ENGINEERED MICROTOPOGRAPHIES TO INDUCE IN VITRO ENDOTHELIAL CELL MORPHOLOGIES STABLE TO SHEAR

By

MICHELLE LEE CARMAN

A DISSERTATION PRESENTED TO THE GRADUATE SCHOOL
OF THE UNIVERSITY OF FLORIDA IN PARTIAL FULFILLMENT
OF THE REQUIREMENTS FOR THE DEGREE OF
DOCTOR OF PHILOSOPHY

UNIVERSITY OF FLORIDA

2007

To my family for their loving support.

ACKNOWLEDGMENTS

I would like to thank my advisor, Dr. Tony Brennan, for the patience and guidance he showed me throughout my graduate studies. I would also like to thank Dr. Chris Batich, Dr. Roger Tran-Son-Tay, and Dr. Mark Segal for serving on my supervisory committee.

I would like to acknowledge the support of my colleagues, both past and present. Their friendships as well as their technical expertise were invaluable. I am especially grateful for the efforts of Leslie Wilson, James Schumacher, Clay Bohn, Adam Feinberg and Thomas Estes. As fellow members of Dr. Brennan's research group, Matthew Blackburn, Kenneth Chung, Amy Gibson, Dave Jackson, Chris Long, Chelsea Magin, Sara Mendelson, Sean Royston, Jim Seliga and Julian Sheets were also very helpful. I also thank the Goldberg and Batich group members for all of their assistance along the way. In particular, Olajompo Maloye was instrumental in helping me reassemble the cell culture lab so that my studies could be completed.

This work would not have been completed without the financial support of the Office of Naval Research and the Alpha 1 Foundation.

Finally, I would like to thank my family for their endless love and support through this experience. They managed to ground me even at the most chaotic moments.

TABLE OF CONTENTS

LIST OF TABLES

LIST OF FIGURES

LIST OF ABBREVIATIONS

ANOVA	Analysis of Variance
AFM	Atomic force microscope
ATS	Allyltrimethoxysilane
BHK	Baby hamster kidney
CH	Channel
DAPI	4',6-Diamidino-2-phenylindole
DMF	Dimethylformamide
DRIE	Deep reactive ion etching
ECM	Extra Cellular Matrix
FG	Fibrinogen
FN	Fibronectin
FOV	Field of View
GEN	Genipin
GTA	Glutaraldehyde
HBSS	Hank's balanced salt solution
HMDS	Hexamethyldisilazane
Hyal	Hyaluronic acid
HyalS	Sulfonated hyaluronic acid
MDCK	Madine Darby canine kidney
MeI	Methyliodide
MEQ	Molar equivalent
NFF	Nuclear form factor
PBS	Phosphate buffered saline

PDMS	Polydimethylsiloxane
PDMSe	Polydimethylsiloxane elastomer
PR	Photoresist
PS	Polystyrene
PVEC	Porcine vascular endothelial cell
RFGD	Radio frequency glow discharge
RGD	Arginine-glycine-aspartate
SEM	Scanning electron microscopy
SK	Sharklet AF™
SM	Smooth
SMC	Smooth muscle cell
TCP	Tissue culture polystyrene
TRITC	Tetramethylrhodamine isothiocyanate
UV	Ultraviolet
WLIP	White light interference profilometry
μCP	Microcontact printing

Abstract of Dissertation Presented to the Graduate School
of the University of Florida in Partial Fulfillment of the
Requirements for the Degree of Doctor of Philosophy

ENGINEERED MICROTOPOGRAPHIES TO INDUCE IN VITRO ENDOTHELIAL CELL MORPHOLOGIES STABLE TO SHEAR

By

Michelle Lee Carman

August 2007

Chair: Anthony Brennan
Major: Biomedical Engineering

Large diameter (>6 mm) synthetic grafts have an established record of clinical success, but consistently occlude at smaller diameters. Attempts to improve patency by seeding grafts with endothelial cells have failed due to removal of cells under high shear. Endothelial cells are known to elongate with flow, requiring cells to break focal adhesions and form new ones. A means of inducing alignment of adhesions before exposure to flow could improve retention.

This is the first known work to investigate the influence of microscale topographies on inducing cellular alignment to improve retention. Initial studies examined the efficacy of existing wetting models. A series of engineered topographies were generated in polydimethylsiloxane elastomer (PDMSe) and contact angles of four solvents were measured. Results correlated strongly with classical models (y=0.99x) with a coefficient of determination of 0.89. Data were compared with settlement of algae spores and porcine vascular endothelial cells. Packing density of algae spores and alignment of endothelial cells followed similar trends, suggesting wettability of topographies may be a strong factor in determining biological responses.

Based on insights from the wettability studies, topographies were designed to induce cytoskeletal alignment of endothelial cells. Gelatin was selected as a potential base material and

glutaraldehyde and genipin were investigated as crosslinking agents. Mechanical properties of gelatin films with varying crosslinker concentrations were determined. Genipin stabilized gelatin more efficiently, exhibiting relatively high modulus and tensile strength while minimizing swelling during hydration.

Porcine vascular endothelial cells were cultured on a series of microscale topographies in genipin-crosslinked gelatin and fibronectin-adsorbed PDMSe. Cells did not grow on gelatin, most likely due to cytotoxicity of unreacted genipin. Cells grew to confluence on topographies formed in fibronectin-treated PDMSe. Focal adhesions and overall cell shape aligned with the underlying topography. The topographies led to significantly smaller mean cell areas, more closely approaching that of cells *in vivo*.

Microscale topographies enhanced cell spreading but not retention after 2 minutes of 2 Pa of flow-induced shear stress. After flow, cells on smooth controls decreased spreading by 60% and tended to form isolated aggregates. Cells on microtopographies maintained spreading, suggesting better viability.

CHAPTER 1
INTRODUCTION

Cardiovascular disease is the leading cause of death in the United States. In 2003 685,089 U.S. deaths were attributed to the disease which correlates to one death every 45 seconds [1]. Although synthetic large diameter grafts have an established record of clinical success, they consistently fail if used at vessel diameters of 6 mm or less. Currently, the preferred treatment of partially occluded vessels is minimally invasive angioplasty and stenting. However, for severe cases angioplasty and stenting are not an option and bypass grafts are necessary. The current standards for coronary bypass grafts are autologous mammary artery followed by saphenous vein despite drawbacks including donor site morbidity and limited supply.

As early as the 1970s, researchers sought to improve the antithrombogenic nature and hence the patency of artificial vascular grafts though the incorporation of endothelial cells onto the inner lumen of the graft surface. They have shown that endothelial cells grow to confluence on a wide variety of substrates, but are removed easily when exposed to shear stresses equivalent to those present in natural human arteries.

Attempts to improve endothelial cell adhesion have included surface modifications of the graft materials. Substrates have been treated though adsorption of adhesion proteins (e.g., albumin, extracellular matrix, gelatin and fibronectin), carbon deposition, photo discharge, and plasma discharge. Protein adsorptions were aimed at providing selective sites for cell adhesions. The remaining techniques were focused on increasing the density of non-specific reactive surface groups or altering surface wettability to influence the adsorption of proteins. Although these methods have been successful at increasing cell density and improving adhesion, there is still a need to develop a surface capable of supporting endothelial cells under high shear stress.

Endothelial cells *in vivo* elongate in the direction of blood flow in regions of high shear stress. It is logical to assume that endothelial cells would tend to alter their morphology in this way when exposed to shear *in vitro* as well. In fact, researchers report that cells maintain attachment and undergo elongation if subjected initially to low shear rates followed by increasing rates up to physiological shear rates [2, 3]. It seems likely that the problem with current attempts to seed vascular grafts with endothelial cells might lie in the fact that cells are seeded in static conditions. It is hypothesized here that these cells are removed when exposed to flow because they must break focal adhesions to adapt their morphology. This implies that a method of increasing cellular alignment under static conditions could improve endothelial cell retention after flow-induced shear stress is applied.

Cells alter their shape based upon the underlying surface morphology, a phenomenon referred to as contact guidance [4]. This has been widely studied over the past several decades with a diverse selection of cell types, surface materials, and topographical features. The design and formation of microscale features has been made possible through advances in fabrication techniques by the microelectronics industry. Simple geometries such as channels and pillars are often used, although more complex geometries have been investigated as well. In particular, channels topographies have been shown to result in cell elongation parallel to the long axis of the channels. For endothelial cells and fibroblasts, cells adhere almost exclusively to the valleys of channels with widths of 5 μm or greater. Consequently, gaps in cell coverage exist wherever the channels are separated by ridges.

The work presented here builds upon these studies in order to increase cytoskeletal alignment of endothelial cells without a disruption in cell confluence. Initially, results of colleagues studying both endothelial cells and marine fouling by algae are examined. Surfaces

used in their studies are evaluated for the influence of topography on surface wettability. A correlation between the topographical influences on wettability and biological settlement is then made. Based upon this work as well as the diverse literature on contact guidance, topographies are designed with the goal of supporting shear-stable endothelial layers.

Topographical dimensions are selected based on their ability to influence the formation of focal adhesions rather than their ability to influence the shape of the cells as a whole. Focal adhesions are typically between 2 and 3 μm in diameter, and so topographical features are developed with lateral dimensions of ~2 μm. The height of topographical features is minimized in order to prevent disruptions in cell confluence.

Polydimethylsiloxane elastomer (PDMSe) surface modified with adsorbed fibronectin has been widely used by colleagues in the study of contact guidance of mammalian cells. PDMSe is examined here as well as a hydrogel material system. Gelatin is derived from collagen which is a natural component of vascular walls. Crosslinked gelatin is investigated for its mechanical stability, ability to replicate microscale topographical features and potential to support cell growth. Glutaraldehyde and genipin were the crosslinking reagents investigated. Glutaraldehyde is commonly used as a fixative for protein systems but is known to be cytotoxic in its unbound state [5]. Genipin is a natural plant extract and suppliers claim a lower level of toxicity.

The primary objective of this work is to determine if microscale topographies induce alignment of endothelial cells and whether this morphological change results in improved resistance to removal by flow induced shear stress. This is the first known attempt to evaluate the influence of engineered topographies to endothelial cell retention during exposure to flow. To achieve this goal, the influence of microscale topographies on biologic settlement was

correlated with changes in surface wettability. Then gelatin was investigated as a potential substrate material and mechanical properties and diffusion kinetics were improved through the optimization of crosslinking. Microscale topographies were next created in the crosslinked gelatin as well as fibronectin-treated polydimethylsiloxane elastomer. The surfaces were evaluated for the ability to induce orientation of endothelial cells without disrupting confluence. Finally, adhesion of the endothelial cells to the topographically modified materials was evaluated using a parallel plate flow chamber.

Specific aim 1. Wettability is correlated with biological settlement on engineered topographies. Contact angles of water, methyliodide, isopropanol, and dimethylformamide are measured using the sessile drop technique on smooth and micropatterned PDMSe. Measured angles are correlated with values predicted by classical wetting theories. The wettability results are correlated with previously published results of algae settlement and nuclear alignment of endothelial cells. One-way analysis of variance (ANOVA) with Tukey's multiple comparisons test are ($\alpha = 0.5$) used to compare groups.

Specific aim 2. Measure the mechanical stability of gelatin films crosslinked with glutaraldehyde and genipin. Gelatin films (10% w/v in water) are crosslinked by genipin (1.4, 2.9, and 4.3% MEQ) and glutaraldehyde (2.9, 4.3 and 5.9% MEQ). Samples are evaluated for the ability to increase modulus, elongation at break and ultimate tensile strength while reducing the percent swelling with water. One way ANOVA with Tukey's multiple comparisons test ($\alpha = 0.5$) are used to determine significant differences in mechanical properties as a result of varying crosslinking reagent and concentration.

Specific aim 3. Demonstrate that cells will align on topographies with 2 μm lateral dimensions while maintaining confluence equal to that of smooth PDMSe. Percentage of

covered surface area, cell density, and alignment of focal adhesions are determined. At least 90% surface coverage must be achieved to be considered confluent. Alignment of focal adhesions is indicated when the average offset angle to topography approaches zero. One way ANOVA followed by pair-wise t-tests ($\alpha = 0.5$) were used to determine significant differences between surface types.

Specific aim 4. Demonstrate that cell alignment induced by micropatterns increases cell retention when subjected to flow generating 2 Pa of shear stress on the sample substrate. Percentage of covered surface area and cell area before and after exposure to flow are determined. Endothelial cell retention is calculated by comparing cell densities before and after flow. One way ANOVA followed by pair-wise t-tests ($\alpha = 0.5$) are used to determine if the topographies increase cellular retention.

CHAPTER 2
BACKGROUND

Introduction

This work proposes the use of microscale topographies to improve endothelial cell retention to biomaterials with the long-term goal of the development of a successful small diameter vascular graft. In order to fully understand the rationale for this research, normal vessel anatomy and the role of the endothelium must first be considered alongside other attempts to improve endothelial cell adhesion to graft materials. These are discussed below as well as the extensive collection of research on cellular responses to microscale topography and efforts to model wettability of textured surfaces.

Vessel Anatomy and the Endothelial Layer

Three distinct layers make up the walls of blood vessels. The innermost layer is referred to as the tunica intima (or tunica interna) and includes the endothelial lining with an underlying layer of connective tissue. In arteries, an internal elastic membrane exists in the outer region of this innermost layer. Beneath the tunica intima lays the tunica media. Sheets of smooth muscle cells are supported by a framework of loose connective tissues which bind the tunica media to the outermost layer, the tunica adventitia (or tunica externa). The tunica media of arteries is thicker compared to veins and contains an external elastic membrane. Collagen (dominant in veins) and elastin (dominant in arteries) fibers provide support.

The endothelium is a made up of a confluent layer of simple squamous cells which regulate cardiovascular physiology. It provides a continuous, selectively permeable barrier between the arterial wall and circulating blood. Additionally, the endothelium controls platelet activation, adhesion, and aggregation and smooth muscle cell (SMC) proliferation and migration.

If allowed to occur uncontrolled, aggregation and proliferation of platelets and SMCs would lead to vessel occlusion.

Endothelial Seeding of Graft Surface

As early as the 1970s, researchers sought to improve the antithrombogenic nature and hence the patency of artificial vascular grafts though the incorporation of endothelial cells onto the inner lumen of the graft surface [2, 3, 6-33]. They have shown that endothelial cells grow to confluence on a wide variety of substrates, but are removed easily when exposed to shear stresses equivalent to those present in natural human arteries.

Attempts to improve endothelial cell adhesion have included surface modifications of the graft materials. Substrates have been coated with adhesion proteins (e.g. albumin, extracellular matrix, gelatin and fibronectin), which have led to improved short term (<3 hours) cellular retention during exposures to flow-induced shear stress [15, 18, 28-30, 32, 33]. Longer exposures, however, show a rapid decrease in cellular attachment on many of these surfaces which has been attributed to desorption of adhesion proteins from the substrate [29, 32, 33]. Additionally, exposed adhesion proteins have been found to promote platelet adhesion and activation [32, 34]. Consequently, gaps resulting from insufficient initial cell seeding or removal due to shear promote the formation of fibrin and fibrous encapsulation of the graft which leads to occlusion.

Other attempts to improve endothelial adhesion have included carbon deposition, photo discharge, and plasma discharge treatments. These treatments were aimed at either increasing the density of reactive surface groups or influencing the adsorption of proteins. Success of these techniques has been limited due to their unspecific interaction with cells and poor control over protein orientation [33]. A more promising treatment has involved the use of a peptide sequence found in fibronectin. Covalent binding of synthetic versions of the arginine-glycine-aspartate

(RGD) sequence has been shown to overcome late term removal of cells and resist platelet adhesion and activation [13, 15, 32].

Shear-Induced Changes in Endothelial Cells

Endothelial cells located in vascular regions of relatively high shear stress (e.g., arteries larger than 0.5 mm in diameter) tend to be elongated in the direction of flow. In these cells, actin filament bundles which terminate at focal adhesions are aligned parallel to flow in an apparent attempt to compensate for the stress [35]. Endothelial cells grown in static culture do not exhibit these same qualities. Instead, the cells tend to be polygonal in morphology with only a small number of stress fibers confined to the cell periphery [36]. These fibers are assumed to be responsible for maintaining cell spreading and preventing contraction.

When cultured cells are exposed to flow-induced shear stresses, cytoskeletal and sometimes morphological changes are induced. These changes are accompanied by a stiffening of the cell which is related to an increase in stress fiber density [37]. These responses have been found to be dependent on both the magnitude of the shear stress and the duration of the exposure. At 0.2 Pa of wall shear stress, an increase in the density of actin filament bundles occurs between 2 and 3 hours of exposure, but cellular alignment does not occur and the stress fibers do not exhibit preferential orientation in the direction of flow [36]. After 7 hours of exposure to 1 Pa of wall shear stress, cells elongate and stress fibers align with the flow direction accompanied by the coalescence of focal contacts so that they are fewer in number but greater in size [38]. For a cell grown in static culture to align itself in this manner, it must break many of the focal adhesions it created with the surface and form new ones [38, 39]. It is hypothesized here that during this transitional period cells are removed from a surface. If this is the case, then a method that would cause the cells to align prior to implantation would be advantageous.

In the 1990s Ballermann et al. of Johns Hopkins University significantly improved *in vivo* endothelial cell retention by preconditioning cell-seeded grafts with *in vitro* shear stress [2, 3, 40]. They found that exposing cell seeded grafts to 0.1 Pa wall shear stress for 3 days and then 2.5 Pa for a subsequent 3 day period significantly improved cell retention and reduced neointimal thickness on aortic interposition grafts in rats. This supports the hypothesis that alignment of the actin cytoskeleton prior to implantation is advantageous.

Micropatterning of Cells

It has long been known that cells respond to the shape of the substrate on which they grow. The earliest known report of this was made by Harrison in 1914 in which he observed that fibroblasts found in embryonic nervous tissue from frogs take on a polygonal shape when cultured against smooth glass, but become drawn-out when grown on spider silk [41]. The term 'contact guidance' was later used to describe the phenomenon when Weiss performed a similar experiment with nerve cells grown on glass fibers [4].

In the past several decades, literature on cellular responses to topography has expanded rapidly. Researchers have investigated numerous combinations of cell types and topographical geometries and dimensions. Appendix A provides a table summarizing the pertinent literature. The degree of contact guidance varies with topographical dimensions and geometry as well as the cell type studied. As an example, Clark et al. examined chicken embryonic cerebral neurons and two epithelial cell types: baby hamster kidney (BHK) and Madin Darby canine kidney (MDCK) [42]. All three cell types were grown on grooved polymethylmethacrylate (Perspex®) with channel widths and spaces ranging from 4 to 24 μm and depths ranging from 0.2 to 1.9 μm. In all cases, alignment increased with decreased spacing and increased depth. Depth had a greater influence than spacing for the dimensions studied and the MDCK cells were more sensitive to topography than BHK cells.

Many researchers have investigated the potential use of topography for preventing fibrous encapsulation and subsequent contraction and stiffening of implants [43, 44]. This goal is of particular interest for maintaining the aesthetic appearance and mechanical integrity of breast implants. Campbell and von Recum examined the influence of pore size of Versapor® filter materials (acrylic copolymers on nylon supports) implanted subcutaneously in canines on fibrous tissue growth [43]. Nonadherent, contracting capsules were formed on materials with pore sizes less than 0.5 μm. Thin, tightly adhered capsules were formed on implants with pore sizes ranging from 1.4 to 1.9 μm and inflammatory tissue infiltrated pores sizes greater than 3.3 μm. Schmidt and von Recum later performed a similar experiment in which 2, 5 and 8 μm wide/spaced grooves were patterned into silicone elastomer and implanted into rabbits [44]. In general it was found that the 2 and 5 μm grooves (depths ranging from 0.4 to 0.6 μm) resulted in fewer attached cells and thinner fibrous capsules than the smooth control and 8 μm grooves. Additionally the surfaces were tested *in vitro* with murine peritoneal macrophages and cellular alignment was observed.

In a more recent study, van Kooten and von Recum have shown that in addition to altering cellular morphology, topography can increase the density of focal adhesions [45]. Fibroblasts grown on 2 μm wide/spaced grooves were shown to have a greater density of focal adhesions than the same cells grown on 8 μm wide/spaced grooves and smooth fibronectin-coated silicone substrates. A 0.5 μm groove depth was used for the study.

Walboomers et al. have shown that topography can be tailored to increase cell density relative to a smooth substrate [46]. Fibroblasts were grown on both smooth and microgrooved (1-10 μm wide and 0.5-5.4 μm deep) polystyrene. It was shown that for samples of equal projected planar areas, the number of adhered fibroblasts was increased on all topographies

relative to the smooth control. When the numbers were corrected to account for the surface area added by roughness, however, the 1.5 μm deep grooves reduced cell density as did the 1 and 2 μm wide grooves.

Fibroblasts are the most common cell type used in studies with microscale topographies. Literature specific to endothelial cell responses to topography is considerably more limited. Matsuda and Sugawara bovine aortic endothelial cell attachment on 20 to 130 μm wide channels and found that alignment increased with decreased channel width [47]. Mrksich et al. grew bovine capillary endothelial cells on polyurethane coated with gold and patterned with alkane thiols and adsorbed fibronectin [48]. They examined V-shaped channels that were 25 and 50 μm wide and had equal spacing. They showed that endothelial cells adhere to ridges or valleys, depending on which was patterned with the alkane thiol and therefore adsorbed fibronectin. Palmaz et al. examined migration of human aortic endothelial cells on nitinol containing 1, 3, 15 and 22 μm channels [49]. Cells aligned with all channels and migration was greater on larger channels. Uttayarat et al. studied smaller channel topographies in fibronectin treated polydimethylsiloxane elastomer (PDMSe). Channel widths ranged from 2.7 to 5.5 μm and depths ranged from 0.2 to 4.6 μm [50]. Cell proliferation was similar on all substrates and cell elongation and alignment increased with channel depth. Focal adhesions formed in channels for all topographies except the 4.6 μm deep channels. Barbucci and Magnani investigated the influence of the combination of topography and chemical patterning on cell behavior [31, 51]. They observed that endothelial cells increasingly align themselves on ridges as the topographical spacing is reduced from 100 to 10 μm. Similar results were found by Wilkerson et al during the study of endothelial cell growth on ridges ranging in spacing from 20 to 5 μm [52, 53]. Feinberg et al has also examined endothelial cell growth on topography and chemical patterns [53, 54].

They found that cells are disrupted by topographies with profile heights greater than 1 μm and that focal adhesions form almost exclusively on fibronectin (FN) regions of FN-treated PDMSe. Furthermore, the area of individual focal adhesions does not vary with surface treatment and is approximately 2 μm^2.

Topography and Wettability

Although topography is clearly a significant factor in determining cell confluence and shape, the mechanism for this response has not been elucidated. The change in wettability of a surface that results from surface roughness, i.e., topography, is likely a contributing factor. Wettability is often characterized in terms of the three phase contact angle which relies on the relative interfacial tensions according to Young's equation given below [55]:

$$\gamma_{SG} = \gamma_{SL} + \gamma_{LV} \cos\theta . \tag{2-1}$$

Young's equation assumes the surface is chemically and topographically homogeneous and does not take into account the dynamic nature of wetting. Many groups have demonstrated the bidirectional nature of surface wetting and therefore, one must consider dewetting as well [56-58]. It has been hypothesized that the hydrophobicity and hence the force required to affect spreading is a function of the hysteresis between advancing and receding angles.

Numerous groups have studied the wetting characteristics of rough surfaces. The earliest report to correlates wetting with topography was made by Wenzel, who assumed the contours of the topography are fully wetted [59]. The apparent contact angle on the textured surface ($\cos\theta^*$) was related to the Young's contact angle on a smooth surface of the same material as follows:

$$\cos\theta^* = r\cos\theta . \tag{2-2}$$

Wenzel defined the roughness ratio (r) as the actual surface area divided by the area of the surface when projected onto a two dimensional plane.

A more detailed approach by Cassie and Baxter proposes an alternative to the Wenzel equation [60]. They evaluated the wetting by water of waxy surfaces which where not just rough, but also porous. Under this condition, water did not follow the contours of the topography and instead rested upon a composite structure of wax and air. The ratios of the areas of liquid beneath the drop in contact with solid and air relative to the planar surface area were termed f_1 and f_2 respectively. The resulting contact angle (θ_D) for the porous surface was then thermodynamically determined to be the following:

$$\cos\theta_D = f_1 \cos\theta - f_2 . \tag{2-3}$$

Marmur[57] and Quéré et al.[61] have independently examined the thermodynamics of the wetting regimes to determine when air entrapment will be energetically favored. Quéré et al. defined the variable ϕ_s as the fraction of liquid beneath the drop in contact with solid. It is equivalent to the f_1 term in Cassie and Baxter's relationship. Air entrapment would be favored for liquids of sufficiently high surface tensions ($\theta > \cos^{-1}[(f_1-1)/(r-f_1)]$) and would be metastable for liquids satisfying the condition of $90^\circ < \theta < \cos^{-1}[(f_{1s}-1)/(r-f_{1s})]$. Wetting as described by Wenzel would be favored for liquids of intermediate surface tensions (i.e. $\cos^{-1}[(1-f_1)/(r-f_1) < \theta < \cos^{-1}[(f_1-1)/(r-f_1)]$) and wicking of liquid into topographical recesses ahead of the drop would occur for liquids of sufficiently low surface tension ($\theta < \cos^{-1}[(1-f_1)/(r-f_1)]$). The apparent contact angles (θ') for cases of air entrapment and wicking are given by the following:

$$\text{Air entrapment: } \cos\theta^* = -1 + f_1(\cos\theta + 1) \text{ for } \theta \geq \cos^{-1}\frac{f_1 - 1}{r - f_1} \tag{2-4}$$

$$\text{Wicking: } \cos\theta^* = 1 + f_1(\cos\theta - 1) \text{ for } \theta \leq \cos^{-1}\frac{1 - f_1}{r - f_1} . \tag{2-5}$$

Application to this Work

Based on the background work presented here, studies were developed to examine the potential of microscale topographies to induce endothelial cell morphologies that increase resistance to shear removal. In the following chapters, studies are presented that examine the influence of microscale topographies on cellular attachment. In the first study, wettability is correlated with the biological response of algae spores (*Ulva*) and porcine endothelial cells. Later, genipin and glutaraldehyde crosslinked gelatin is investigated for its ability to replicate and maintain fidelity of microscale features. Then the gelatin topographies are evaluated alongside fibronectin-treated PDMSe topographies for potential to support endothelial cell growth. Cell density, confluence and orientation are measured in relation to the microscale features. Finally, endothelial cell retention to microscale topographies is measured after exposure to flow-induced shear stress in a parallel plate flow chamber.

CHAPTER 3
INFLUENCE OF TOPOGRAPHY ON WETTABILITY AND BIOADHESION

Notice of Previous Publication

The contents of this chapter were originally published in Biofouling © 2006 by Taylor and Francis [62]. It is reprinted here in accordance with the copyright agreement.

Introduction

Reports on cellular responses to topographical cues on both nanometer and micrometer scales have increased in the past few decades [63-66]. Appropriately scaled nanotopographies have been shown to prevent cell attachment by prohibiting formation of focal contacts [66, 67]. Alternatively, cells can respond to microscale features by altering their shape such as elongating along grooves [45, 63]. In the area of marine fouling, topography has been shown to alter settlement of algae [68, 69], barnacles [70] and bacteria [71]. The change in wettability of a surface that results from surface roughness (i.e., topography) is likely a contributing factor to these responses.

Wettability is often characterized in terms of the three phase contact angle which relies on the relative interfacial tensions according to Young's equation [55]:

$$\gamma_{SG} = \gamma_{SL} + \gamma_{LV} \cos\theta . \tag{3-1}$$

Young's equation assumes that the surface is both chemically and topographically homogeneous and does not take into account the dynamic nature of wetting. Many groups have demonstrated the bidirectional nature of surface wetting and therefore, one must consider dewetting as well [56, 58, 72].

Numerous groups have studied the wetting characteristics of topographically rough surfaces. The earliest report that correlates wetting with topography was made by Wenzel [59], who assumed the contours of the topography become fully wet and the change in contact angle is

due to an increase in surface area that topography provides. Wenzel defined a roughness ratio (r) as the actual surface area divided by the area of the surface when projected onto a two dimensional plane to account for the change in wetting in terms of contact angle as follows:

$$\cos\theta^* = r\cos\theta\,. \tag{3-2}$$

A more detailed approach by Cassie and Baxter [60] proposed an alternative to the Wenzel equation. They evaluated the wetting by water of waxy surfaces which where not just rough, but also porous. Under this condition, water did not follow the contours of the topography and instead rested upon a composite structure of wax and air. The ratios of the areas of liquid beneath the drop in contact with solid and air relative to the planar surface area were termed f_1 and f_2 respectively. The resulting contact angle (θ_D) for the porous surface was then thermodynamically determined to be the following:

$$\cos\theta_D = f_1\cos\theta - f_2\,. \tag{3-3}$$

More recently, Quéré et al. [61, 73-75] demonstrated that for a given surface, regimes of both Wenzel and Cassie-Baxter behavior exist across a range of liquid surface tensions. They defined the variable ϕ_s as the fraction of liquid beneath the drop in contact with solid. It is equivalent to the f_1 term in Cassie and Baxter's relationship. Air entrapment, fully wetted, and wicking occurs for liquids of sufficiently high, moderate, or low surface tensions respectively. In the case of wicking, the liquid is drawn into the topography at the advancing edge so that the drop rests on a composite surface of liquid and solid. The corresponding relationships and criteria for each case are given below.

$$\text{Air entrapment: } \cos\theta^* = -1 + f_1(\cos\theta + 1) \text{ for } \theta \geq \cos^{-1}\frac{f_1 - 1}{r - f_1} \tag{3-4}$$

$$\text{Fully wetted: } \cos\theta^* = r\cos\theta \text{ for } \cos^{-1}\frac{1 - f_1}{r - f_1} \leq \theta \leq \cos^{-1}\frac{f_1 - 1}{r - f_1} \tag{3-5}$$

Wicking: $\cos\theta^* = 1 + f_1(\cos\theta - 1)$ for $\theta \le \cos^{-1}\frac{1-f_1}{r-f_1}$. (3-6)

Quéré et al. also indicated that the air entrapment state would be metastable for the following condition:

$$90° \le \theta \le \cos^{-1}\frac{f_1 - 1}{r - f_1}. \quad (3\text{-}7)$$

In the present study, a series of engineered microtopographies was created in a polydimethylsiloxane elastomer (PDMSe). The engineered patterns include a biomimetic inspired design that is based upon the configuration of placoids of fast moving sharks. Changes in wettability were measured and compared against the values predicted by the Wenzel and Cassie-Baxter relationships. Some of these surfaces were then selected to test the hypothesis that wettability influences the contact-sensing processes used by living cells. For this purpose we selected two well-characterized but contrasting model systems to represent both marine and biomedical fouling, viz. the motile spores of the marine alga *Ulva* (syn. *Enteromorpha*), and porcine vascular endothelial cells (PVECs) which form the inner lining of arteries.

The green algal genus *Ulva (*formerly *Enteromorpha)* is the most common macroalga contributing to 'soft' fouling of man-made surfaces throughout the world [76] and has been developed extensively as a model system for experimental studies [77-80]. Fouling is initiated by the settlement and subsequent adhesion of motile spores, a process which is influenced by a variety of surface-associated cues. We have previously used engineered microtopographies in PDMSe to identify surface features that *promote* settlement [68, 69]. Our hypothesis in the present study was that topographic patterns that mimic a natural antifouling surface, viz. the placoid structure of shark skin, may provide a surface with low settlement properties.

Endothelial cells are widely used as models in which to study the influence of substratum morphology on adhesion and contact-mediated growth of animal cells [31, 51, 52, 81-84]. We have chosen to use porcine vascular endothelial cells (PVECs) for our study because of the local availability of a well characterized cell line [85]. The pig has been shown to be an ideal preclinical model for vascular research, as *in vitro* tests have concluded that the coagulation and fibrinolytic systems of swine closely resemble that of humans [86, 87]. In the present study PVECs were used to investigate the affect of feature spacing (5 to 20 μm) on cellular orientation. This response was then correlated with the influence of topography on wettability.

Materials and Methods

Material

A platinum catalyzed PDMSe (Dow Corning Corporation's Silastic T-2) was chosen for this study due to its high transparency and reproducibility. The PDMSe is filled with micron and sub-micron silica particles. In the unmodified state, the polymer is known to promote minimal bioadhesion because of its combination of low surface energy and low modulus [69]. The PDMSe was prepared by mixing ten parts by weight of resin with one part by weight curing agent. The PDMSe was typically cured at ~ 22°C for 24 hours.

Pattern Designs

The features studied included channels, ridges, pillars, pits and ribs (Fig. 3-1). Channels, ridges, pillars, and pits were 5 μm wide and spaced 5, 10, and 20 μm apart. The rib designs are a reduction of the scales of fast moving sharks. We refer to this biologically inspired pattern as the 'Sharklet AF™' because it is an antifouling topography that was inspired by, but does not reproduce, the skin of the shark. The ribs are 2 μm wide, spaced 2 μm apart, and have lengths ranging from 4–16 μm. Both 1.5 and 5 μm high channel and pillar features were investigated, whereas the ribs of the Sharklet AF™ were 4 μm high.

Silicon Wafer Processing

Patterns were etched into silicon wafers using standard photolithography techniques as described previously [88]. Wafers were then critically cleaned using a piranha etch (50:1 H_2SO_4 and H_2O_2) at 120°C for 10 min followed by subsequent rinsing in acetone and ethanol prior to each replication with PDMSe. Hexamethyldisilazane was used to methylate the surfaces in order to prevent adhesion.

Pattern Transfer and Die Production

Patterns are transferred to PDMSe in either negative (channels, pits and Sharklet AF™) or positive (pillars and ridges) form (Table 3-1). Negatives were replicated directly from the etched wafer so that the PDMSe topography is inverted compared to the silicon wafer. For example, pillars in the wafer would transfer as pits into the PDMSe. Positives were generated by first solution casting polystyrene (0.15 g/mL in chloroform) against the wafer followed by curing the PDMSe against the polystyrene. Epoxy dies (Epon 828 with Jeffamine D230, 9.7:2.73 by weight) were then made from both positively and negatively patterned PDMSe.

Sample Production

Samples included PDMSe films that were either free standing or adhered to glass slides. In both cases, the PDMSe was cured in a glass mold (Fig. 3-2) as described previously [68]. Smooth samples were cast directly off the glass, while patterned samples were produced by casting against epoxy or silicon dies. For glass-backed samples, slides were first pretreated with 0.5% allyltrimethoxysilane (ATS) in a 95% ethanol/water solution to improve adhesion. Three replicates of each pattern type were produced. Fidelity of the surface features was verified with the aid of light microscopy and SEM.

Contact Angle Measurements

Wettability was evaluated on free-standing PDMSe films containing 5 μm high channels, pits, and Sharklet AF™ and 1.5 μm high ridges by the Sessile drop method with 2 μL drops. This method looks at advancing contact angles measured in the first few seconds of contact. Video capture goniometry was used and angles were measured with ImageTool software. Liquids included in the study were nanopure water (17 MΩ*cm resistivity), methylene iodide, and dimethylformamide. Surfaces were rinsed with ethanol and dried at 80°C prior to testing with each liquid. One drop was placed on three replicates of each pattern and two angle measurements, one from the left and one from the right, were taken per drop. In this manner, six measurements were taken per pattern. Drops were viewed down the lengths of channels and ribs.

Comparison with Model

Wettability data were compared against values predicted by Quéré's combined model of Wenzel and Cassie-Baxter relations. Predicted contacted angles were calculated from the model using the roughness ratios and solid surface fractions of each topography. For both relations, the contact angles on rough surfaces are related to the contact angle on the smooth surface. In order to account for this, data were normalized by dividing the contact angles for each liquid on textured surfaces by the angle the same liquid makes on smooth PDMSe. Normalized values predicted by the models were then plotted against normalized values measured on the surfaces. Linear regression was performed to test the validity of the models.

Predicted Wetting on Novel Topographies

Once the model was determined to give a good approximation of the wetting across engineered topographies, it was used to predict the effectiveness of proposed topographies.

Topographies considered included circular pillars, square pillars, star-shaped pillars, ring-shaped pillars, a combination of triangular and circular pillars, a gradient array of circular pillars, and hexagonal pillars (Fig. 3-3 and Table 3-2). Both 1 and 3 μm features heights were evaluated. The Sharklet AF™ topography was also considered at these depths to determine effectiveness in altering wettability.

***Ulva* Zoospore Assay**

PDMSe samples containing 5 μm wide ridges and pillars spaced 5, 10 and 20 μm apart at 1.5 and 5 μm heights in addition to the 5 μm deep Sharklet AF™ topography were evaluated for settlement of *Ulva* spores. Three replicates of each type were tested and all samples were backed by glass slides. Settlement data for the pillars and ridges have been published previously [68, 69]. The 5 μm Sharklet AF™ topography was evaluated using the same protocol except for one slight deviation. Due to the ultrahydrophobic nature of the Sharklet AF™ topography, samples for this study were shipped to the bioassay site in nanopure water to ensure air was displaced from the features and the samples were fully wetted during the assay.

Ulva zoospores were obtained from fertile plants of *Ulva linza* collected from Wembury Beach, UK (50º18' N; 4º02' W) and prepared for experiments as previously described [79]. Briefly, 10 mL of spore suspension (adjusted to $2x10^6$ mL^{-1}) is added to each sample and incubation is carried out for 60 min in the dark followed by fixation with 2% glutaraldehyde in artificial seawater (Instant Ocean™). Settled spore counts were taken using a 10X objective with a Zeiss Kontron 3000 image analysis system attached to a Zeiss epifluorescence microscope and video camera as described by Callow et al. [68]. Thirty images were taken of each of the 3 replicate samples to quantify the number of attached spores. For smooth samples and both flat and textured areas of patterned samples, images were taken at 1 mm intervals along the axis of

the slide. Spore settlement data are reported as the mean number of adhered spores (x = 90) with 95% confidence limits.

Porcine Vascular Endothelial Cell (PVEC) Assay

Free-standing PDMSe samples containing 5, 10, and 20 μm spaced, 5 μm wide ridges at both 1.5 and 5 μm heights were evaluated. In order to promote cell attachment, surfaces were coated with fibronectin (FN) using the method of Ostuni and Whitesides [89]. This protein adsorption makes the surface hydrophilic and improves cellular adhesion. Topography coupled with fibronectin should induce cellular alignment within channels to maximize contact area while minimizing tension on the cell membrane. Briefly, lyophilized bovine plasma FN (Sigma) was dissolved in 2 mL of 0.22 μm filtered water at 37°C for 45 minutes and then diluted to 50 μg/mL in Hanks Balanced Salt Solution (HBSS). Sterilized samples were placed in individual wells of a 24-well plate, and FN was added in 0.5 mL aliquots to each sample. During exposure to vacuum (100 kPa) to remove trapped air, samples were left to incubate for 1 h at room temperature. Air must be removed to prevent denaturizing of the protein which would affect adhesion [90]. The FN solution was aspirated out and then the samples were washed 3 times with HBSS.

PVECs obtained from the main pulmonary artery of 6 to 7-month-old pigs were supplied by Dr. Edward Block's lab between passages 2 and 5 [91]. Cells were seeded at a density of $2x10^5$ cells per sample in 1 mL of serum-free media. Serum-free media was selected because the adhesion protein was already adsorbed on sample surfaces. The cells were incubated at 37°C and 5% CO_2 for 48 to 72 hours.

Samples were fixed with cold 10% n-buffered formalin for 20 minutes. The cell bodies were then stained for 20 minutes in 1% crystal violet solution. Hematoxylin (Richard Allan

Scientific) was used to stain cell nuclei so that nuclear elongation could be used to quantify contact guidance. Cells were stained in hematoxylin for 2 minutes

Cells were imaged on the surface at 200X magnification using a Nikon Optiphot microscope and Matrox image capturing system. Multiple images were taken at each feature width that included at least 5 nuclei. Images were analyzed to measure the nuclear form factor (NFF) of each nucleus. The NFF is the log of the ratio of the cell length to width (Fig. 3-4). This measurement was adapted from a procedure introduced by Dunn and Heath which requires the measurement of the length and width of nucleus at its widest point [92]. A 5x5 grid was superimposed on the images, and 5 nuclei were chosen per image, each from a separate square of the grid. Using this method, at least 20 nuclei per topography type were quantified.

Statistical Methods

Results are reported using mean values and 95% confidence intervals. One-way analysis of variance (ANOVA) and multiple comparison tests (Tukey, 95% confidence interval) were used to compare groups.

Results

Contact Angle Measurements

As expected, topography increased water contact angles and decreased both methylene iodide and dimethyl formamide contact angles (Table 3-3). The most effective topography at altering wettability was the Sharklet AF™, whereas the 20 μm spaced ridges and pits behaved the most like smooth PDMSe. The water contact angle on PDMSe was increased by as much as 20%, while the contact angles of methylene iodide and dimethyl formamide were reduced by as much as 35% and 33%, respectively. Droplets on the pits and Sharklet AF™ maintained a circular contact area, whereas droplets on the channels and ridges elongated along the features.

Because of their cylindrical, rather than spherical, geometry the contact angles on the channels and ridges must be treated as estimates.

Receding contact angles were not evaluated by the captive air method because of difficulty in bubble placement. For example, the channel patterns were only 0.33 cm wide (Fig. 3-5) and the topographies became invisible when wetted. Consequently, it was impossible to be certain the air bubble remained in the desired region. In addition, the Wilhelmy plate technique was also deemed unsuitable because of the inability to prepare a proper sample (same topography on all sides).

The effect of topography height was examined by comparing the 5 μm spaced, 5 μm deep channels against the 5 μm spaced and 1.5 μm deep ridges. Because droplets were placed away from the pattern boundaries, the feature height was the only difference sensed by the spreading drops. The water contact angle was significantly higher on the 5 μm deep channel compared to the 1.5 μm deep ridge. The effect of feature spacing was examined by looking at trends within the pits, channels, and ridge topographies. Increased feature spacing and decreased pattern depth resulted in diminished contact angle changes.

Comparison with Model

The sessile drop contact angle data were compared against the model to determine its viability for use in prescreening ideas for new patterns. The 1.5 μm high ridges have relatively low roughness factors (1.1 to 1.3), and solid fractions (0.2 to 0.5). On these surfaces water droplets appear to follow the situation proposed by Wenzel (Fig. 3-6) rather than the metastable state described by Quéré. The Sharklet AF™ topography, on the other hand, has a high roughness factor (5.0) and moderate solid fraction (0.47), and all three test liquids followed the situations described by Cassie (air pockets or wicking).

Quéré proposed that air entrapment would be favored for liquids of sufficiently high surface tensions ($\theta > \cos^{-1}[(f_1-1)/(r-f_1)]$) and would be metastable for liquids satisfying the condition of $90^\circ < \theta < \cos^{-1}[(f_1-1)/(r-f_1)]$. The results in Figure 3-6, however, suggest that the metastable air pocket state is not favored, and that instead the Wenzel regime is followed. Consequently, the model has been adapted to eliminate the metastable state. In order to test the reliability of the adapted model, data were normalized with respect to the smooth contact angles. The model fits the data well ($y = 0.99x$) with a coefficient of determination of 0.89 (Fig. 3-7).

Predicted Wettability on Novel Topographies

The model predicts that the hexagons would be the least effective at increasing the hydrophobic nature of PDMSe (Table 3-4) relative to the various designs (i.e., circular pillars, square pillars, star-shaped pillars, combination of triangular and circular pillars, and gradient array of circular pillars). The results reveal a minimal increase of only 1º and 3º in the water contact angle for the 1 and 3 μm high hexagonal features in PDMSe, respectively. These changes would likely be insignificant when considered with the typical standard error in contact angle measurements of 3º. The model predicts that the 3 μm tall mixed star pattern will be the most effective and lead to an increase in water contact angle of approximately 31º relative to smooth PDMSe. A maximum height of 3 μm was chosen for this investigation because 2 μm diameter pillars in PDMSe tend to collapse at higher aspect ratios (Fig. 3-8).

All pattern types were predicted to be fully wetted by water when feature heights are held to 1 μm. Increasing the height to 3 μm, however, should promote the trapping of air in all topographies except the hexagons, circular pillars, and gradient pillars.

Ulva Zoospore Assay

The ridge topographies enhanced spore settlement (Fig. 3-9). The most significant effect was observed on the 5 μm spaced, 5 μm high ridges, which increased settlement by 150% relative to the smooth surface. This dimension is roughly equivalent to the diameter of the pear-shaped swimming spore at its widest point and the diameter of the settled spore (Fig. 3-10). As spacing increased, the density of settled spores approached that of smooth PDMSe. Settlement density decreased on the shorter 1.5 μm high ridges compared to the 5 μm high ridges, but still remained at least as high as the density on smooth PDMSe. Settlement occurred almost entirely in valley regions for all ridge topographies.

The Sharklet AF™ topography, which has feature dimensions smaller than the spore body, significantly reduced settlement density by ~86% relative to smooth PDMSe (Fig. 3-9). Spores avoided the 2 μm wide channels and were largely confined to defects and slightly wider spaces (~3 μm) located between adjacent Sharklet AF™ diamonds (Fig. 3-10).

PVEC Assay

Cell growth on smooth PDMSe was random with respect to orientation. Consequently, NFFs were not significantly different from zero (Fig. 3-11). Cells attached to ridge patterned substrata became aligned with the topographies. The PVECs settled almost entirely in the valleys formed by adjacent ridges similar to the *Ulva* spores (Fig. 3-12). Cell orientation was most strongly directed by the 5 μm deep, 5 μm spaced ridges. NFFs varied directly with feature height and inversely with feature spacing for 5 μm deep features (Fig. 3-11).

The NFFs are significantly different for all widths at the 5 μm depth. At the 1.5 μm depth only the 5 μm wide ridges and smooth surfaces showed a significant difference. One of the difficulties in the analysis is the fact that the nuclei are not round, but rather elongated in

random directions on the smooth FN treated PDMSe samples. Consequently, the mean nuclear form factors for smooth areas are near zero, but with a large standard deviation.

Discussion

Researchers have independently shown that topography alters wettability [59, 60] and surface energy influences bioadhesion [93-97]. This study investigated the interrelationship of all three factors (topography, wettability and adhesion) simultaneously using two different cell types viz. motile algal spore which 'choose' where to settle and adhere and cultured animal cells (PVECs) which are known to adapt to underlying substrate morphology. The wetting response was well described by the Wenzel and Cassie-Baxter equations for the topographies investigated, but ideally one would also like to predict the effect topography has on bioadhesion. It is interesting to note that both biological models responded to the channel topographies by trying to fill the valleys either through settlement packing (*Ulva*) or by elongation (PVECs). This suggests that their responses are governed by the same underlying thermodynamic principles as wettability. Consider a cell settling on a textured surface. If the cell is too large to rest between or on top of the features, it must bridge, align, or conform to their shape. Bridging is similar to the air pocket state and alignment is similar to the wicking states described by the Cassie-Baxter relation. Alternatively, conforming resembles Wenzel behavior.

Consider a surface that an organism will settle on but for which it has a relatively low affinity (e.g., PDMSe for *Ulva* spores). If the topography of this surface is engineered to expand the Cassie-Baxter regime, then the organism may be induced to bridge the features. This would increase tension along the unsupported regions of the organism's membrane. Additionally, bridging would reduce the area of contact between the organism and surface, which would decrease the adhesion strength. Thus, bridging reduces the potential for settlement by creating unfavorable energy barriers. This would be very useful, particularly in limiting marine fouling.

Using this hypothesis, the Sharklet AF™ topography was engineered to enhance hydrophobicity with dimensions smaller than the *Ulva* spore so that bridging would be necessary for settlement to occur. It is important to note that the Sharklet AF™ design is biomimetically inspired rather than a true biomimic. Although the basic pattern of the placoids has been maintained, the dimensions have been reduced and the tips of the ribs have been flattened. As designed, spores avoided the topography which resulted in an 86% reduction in settlement density. This result provides the first demonstration that engineered microtopographies can inhibit the settlement of spores of marine algae.

In addition to preventing settlement, topographies can also be engineered to promote it. Consider an organism settling on a surface which it prefers (e.g., PVECs on fibronectin-coated PDMSe). If the topography of this surface is engineered to expand the Cassie regime, then the organism may be induced to align with topographies. This was evident in the PVEC study presented here. For the topographies studied, the Cassie-Baxter regime increased with increased spacing and increased depth. Similarly, PVECs showed increased alignment with increased spacing and depth as demonstrated with NFFs. This result is consistent with research by von Recum et al. demonstrating rat dermal fibroblasts become increasingly oriented on 0.5 μm deep microgrooves as the width is reduced from 10 to 2 μm [44, 45, 98, 99].

Microbubbles on surfaces are reported to denature surface adsorbed proteins, which increases cell adhesion [90]. Fibronectin pretreatment of PDMSe was used in the PVEC assay to convert the surface to a hydrophilic surface needed for initial cell attachment. To minimize any potential artifacts in the PVEC assay that could be caused by differential fibronectin adsorption through the presence of microbubbles, all PDMSe surfaces were degassed during fibronectin adsorption to eliminate surface-adsorbed air bubbles from topographies. It can therefore be

concluded that it is unlikely that the results on PVEC alignment can be ascribed to artifacts caused by microbubbles. In the case of *Ulva* spore settlement, it can also be reported that hydrophilic modification of the topographies (which would eliminate microbubble formation) did not alter the inhibition of zoospore settlement by the Sharklet AF™ topography [100]. Thus, it is concluded that *Ulva* zoospores were contact sensing the topography and were not influenced by the presence of microbubbles [101].

These results suggest that wettability models can be useful in predicting cellular contact guidance for engineered topographies. It is important to note that bioadhesion is complex and does not only rely on surface energetics but is also species-specific [102]. The material modulus and surface elasticity of the cell membrane are also important to consider. The process is further compounded by the variety of adhesive proteins that an organism may secrete. Additionally, the use of wettability models is limited by their assumption that the droplet is much larger than the topographical features. This allows for line tension effects to be neglected. Investigation of wetting of these topographies by picoliter-sized drops may provide greater insight. Although further investigation is needed, these relationships may eventually be used to develop models capable of predicting the contact guidance of cells and microorganisms. Such a model would be of value in the biomedical device and marine coating industries.

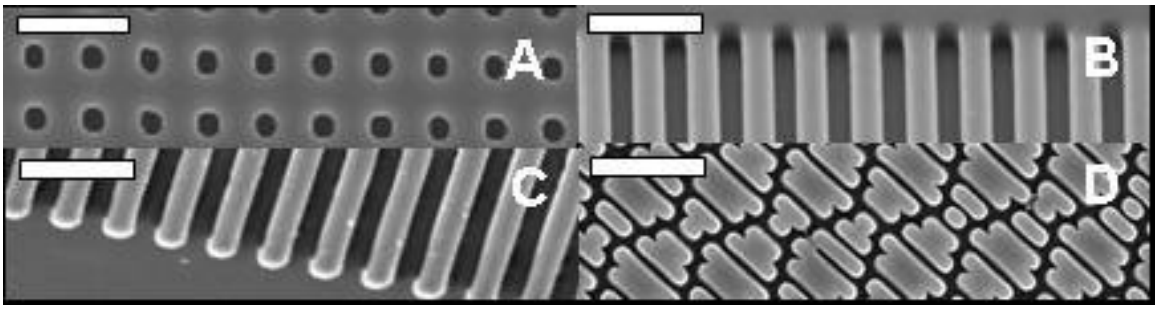

Figure 3-1. SEM images of PDMSe microtopographies. A) 5 μm diameter, 5 μm diameter, 5 μm spaced pits. B) 5 μm wide, 20 μm spaced channels. C) 5 μm wide and 20 μm spaced ridges. D) Sharklet AF™ topography. Pillars, pits, channels, and Sharklet AF™ are all 5 μm deep, while ridges are 1.5 μm high. Scale bars represent 20 μm.

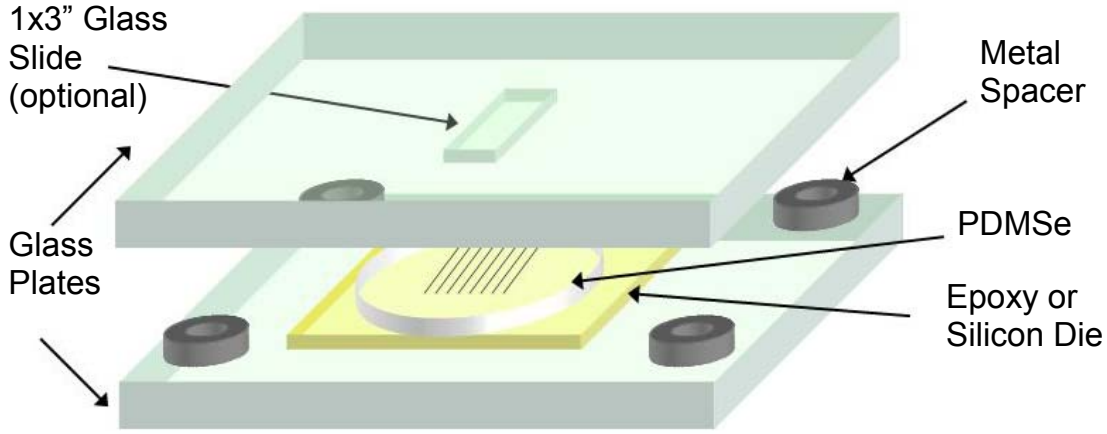

Figure 3-2. Glass mold used to make PDMSe samples. The epoxy and silicon dies were used only for patterned samples.

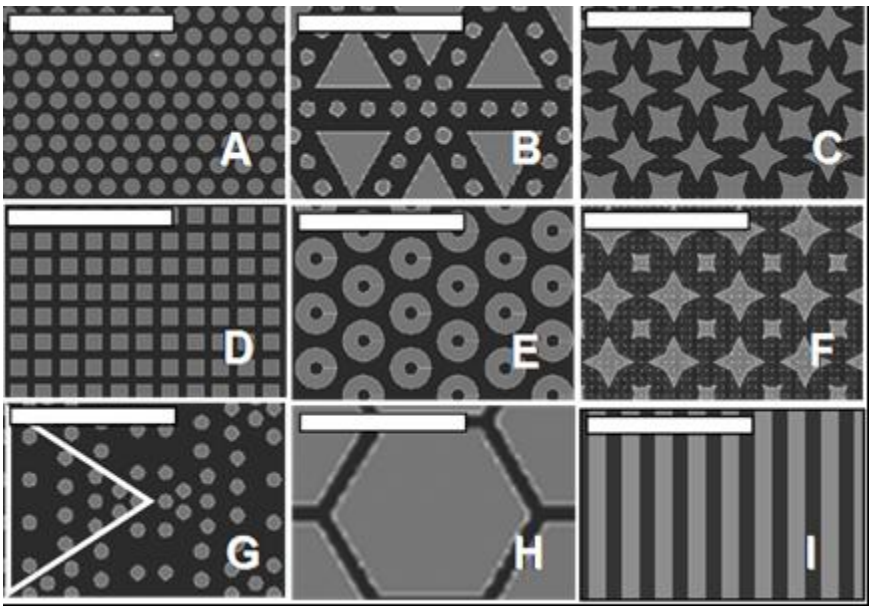

Figure 3-3. AutoCad sketches of proposed topographies. A) 2 μm diameter, 2μm spaced pillars. B) triangles and 2 μm pillars. C) 4 μm wide, 2 μm spaced stars. D) 2 μm wide, 1 μm spaced square pillars. E) Rings with 2 μm inner diameter and 6 μm outer diameter, spaced 2 μm apart. F) 4 and 2 μm wide stars. G) 2 μm diameter pillars spaced 1, 2 and 4 μm apart in a gradient array (repeat unit designated by triangle). H) hexagons with 12 μm long sides and spaced 2 μm apart. I) 2 μm wide, 2 μm spaced channels. Scale bars represent 20 μm.

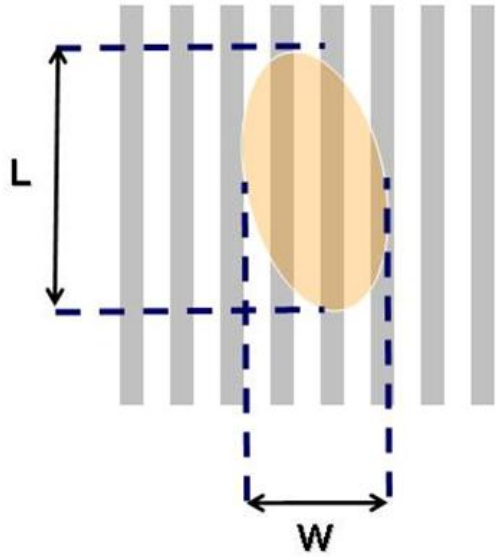

Figure 3-4. Measurements taken to calculate nuclear form factor where *L* is the length of the nucleus parallel to the ridges and *W* is the width of the nucleus orthogonal to the ridges.

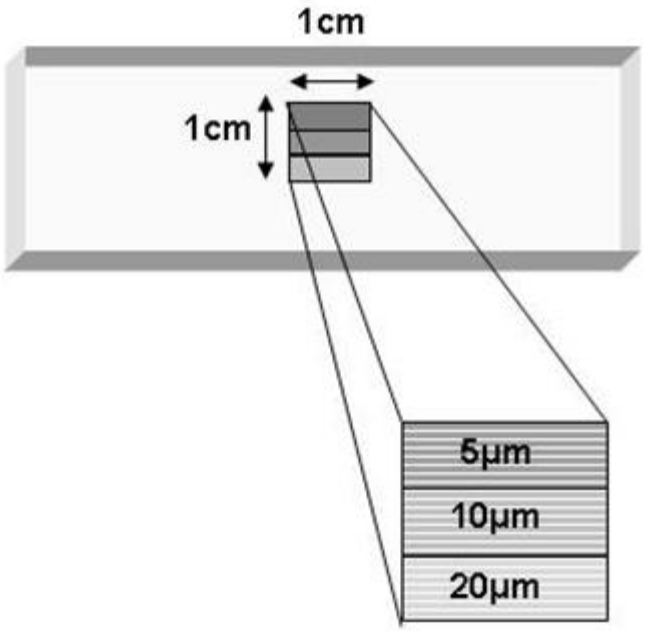

Figure 3-5. Layout of channel topographies. Each channel width (5, 10 and 20 μm) is contained within a 1 cm by 0.33 cm area.

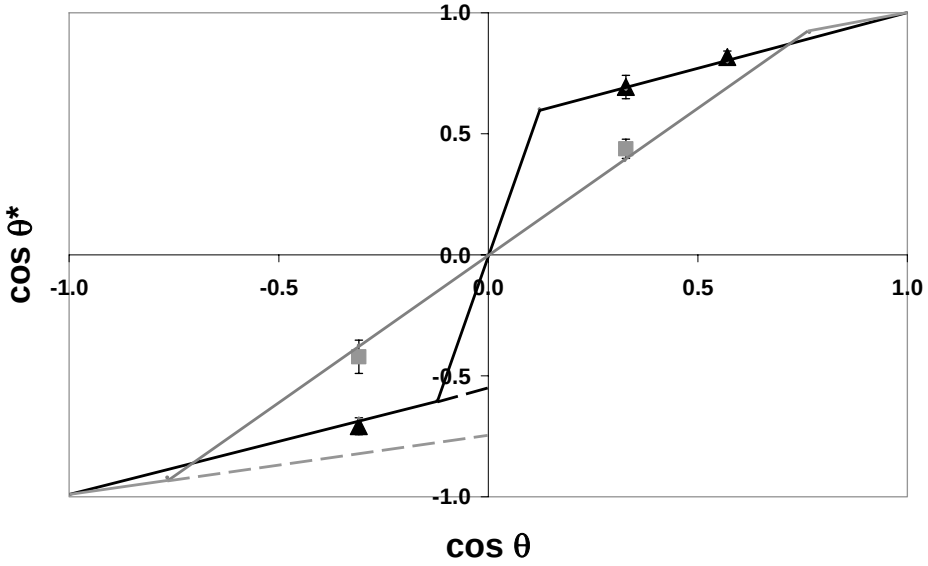

Figure 3-6. Change in wettability induced by the 20 μm spaced ridges (grey squares) and Sharklet AF™ (black triangles) topographies compared to smooth PDMSe. Both measured data and model predictions are given. Dashed lines are used to indicate the metastable air pocket state proposed by Quéré.

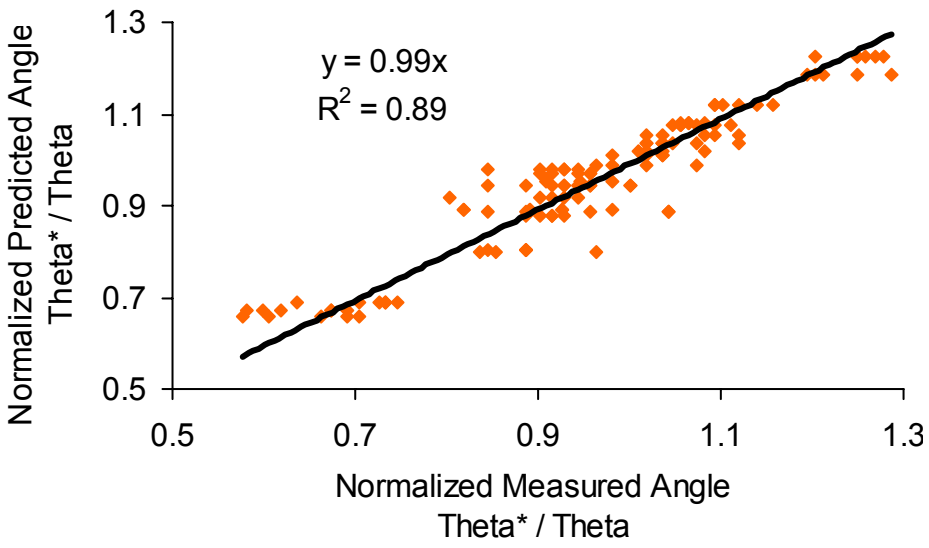

Figure 3-7. Comparison of contact angles predicted by the model to contact angles measured on the surfaces. Data were normalized with respect to contact angles on smooth PDMSe. Linear regression indicates a near 1:1 relationship (slope-0.99) with high correlation ($R^2 = 0.89$) to the data.

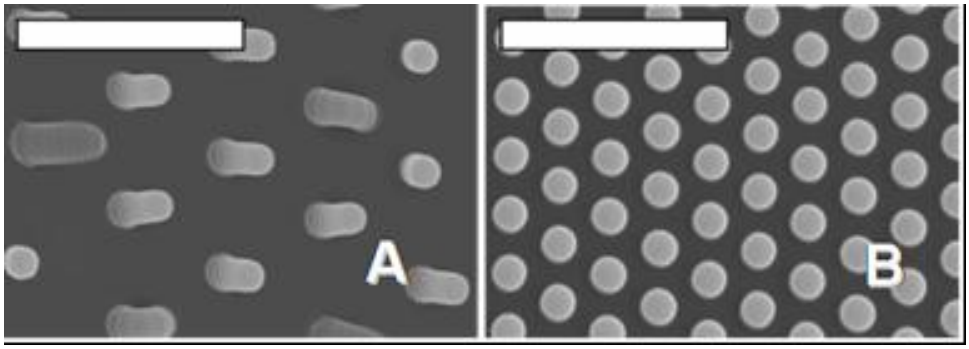

Figure 3-8. SEM images of 2 μm diameter pillars in PDMSe that are A) 5 μm high and 4 μm spaced and B) 3 μm high and 2 μm spaced. Increased height causes pillars to bend. Scale bars represent 15 μm.

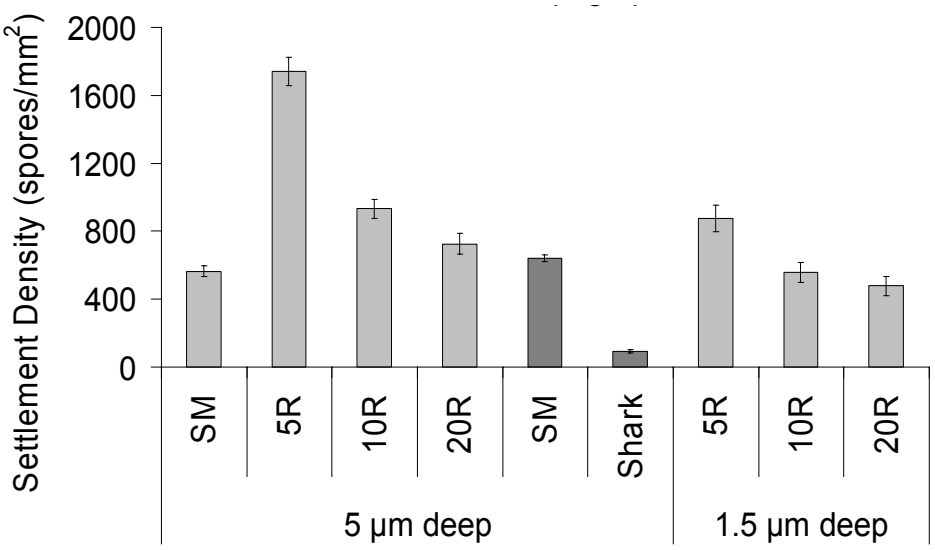

Figure 3-9. *Ulva* settlement on smooth (SM) and textured PDMSe. Topographies studied included the Sharklet AF™ (Shark) in addition to 5 µm wide ridges that were 5, 10, and 20 µm spaced (5R, 10R, and 20R) and either 1.5 or 5 µm high. The Sharklet AF™ topography was evaluated in a separate experiment as indicated by the darker bars. Error bars indicate ±2 standard errors of the mean. For all surfaces, counts are based on the mean of 90 counts, 30 from each of 3 replicates.

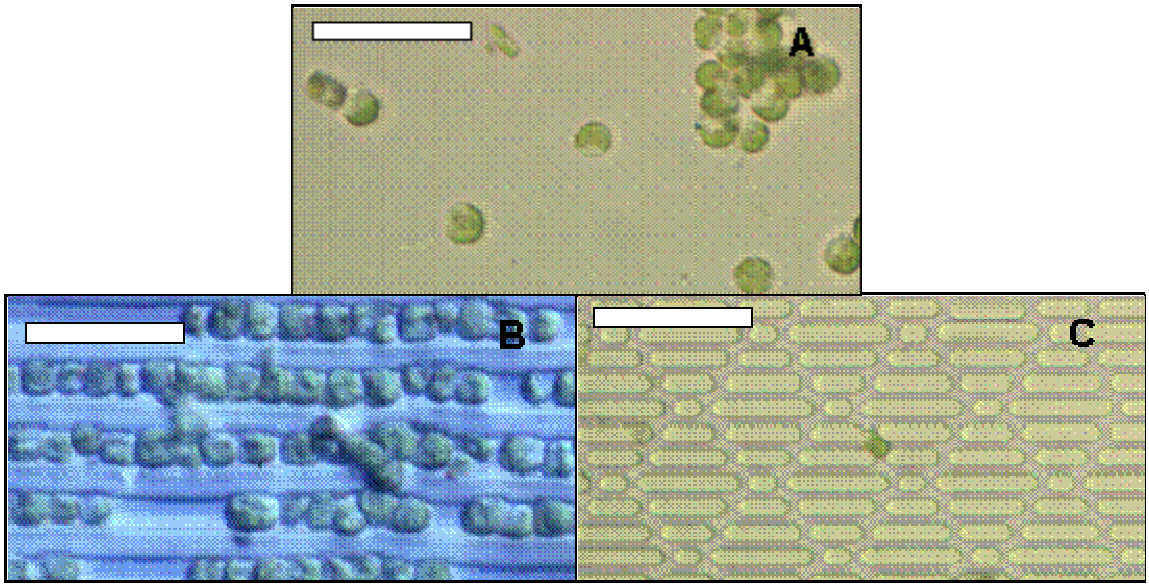

Figure 3-10. *Ulva* settled on smooth and textured PDMSe. A) Smooth. B) 5 µm wide, 5 µm spaced, and 5µm deep channels. C) 5 µm deep Sharklet AF™ in PDMSe. Images were taken via light microscopy. Scale bars represent 25 µm.

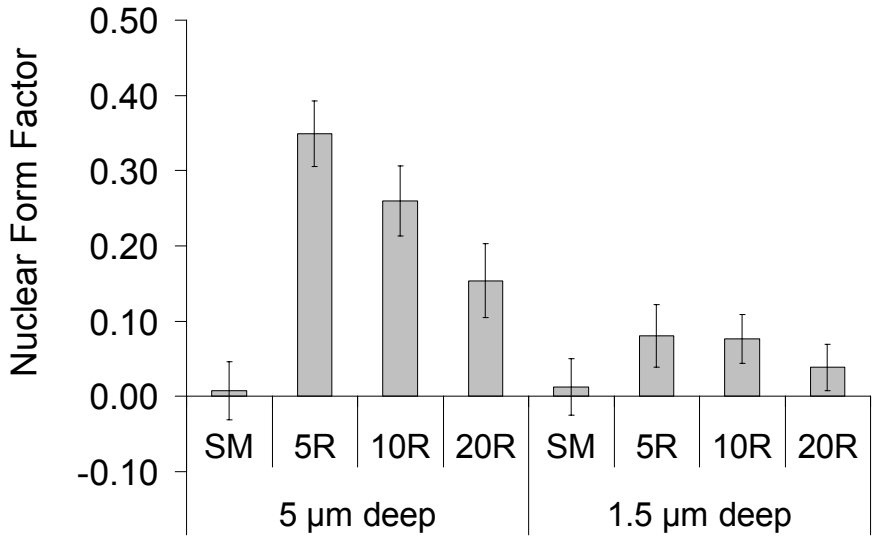

Figure 3-11. PVEC alignment on smooth (SM) and textured PDMSe. Topographies studied included 5, 10, and 20 µm spaced, 5 µm wide ridges (5R, 10R, and 20R) that are both 1.5 and 5 µm high. Error bars indicate ±2 standard errors of the mean.

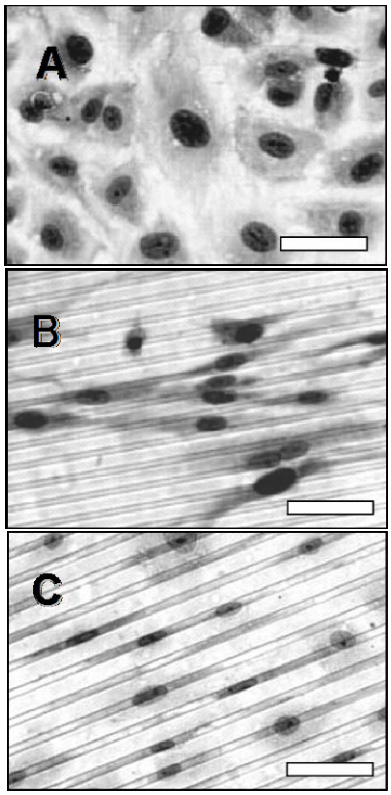

Figure 3-12. Endothelial cells grown on smooth and textured PDMSe. A) Smooth. B) 5 µm wide, 5 µm spaced, and 5 µm tall ridges. C) 5 µm wide, 5 µm spaced, and 1.5 µm tall ridges. Images have been processed to improve contrast. Scale bars represent 50 µm.

Table 3-1. Dimensions of Topographies Used in Wettability and Bioadhesion Studies

Feature	Height (μm)	Width (μm)	Spacing (μm)	Replication Type
Pillar	1.5	5	5	Positive
	1.5	5	10	
	1.5	5	20	
	5.0	5	5	
	5.0	5	10	
	5.0	5	20	
Pit	5.0	5	5	Negative
	5.0	5	10	
	5.0	5	20	
Channel	5.0	5	5	Negative
	5.0	10	5	
	5.0	20	5	
Ridge	1.5	5	5	Positive
	1.5	5	10	
	1.5	5	20	
	5.0	5	5	
	5.0	5	10	
	5.0	5	20	
Sharklet AF™	4.0	2	2	Negative

Table 3-2. Dimensions of Novel Theoretical Topographies

Feature	Height (μm)	Spacing(s) (μm)	Width(s) (μm)
Circular Pillars	1	2	2
	3	2	2
Triangle/Circles	1	2	2 10
	3	2	2 10
Star Pillars	1	2	4
	3	2	4
Square Pillars	1	1	2
	3	1	2
Ring Pillars	1	2	2
	3	2	2
Mixed Star Pillars	1	2	2 4
	3	2	2 4
Gradient Pillars	1	1 2 3 4	2
	3	1 2 3 4	2
Hexagon Pillars	1	2	20
	3	2	20
Channels	1	2	2
	3	2	2
Sharklet AF™	1	2	2
	3	2	2

Table 3-3. Measured Contact Angles on Microtopographies

Features	Spacing (μm)	f_1	r	Contact Angles (°)		
				Water	MeI	DMF
Smooth	-	1.00	1.0	108 ± 4	71 ± 6	55 ± 8
Pits	5	0.80	1.8	115 ± 2	65 ± 2	50 ± 8
	10	0.91	1.4	112 ± 2	69 ± 4	52 ± 4
	20	0.97	1.1	110 ± 6	65 ± 6	56 ± 6
Channels	5	0.50	2.0	133 ± 8	51 ± 2	39 ± 6
	10	0.67	1.7	121 ± 6	62 ± 4	49 ± 8
	20	0.80	1.4	116 ± 6	68 ±12	48 ± 6
Ridges	5	0.50	1.3	116 ± 8	63 ± 8	46 ± 4
	10	0.33	1.2	115 ± 8	63 ± 6	46 ± 8
	20	0.20	1.1	111 ± 6	66 ± 4	52 ± 8
Sharklet AF ™	2	0.47	5.0	135 ± 3[a]	46 ± 8	35 ± 2

[a]Indicates droplet would not settle on the surface and had to be captured with video

CHAPTER 4
CHARACERIZATION OF GLUTARALDEHYDE AND GENIPIN CROSSLINKED GELATIN FILMS

Introduction

Collagen is the primary protein component in bone, cartilage, skin and connective tissue. Collagen has been investigated for use as a biomaterial, but due to its antigenicity extensive further research would be needed to determine the impact on the immune system. Alternatively, gelatin has relatively low antigenicity. Gelatin is formed from denatured collagen, through heating or physical and chemical degradation of the protein to destroy the triple-helix structure. In the biomedical sector, gelatin is most commonly used for drug delivery capsules, wound dressings, adsorbent surgical pads, and vascular graft sealants.

Gelatin has the advantage of being a natural, biodegradable biopolymer. As such, upon implantation no cytotoxicity is evident and over time it can be resorbed and replaced with native collagen. At temperatures above 40°C, aqueous gelatin solutions exist in the solvated state allowing them to be cast into a variety of forms. At these elevated temperatures, the polypeptide exists as flexible single coils. Upon cooling, gelation takes place in which the triple helical structure of collagen is partially recovered. Gelation requires the concentration of gelatin in water to be above a certain critical minimum point, typically accepted to be between 0.4 and 1% by weight [103]. A hydrogel results, which allows for the transport of water and nutrients through the bulk.

The primary drawback of gelatin lies in poor mechanically stability. In creating a gelatin hydrogel, dry gelatin powder is mixed with water that has typically been heated to above 40ºC which is the denaturation point for native soluble collagen. Upon allowing the solution to cool, gelation occurs as there is a partial recovery of the collagen triple helix occurs along segments of the polymer chains. At the triple helix regions, three chains are combined to form a type of

crosslink. However, if gelatin is submerged in an aqueous environment long enough it will eventually dissolve completely. Consequently, crosslinking must be employed to improve mechanical stability. This is typically accomplished through chemical crosslinking with bifunctional aldehydes, diiosocyanates, carbodiimides, epoxy compounds and acyl azide methods [104]. Physical methods such as dehydrothermal treatment and ultraviolet and gamma irradiation have also been used [105-107]. The improvement of mechanical properties depends on the crosslink density and can be modeled using rubber elasticity theory. Briefly, as a rubber is stretched a retractive force is generated due to the decrease in entropy that occurs as the polymer chains become stretched. The basic equation that relates the retractive stress (σ) to the extension ratio (α) is given below:

$$\sigma = \frac{\rho}{M_c} RT\left(\alpha - \frac{1}{\alpha^2}\right). \tag{4-1}$$

In this equation, ρ represents density and M_c denotes the molecular weight between crosslinks. Although the stress-strain relationship is not linear, it is clear that increasing the crosslink density (which decreases M_c) results in higher modulus values.

Glutaraldehyde (GTA) is the most common crosslinker for gelatin systems and it primarily reacts with lysine and hydroxylysine amino acid residues. Although it reacts heterogeneously with gelatin (Fig. 4-1), it only requires one GTA molecule to form a crosslink. GTA efficiently stabilizes the biopolymer, but is known to exhibit localized cytotoxic effects as it is released during material degradation [5].

Genipin (GEN) provides an alternative to dialdehyde crosslinking. GEN is a natural crosslinker that is obtained from an extract (geniposide) of gardenia fruits. Two GEN molecules combine to form a single crosslink between primary amino groups (Fig. 4-2). The mechanism begins with a ring-opening condensation reaction with a primary amine [108] and is completed

with a dimerization reaction which may involve free radicals [109]. GEN has been shown to be nearly as efficient as GTA at stabilizing collagen-based biomaterials, but with a much lower associated cytotoxicity [110]. In comparison to GTA, GEN fixation of cell-free xenogenic vascular grafts results in the formation of a more consistent endothelial layer *in vivo* [111].

Attempts to generate microscale topographies in gelatin films have been limited. Yang et al produced gelatin ridges adhered to a glass substrate by modification of conventional photolithography techniques [112]. Briefly, gelatin was first spin coated onto glass and then photoresist was coated on top. UV photolithography was then used to generate the desired pattern in the photoresist and then the three-layer structure was immersed in GTA to crosslink the exposed regions of gelatin. The gelatin microtopgraphy was revealed after rinsing in acetone to strip away photoresist and immersion in hot water to remove uncrosslinked gelatin. The fidelity of the resulting patterns depended on both the line width (at least 5 μm) of the gelatin and spacing between features (at least 10 μm). Yu et al. produced parallel grooves (5-500 μm wide) in a chitosan-collagen-gelatin composite via photolithography and replication from a silicone intermediate [112]. Good reproducibility was achieved for dimensions greater than 10 μm.

In the present study, gelatin films were crosslinked with varying concentrations of GTA and GEN. These films were evaluated for their potential at producing stable microtextured cell culture substrates. Mechanical properties (tensile and swelling) were determined in addition to the ability to produce fine (~2 μm wide) microscale features.

Materials and Methods

PDMSe Mold Preparation

Smooth polydimethylsiloxane elastomer (PDMSe) wells were produced using Dow Corning Corporation's Silastic T-2. The resin and curing agent were mixed in a 10:1 ratio,

degassed and poured over two 3 inch by 2 inch microscope slides that were adhered to one another. Large top and bottom glass plates separated by 5 mm spacers were used to ensure a flat surface on the back of the wells (Figure 4-3). The PDMSe was allowed to cure for 24 h at room temperature and then removed from the mold. Excess silicone was cut away, leaving about a 1cm border around the well

Topographically patterned PDMSe molds were prepared in a two-step curing process (Fig. 4-4). First, PDMSe (10:1 ratio of base resin to curing agent) was cast directly from topographically modified silicon wafers. The wafers were prepared using standard photolithography techniques (processing performed by James Schumacher). Wafers were prepared using deep reactive ion etching (DRIE) as previously described in Chapter 3. The target dimensions of the topography were 2 μm wide channels separated by 2 μm wide ridges that are 1 μm tall. For the wafers, the channels are etched into the surface and are therefore considered to be negative features. When PDMSe is cast against the wafer, channels replicate as ridges protruding out from the surface and so the topography is inverted.

In an initial cure step, PDMSe was then cast against clean wafers within a glass mold with spacers to give ~0.5 mm thick PDMSe film. Cured films were then removed from the wafers and the desired pattern portion cut out leaving ~2 mm thick border of smooth PDMSe around the edges. Two 2 in x 3 in glass microscope slides were adhered to one another and then treated with hexamethyldisilazane via vapor deposition. The textured film was then suctioned pattern-side down to the center of the microscope slides. This was then placed on a clean HMDS-treated glass plate with 3 mm spacers at the corners of the plate. Approximately 120 g of PDMSE was mixed, degassed and poured over the film and slides and a second clean, HMDS treated glass plate was laid over top. The PDMSe was allowed to cure overnight at room temperature before

being removed from the mold. Excess silicone was then cut away, leaving ~1 cm border of smooth PDMSe around the well.

Gelatin Film preparation

Gelatin derived from bovine calf skin was supplied as a dry powder (Sigma). Uncrosslinked gelatin films were prepared by first dissolving the powder in 50°C nanopure water at a 10% (wt/v). For each film, 8 mL of the heated gelatin solution was poured into a 50.8 mm by 76.2 mm by 2 mm PDMSe well. A clean glass slide was then across the well in order to level the solution. A desiccator lid was placed above the well in order to slow evaporation of the water. The film was allowed to dry for 24 hours at room temperature.

GTA and GEN were used to stabilize smooth gelatin films. Four GTA concentrations were investigated: 2.2, 3.2, 4.3 and 9.1 wt/wt% which correspond to 2.9, 4.3, 5.9 and 13% molar equivalents (% MEQ), respectively. GEN crosslinking was carried out at 3 different crosslinker concentrations: 4.8, 9.1 and 13 wt/wt% (1.4, 2.9 and 4.3% molar equivalents). Molar equivalents are based on a molecular weight of $1.2x10^5$ g/mol for gelatin as previously measured by Cuevas [94]. The average molecular weight of repeat units was assumed to be 65 g/mol.

GTA crosslinking was performed on partially dried gelatin films. Five hours after initial casting of uncrosslinked gelatin, 4 mL of an appropriate GTA solution was pipetted on top of the film (Figure 4-5). The desiccator lid was then placed above the well and the GTA was allowed to react overnight at room temperature.

GEN crosslinking was carried out by bulk mixing. GEN was first dissolved in nanopure water and heated to 50°C. Gelatin was then slowly added while mixing to a final concentration of 10% (wt/v). The solution was then placed in a 50°C oven for 5 minutes to ensure the gelatin completely dissolved. For each film, 8 mL of the heated gelatin-GEN solution was poured into a 50.8 mm by 76.2 mm by 2 mm PDMSe well. A clean glass slide was then across the well in

order to level the solution. A desiccator lid was placed above the well in order to slow evaporation of the water. The film was allowed to react and dry for 24 hours at room temperature. In addition to the smooth films, a topographically patterned GEN crosslinked gelatin film (2.9 % MEQ) was also prepared. The topography included 2 μm wide channels formed between 2 μm spaced ridges that were 1 μm tall.

Soxhlet Extraction of Gelatin

For some studies, gelatin films were Soxhlet extracted in nanopure water for 72 hours to remove residual unreacted GEN. Samples were then immersed in fresh nanopure water and allowed to equilibrate for 24 hours before mechanical tests were performed.

Postcuring of Gelatin

In order to evaluate the thermal stability of GEN crosslinked gelatin exposed to moderate heat, two films of each GEN concentration were immersed in water and placed in a 50°C oven for 3 hours. Samples were then immersed in fresh nanopure water and allowed to equilibrate for 24 hours before mechanical tests were performed.

Mechanical Testing

Samples for tensile testing were cut using an ASTM D1822-68 type L dog bone die (1 in gauge length and 3.1 mm cross-sectional width). Three specimens were cut from each gelatin film. Samples were tested using an Instron 4301 with Series IX software. All samples were tested at a crosshead speed of 50.8 mm/min (2 in/min). Additionally GEN-crosslinked samples without post-processing (Soxhlet extraction or postcuring) were tested at a second, slower crosshead speed of 5 mm/min to determine the effect of strain rate. Pneumatic grips were used with the pressure set to 24 psi.

Swelling Study

Swelling studies were carried out in order to further characterize the abilities of GTA and GEN to stabilize gelatin films. A 12 mm diameter circular punch was used to cut out samples from smooth, hydrated films. Four samples of each type were punched. Samples were placed in the oven at 50ºC for 3 hours to dry and the initial weight of each sample disc was measured. Samples were placed in individual wells of 12-well culture plates. Then 3 mL of nanopure water was added to each well. At ten time points (5, 10, 15, 20, 30, 60, 120, 240, 1200 and 10000 min) the water uptake in the gelatin samples was measured. For each time point, samples were removed from water and their surfaces blotted dry with a task wipe. Each sample was then immediately weighed to determine the hydrated weight. Percent swelling was then calculated by comparing the hydrated (W_t) and initial dry weights (W_o) according to the following equation:

$$\%Swelling \equiv \frac{W_t - W_o}{W_o} * 100\% . \qquad (4\text{-}2)$$

After the swelling study was complete, samples were dried for 3 hours at 50ºC and the final dry weights (W_f) taken. The mass change of the samples throughout the study was then calculated by substituting W_f for W_o in Equation 4-2.

Evaluation of Microscale Gelatin Features

The fidelity of the topographically patterned gelatin film was evaluated using white light interference profilometry. A Wyko model NT1000 profilometer coupled with Vision 32 software was used for all measurements. The microscope has 2 lenses: the exterior objective that was available in three magnifications namely 5X, 20X and 50X and the internal 'field of view' (FOV) lens which was available in 0.5X, 1X and 2X magnifications. High resolution was needed for the present study and so the 50X external objective and 2X FOV were used for a combined magnification of 100X.

Profilometry was performed on both dry (ambient conditions for 24 h) and rehydrated (immersed in nanopure water for 24 hours) gelatin films. The surface of the rehydrated film was blown dry with nitrogen gas immediately preceding testing. The Vision 32 software was used to measure the channel dimensions (width, spacing and height). Six measurements per dimensions were taken at random across the sample.

Statistical Analysis

Results are reported as mean values with 95% confidence intervals. For each study, one way analysis of variance ($\alpha = 0.05$) was used to determine if any significant differences among the treatment means existed. As appropriate, Tukey's multiple comparisons test was used to determine which treatments were significantly different.

Results and Discussion

Mechanical Testing of Gelatin Films

Tensile testing of GEN and GTA crosslinked gelatin films indicated that the mechanical properties are influenced by the concentration of crosslinker. As crosslinker concentration is increased, the stress-strain curves become steeper (Fig. 4-6), indicating stiffness is increased. For both GEN and GTA, the initial Young's modulus of the gelatin increased significantly with increased crosslinker concentrations (Fig. 4-7). Interestingly, both chemistries were equally efficient at stabilizing the gelatin in terms of modulus. No significant differences existed between GEN and GTA at concentrations of 2.9 and 4.3% MEQ. Mean moduli values were ~120 and ~155 kPa, respectively, for these two concentrations. This contradicts results published by Cuevas which state GEN is significantly more efficient at crosslinking gelatin [113]. The reason for the difference is not immediately clear, but might be attributed to differences in the length of storage of GEN. Increasing the GTA concentration to 5.9% MEQ led to a significant increase in modulus with a value of 280 ± 14 kPa. A direct comparison with

GEN could not be made at this concentration. A 5.9% MEQ GEN crosslinked gelatin film could not be produced due to GEN's low solubility in water (slightly less than 0.02 g/mL).

Elongation at break for gelatin was also affected by crosslinker concentration. An increase in crosslinker amount tended to decrease the elongation at break (Fig. 4-8). Significant differences for the mean elongation values were observed for the highest and lowest concentrations of both GEN and GTA. Elongation values across all treatments ranged from 42 ± 9% to 82 ± 16%. As with modulus, elongation did not differ significantly among the GEN and GTA samples at either 2.9 or 4.3 % MEQ.

Ultimate tensile strength (also known as break stress) did not vary significantly with crosslinker amount or chemistry (Fig. 4-9). GTA tended to increase the ultimate tensile strength compared to GEN, particularly at a concentration of 2.9 % MEQ. However, high variability in the data prevented definitive conclusions.

Mechanical testing of GEN crosslinked gelatin was carried out at both 5 mm/min and 50.8 mm/min (2 in/min) strain rates in order to determine how the time scale of perturbations affects the mechanical stability of the gelatin. No obvious differences were observed between the characteristic stress-strain curves for the two strain rates at any of the crosslinker concentrations (Fig. 4-10). Similarly, the initial Young's modulus did not vary significantly with strain rate either (Fig. 4-11).

The thermal stability of GEN crosslinked gelatin was evaluated by processing samples by two methods. The 50ºC postcure for 3 hours did not significantly affect the gelatin at GEN concentrations of 2.9 and 4.4% MEQ (Fig. 4-12). However, at 1.4% MEQ the initial Young's modulus was decreased significantly by the heat, lowering the modulus from 98 ± 19 to 67 ± 3 kPa. Soxhlet extraction significantly reduced the initial modulus for all GEN

concentrations. In particular, the 1.4% MEQ GEN crosslinked gelatin samples were so degraded that the films fell apart under their own weight and dog bone specimens could not prepared. At 2.9 and 4.3% MEQ of GEN, Soxhlet extraction of the samples resulted in ~50% reduction of the initial Young's modulus.

Swelling Studies of Gelatin Films

The goal of this chapter was to choose an optimum crosslinker for later cell studies with topographically modified gelatin. With this in mind, it was necessary to limit the swelling of gelatin over time when immersed in aqueous environments. Dried samples of GEN and GTA crosslinked gelatin were immersed in nanopure water for up to 7 days and their percent swelling was plotted with time (Fig. 4-13). The GEN crosslinked samples tended to level off more quickly and at a lower swelling percentage than the GTA samples.

For both GEN and GTA, increasing the concentration of crosslinker resulted in a decrease in swelling. By 1200 min (20 h), the only treatments that did not significantly differ in the degree of swelling were 1.4% MEQ GEN and 5.9% MEQ GTA (Fig. 4-14). With the exception of these two, all of the GTA samples swelled to a greater extent than all of the GEN samples. The swelling of GEN crosslinked samples decreased from 360 ± 20% to 100 ± 10% as the crosslinker concentration increased from 1.4 to 4.3% MEQ. Similarly, the swelling of GTA crosslinked samples decreased from 520 ± 10% to 370 ± 20% across a range of 2.9 to 5.9% MEQ of the crosslinker. These results suggest that GEN samples would be better than GTA samples at maintaining the fidelity of microscale topographies during culture

The transport of water through each film was evaluated assuming Fickean diffusion. The diffusion coefficient (D) was determined by the following equation which is based on Fick's 2nd law [114, 115]:

$$\frac{W_t}{W_\infty} = \left(\frac{4Dt}{\pi l^2}\right)^{1/2}. \quad (4\text{-}3)$$

In this equation, W_t and W_∞ represent the mass of water in the hydrogel at time t and infinite time respectively. D is the diffusion coefficient and l is the average thickness of the gel during the swelling study. The diffusion coefficient for each sample was calculated from the slope of a linear regression to W_t/W_∞ versus the square root of time (Fig. 4-15). It is important to note that the weight of the GTA crosslinked gelatin samples leveled off between 480 and 1200 minutes (4 and 20 h) but underwent a sharp weight increase between 1200 and 10000 minutes (roughly 1 and 7 days). This suggests that the network of the material underwent degradation during this time period and so the infinite weight time point was selected to be 1200 minutes to exclude the effects of degradation. The diffusion coefficient of gelatin did not significantly vary with type or concentration of crosslinker used (Table 4-1). The average diffusion coefficient was 13 ± 2 $\mu m^2/s$.

To further evaluate the diffusion kinetics, a generalized rate equation was used to determine whether Fickean diffusion was rate determining mode of mass transport. The equation used was as follows [114, 116]:

$$\frac{W_t}{W_\infty} = kt^n. \quad (4\text{-}4)$$

The term k is a characteristic constant of the gel and n is a characteristic exponent which depends on the primary mode of transport of the penetrant. Fickean kinetics defines n = 0.5. Values of n between 0.5 and 1.0 indicate that the desorption process is non-Fickean. The characteristic exponent, n was calculated from the slope of the linear regression of log (W_t/W_∞) versus the log of time (Fig. 4-16). The values for n varied significantly with crosslinker type but not concentration (Table 4-1). The value of n was 0.39 ± 0.07 for GEN samples and 0.50 ± 0.06

for GTA samples. This suggests the rate of diffusion of water through GTA crosslinked gelatin is governed by Fickean diffusion, whereas other processes are significant for GEN crosslinked gelatin. The value of n might have been decreased because of a desorption of unreacted genipin

In order to determine if GEN and GTA crosslinked gelatin degrades or leaches crosslinker into the water, the weights of dried samples before and after the 7 day swelling study were compared (Fig. 4-17). The mass loss of GTA crosslinked samples was 7.4 ± 0.9% and it did not vary significantly with crosslinker concentration. In contrast, the mass loss of GEN crosslinked samples increased with increasing crosslinker concentration. The 4.3% GEN samples exhibited a 20.2 ± 2.3% mass loss, which was significantly greater than that of 1.4% and 2.9% GEN samples which lost 11.9 ± 5.4% and 14.7 ± 1.2% respectively. Some of the mass loss is likely due to the leaching of unreacted genipin from the gelatin into water. The total mass loss is similar to the amount of GEN in the original film, which suggests that at least some of the change in mass is due to a loss of gelatin.

Evaluation of Microscale Gelatin Features

GEN (2.9% MEQ) crosslinked gelatin was able to replicate the 2 μm wide microchannels as shown in the profilometry images (Fig. 4-18). Feature widths did not vary significantly from the silicon wafer master, with both substrates having channel widths of 2.3 to 2.4 μm and ridge widths of 1.6 to 1.7 μm (Table 4-1). Feature depths were not as accurately replicated. Compared to the silicon wafer, channel depth decreased from 0.90 ± 0.02 μm to 0.77 ± 0.02 μm for dehydrated gelatin. The features in the rehydrated gelatin appeared even shallower with a depth of 0.55 ± 0.01 μm. However, the true rehydrated feature height may have been larger. Because the profilometry measurements were taken in air, water from the bulk of the gelatin may have diffused to the surface and partially filled the channels. The replication of the feature depths could possibly be improved if the PDMSE mold were hydrophilically modified prior to

casting the gelatin. This could be accomplished either through plasma treatment or acid immersion and would allow the gelatin to fully wet the contours of the PDMSe.

Conclusion

Both GEN and GTA stabilized the gelatin films. For equal crosslinker concentrations (% MEQ), GTA provided a slight advantage at improving tensile properties (similar modulus but longer elongation at break), but GEN was significantly better at stabilizing gelatin against swelling in water. Although GEN is known to be less cytotoxic than GTA, some concern remains about whether cells will grow on the GEN crosslinked gelatin surfaces. Swelling studies indicate that unreacted genipin will likely be leached from the gelatin samples. Soxhlet extraction in water was not found to be an acceptable method of removing residual unreacted GEN from gelatin because the mechanical properties of the films deteriorated too much. As such, the 2.9% MEQ GEN was chosen as the best crosslinker concentration to proceed with into cell culture work because it should provide the best trade-off of enhancing tensile properties and resistance to swelling while minimizing the amount of unreacted GEN. Topographically modified gelatin films crosslinked with 2.9% MEQ GEN were found to replicate 2 μm wide features adequately, although the PDMSe mold would need to be hydrophilically modified in order for feature depth to be replicated accurately.

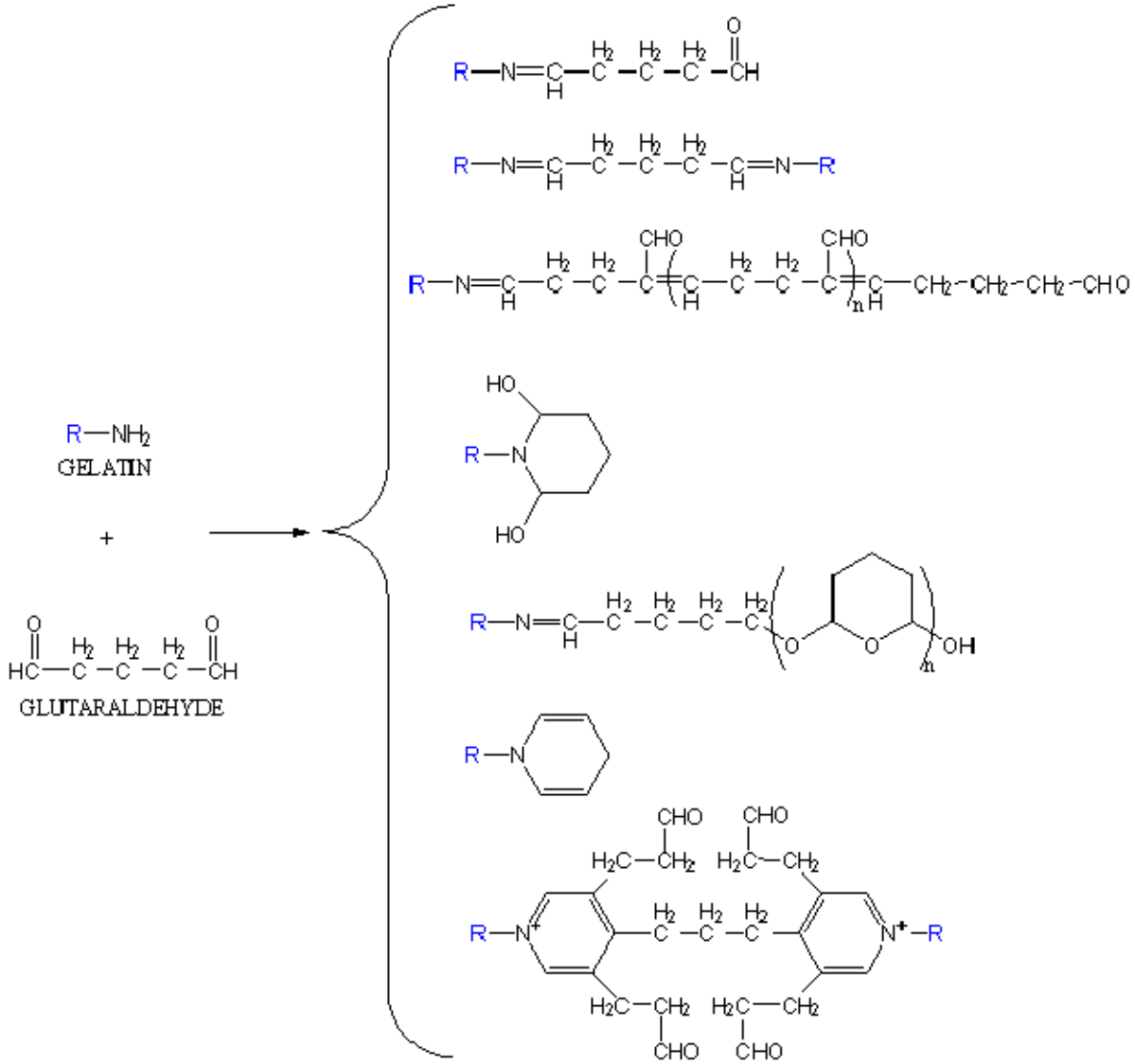

Figure 4-1. Chemical Reactions between gelatin and glutaraldehyde [117].

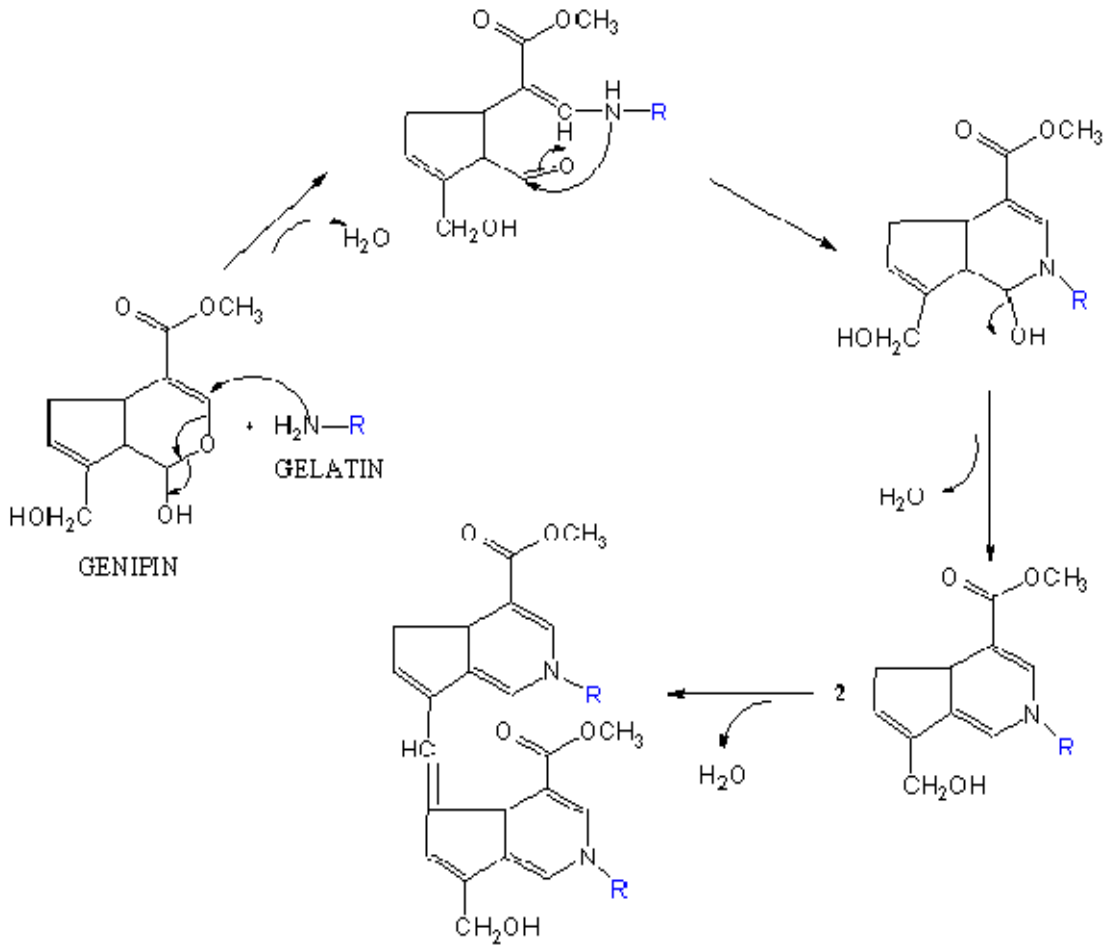

Figure 4-2. Crosslinking mechanism of genipin [108, 109, 118].

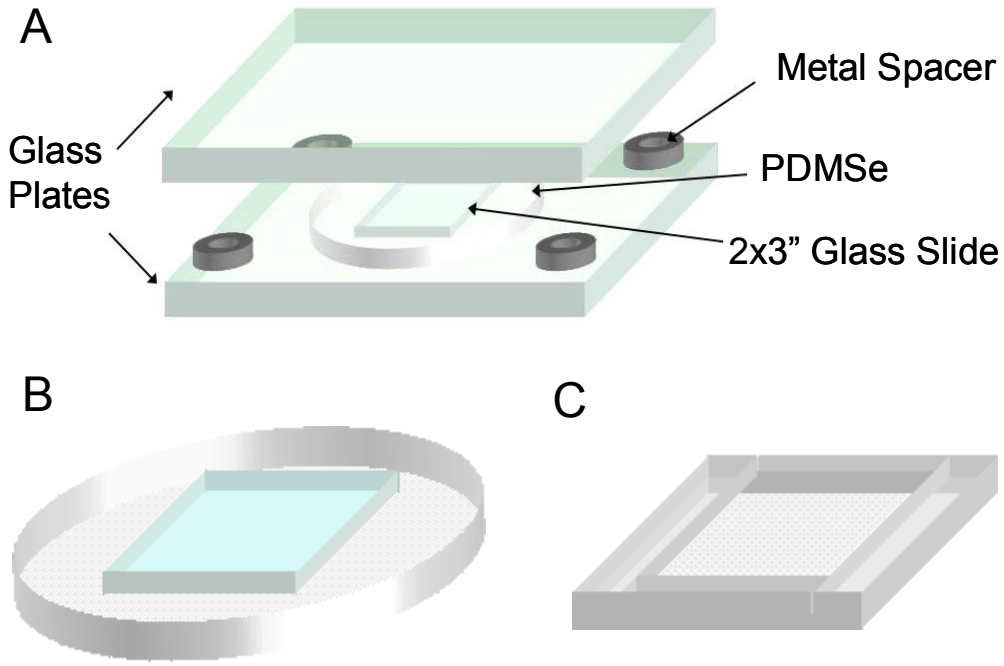

Figure 4-3. Mold design for creating smooth PDMSe wells for casting gelatin. A) Pour PDMSe over 2 in by 3 in glass slides and allow ot cure in the glass mold shown. B) Remove PDMSe and slide from the mold. C) Peel away slide an cut out well.

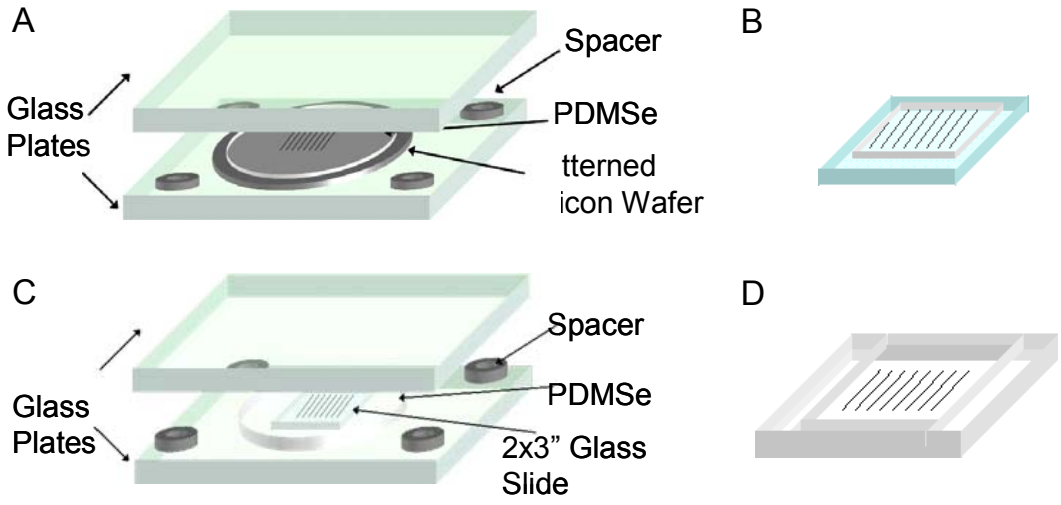

Figure 4-4. Process for preparing topographically patterned PDMSe wells. A) Cure PDMSe against patterned wafer. B) Suction patterned PDMSe to glass slides. C) Pour fresh PDMSe on top and allow to cure. D) Remove PDMSe from mold and cut out the well.

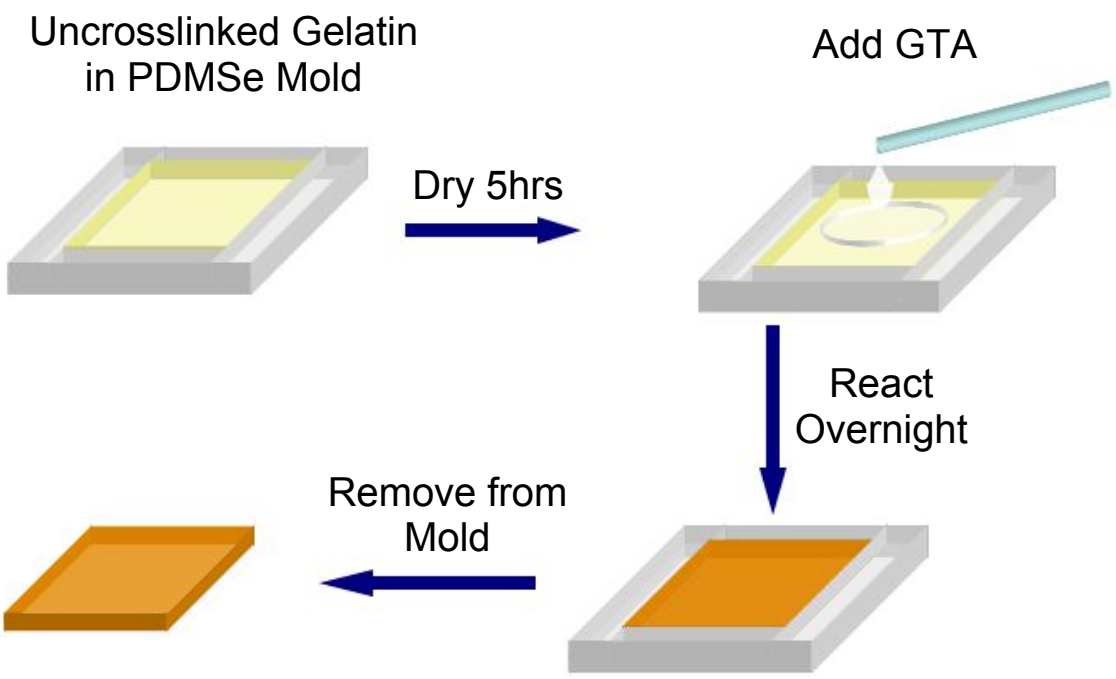

Figure 4-5. Process for crosslinking gelatin films with glutaraldehyde.

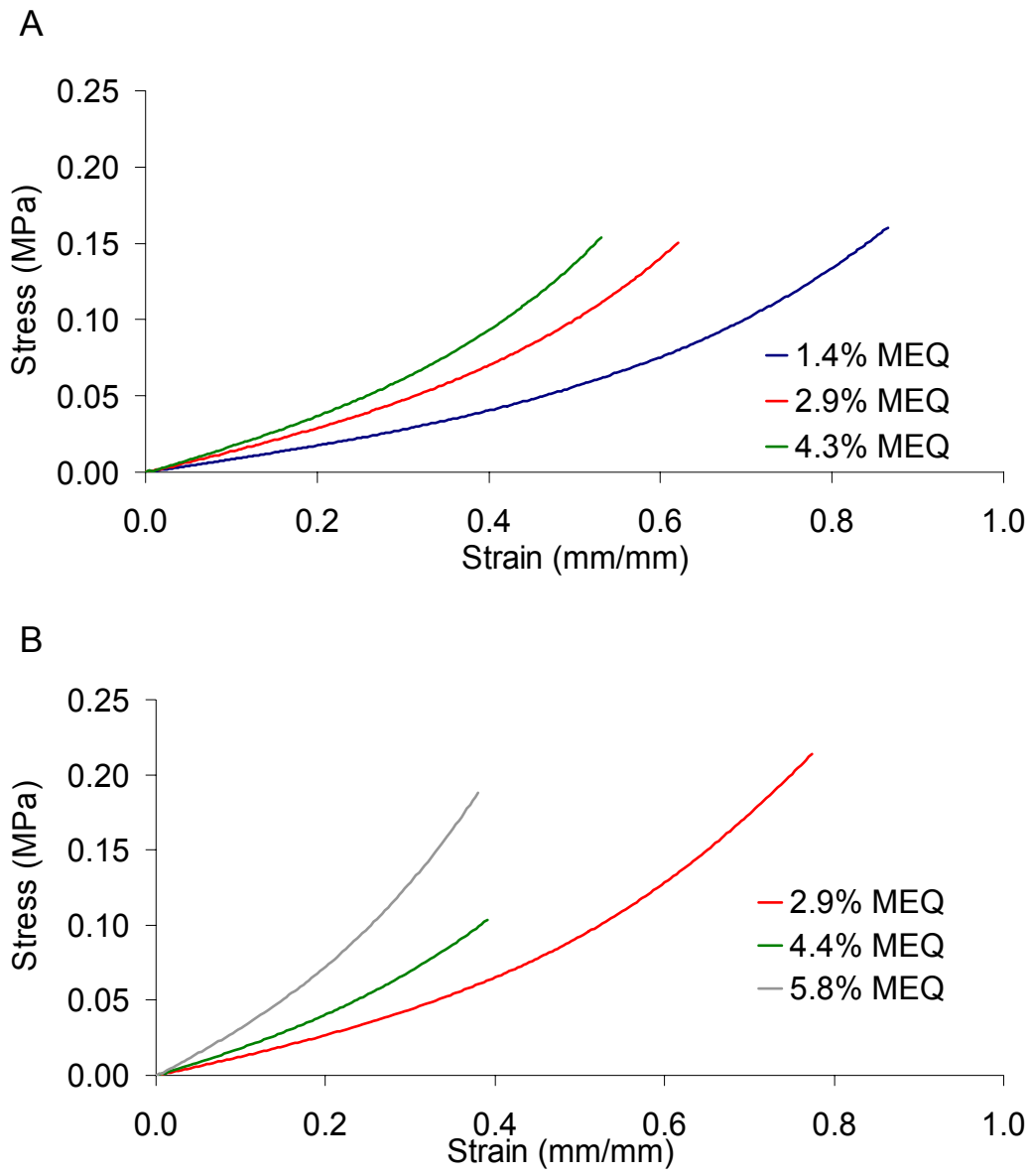

Figure 4-6. Representative stress-strain curves for GEN and GTA crosslinked gelatin. A) GEN crosslinked gelatin. B) GTA crosslinked gelatin. Tensile testing was carried out at a crosshead speed of 50.8 mm/min (2 in/min).

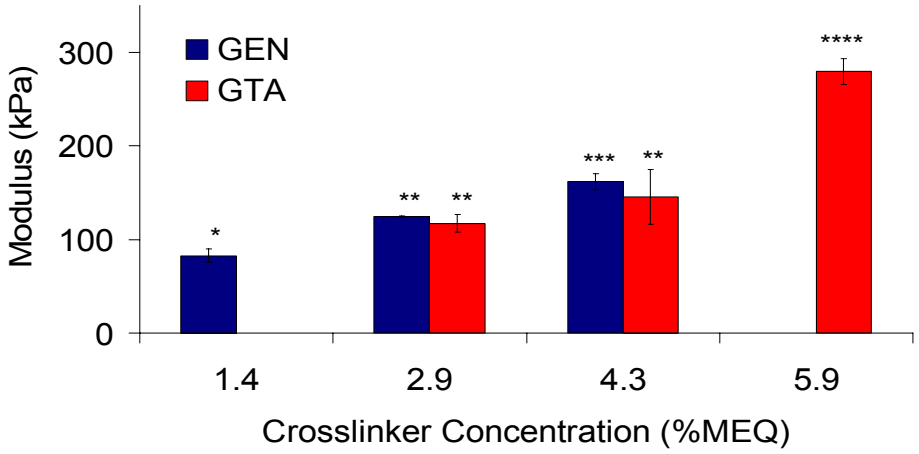

Figure 4-7. Initial Young's modulus versus crosslinker concentration for GEN and GTA crosslinked gelatin. Tensile testing was performed at a crosshead speed of 50.8 mm/min (2 in/min). Asterisks denote groups with means that are not statistically different (Tukey's Test, $\alpha = 0.05$).

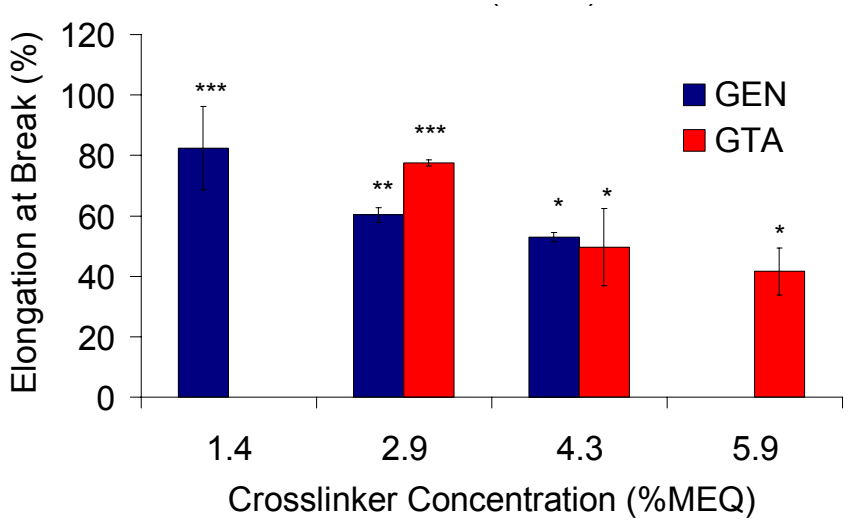

Figure 4-8. Elongation at break versus crosslinker concentration for GEN and GTA crosslinked gelatin. Tensile testing was performed at a crosshead speed of 50.8 mm/min (2 in/min). Asterisks denote groups with means that are not statistically different (Tukey's Test, $\alpha = 0.05$).

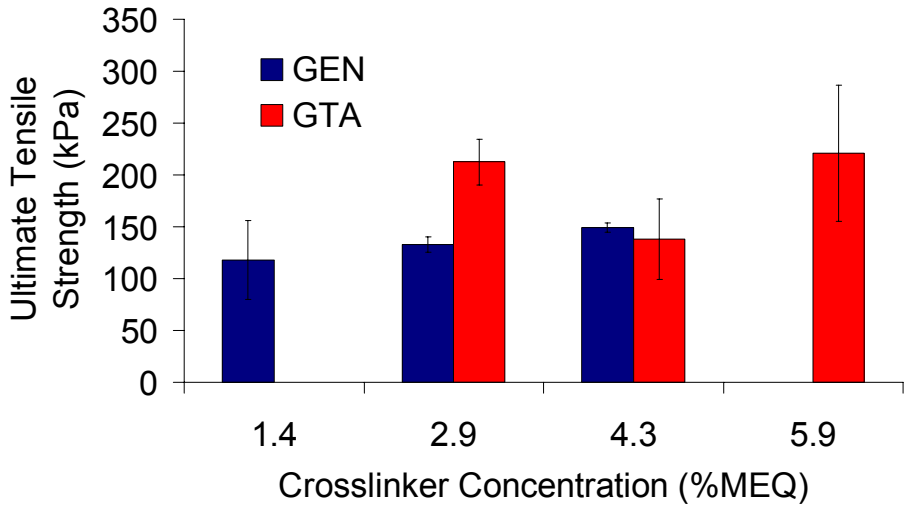

Figure 4-9. Ultimate tensile strength versus crosslinker concentration for GEN and GTA crosslinked gelatin. Tensile testing was performed at a crosshead speed of 50.8 mm/min (2 in/min). Significant differences did not exist among any of the means (Tukey's Test, $\alpha = 0.05$).

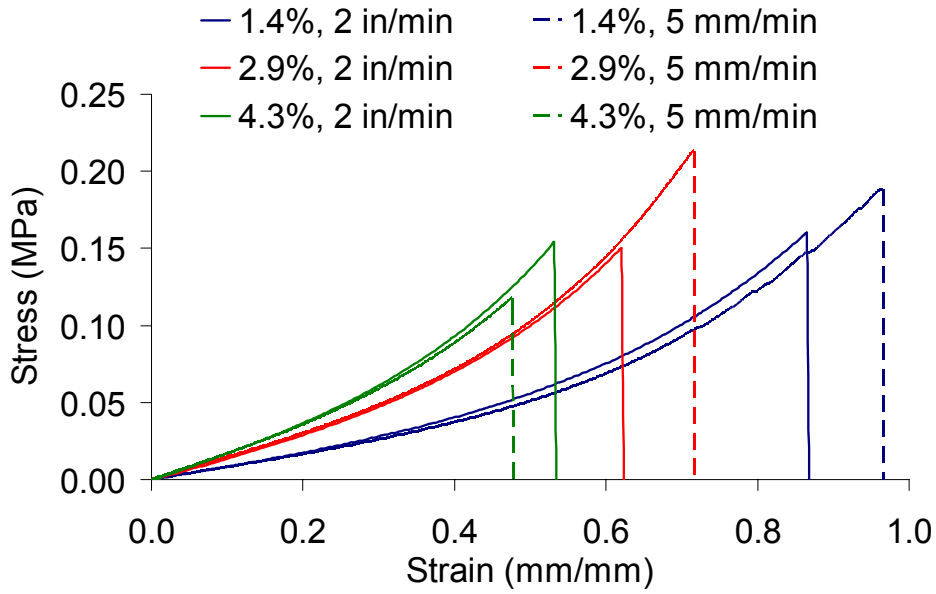

Figure 4-10. Stress-strain curves of GEN and GTA crosslinked gelatin. Testing was performed at 2 in/min (solid lines) and 5 mm/min (dashed lines).

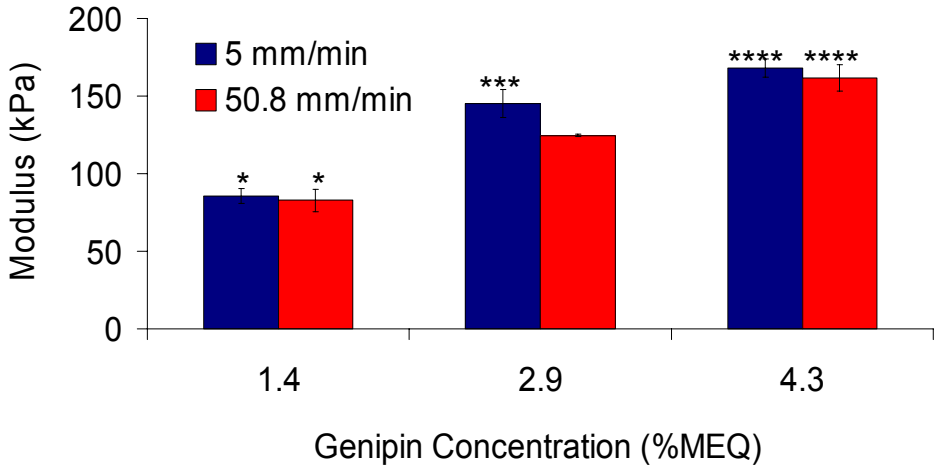

Figure 4-11. Effect of strain rate on the initial modulus of GEN crosslinked gelatin. Asterisks denote groups with means that are not statistically different (Tukey's Test, $\alpha = 0.05$).

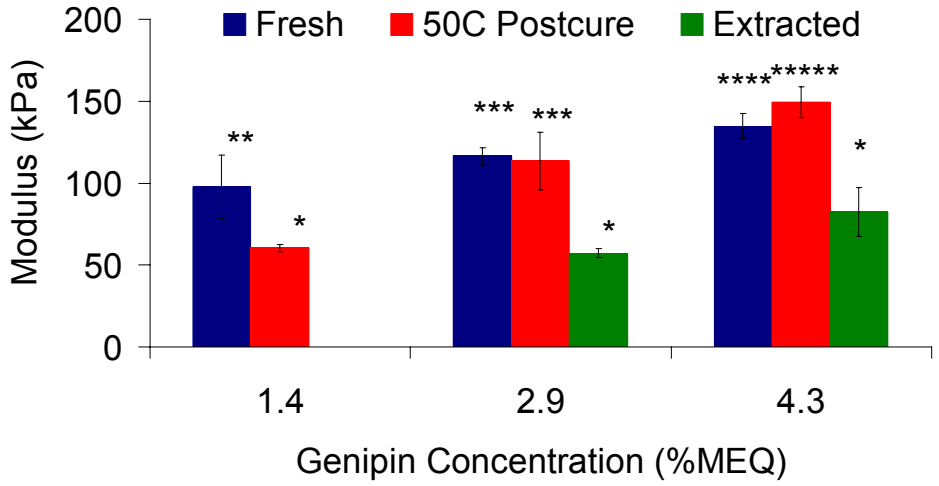

Figure 4-12. Effects of post-processing on the initial modulus of GEN crosslinked gelatin. Samples were tested without post-processing (Fresh), after heating for 3 h in a 50ºC oven while immersed in water (50ºC Postcure), or after being Soxhlet extracted in water for 72 h (Extracted). Mechanical testing was performed at a crosshead speed of 50.8 mm/min (2 in/min). Asterisks denote groups with means that are not statistically different (Tukey's Test, $\alpha = 0.05$).

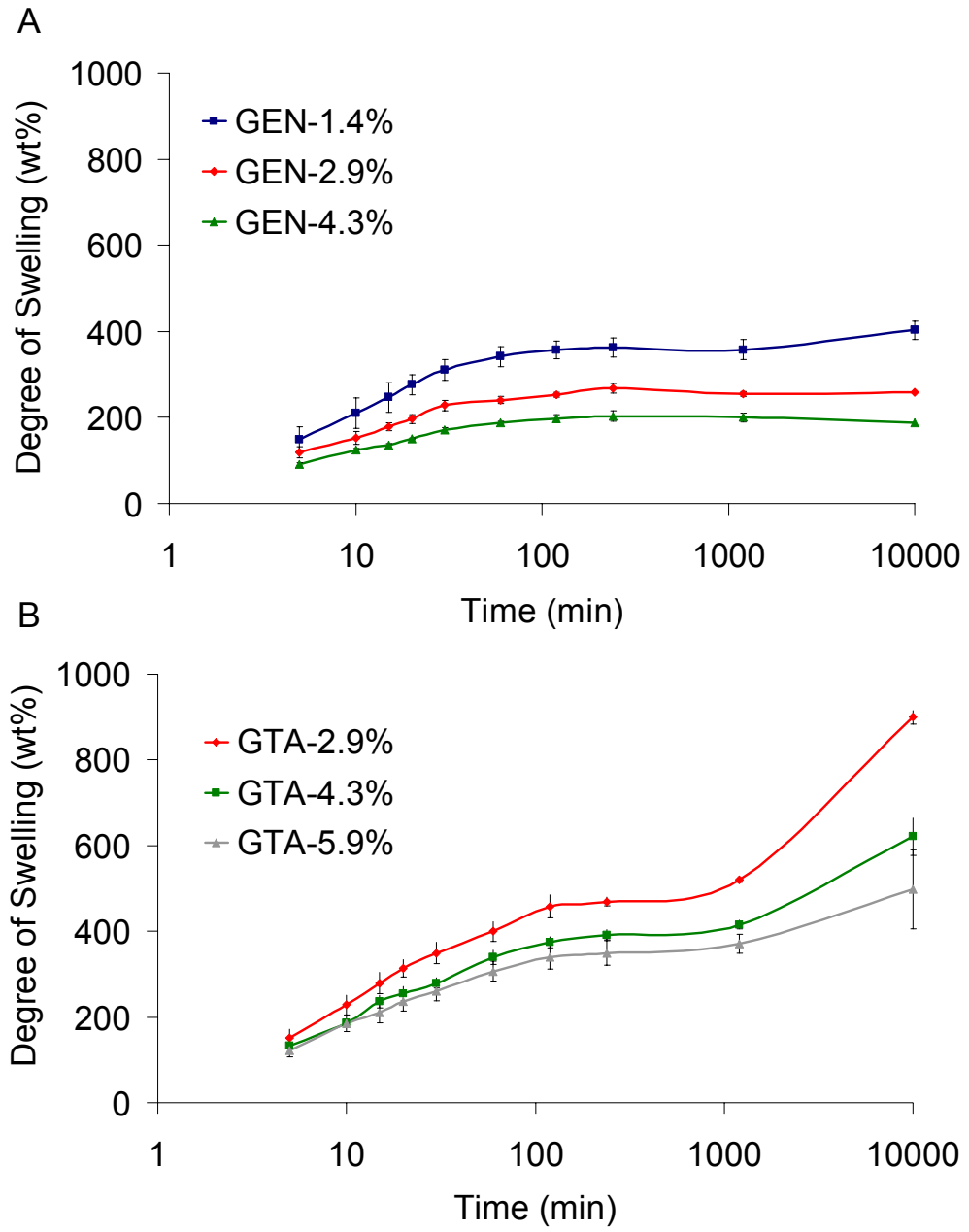

Figure 4-13. Swelling of GEN and GTA crosslinked gelatin for 7 days in water. A) GEN crosslinked gelatin. B) GTA crosslinked gelatin. Samples were initially dried overnight in a 50ºC oven. Error bars represent ±2 standard errors.

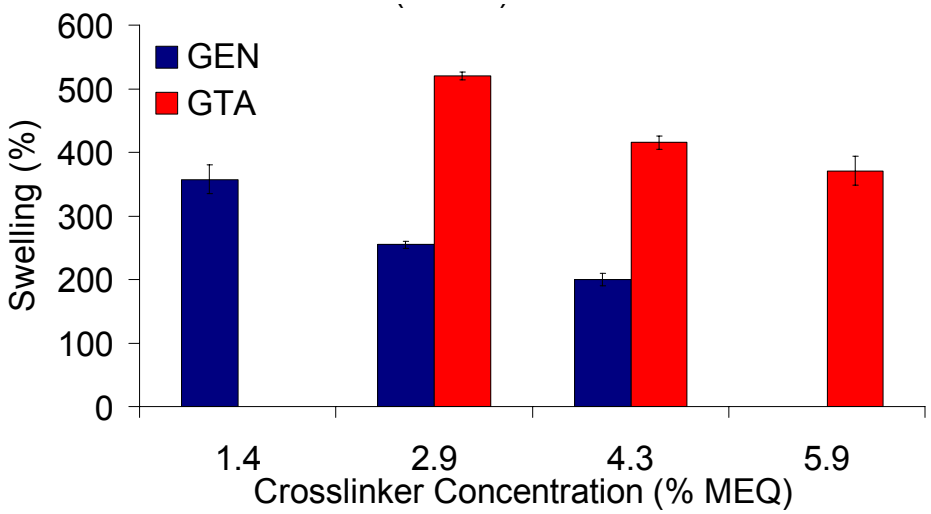

Figure 4-14. Swelling at 20 h of GEN and GTA crosslinked gelatin films. Swelling was carried out in nanopure water for 20 h. All sample means are significantly different from one another (Tukey's Test, $\alpha = 0.05$).

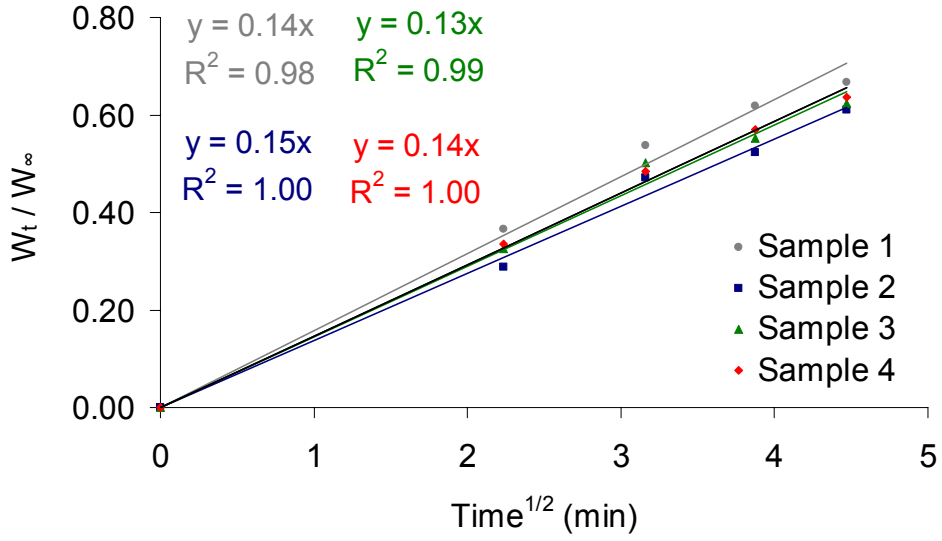

Figure 4-15. Representative plot used to calculate diffusion coefficients. Fractional water uptake (Wt/W∞) is plotted against the square root of time. The diffusion coefficient is calculated from the slope of this plot according to Equation 4-3.

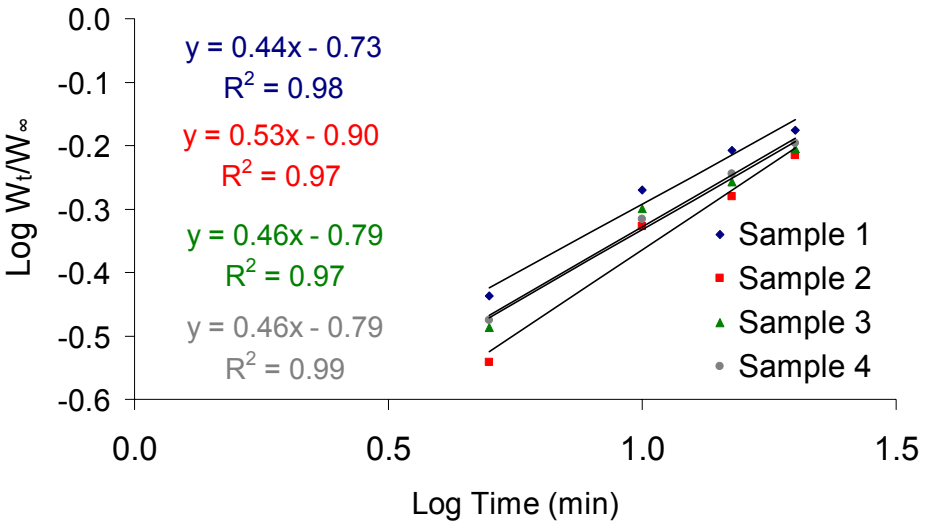

Figure 4-16. Representative plot used to calculate the time constant for diffusion kinetics. The log of fractional water uptake (Wt/W∞) is plotted against the log of time. The time exponent (n) for the welling kinetics is calculated from the slope of this plot according to Equation 4-4

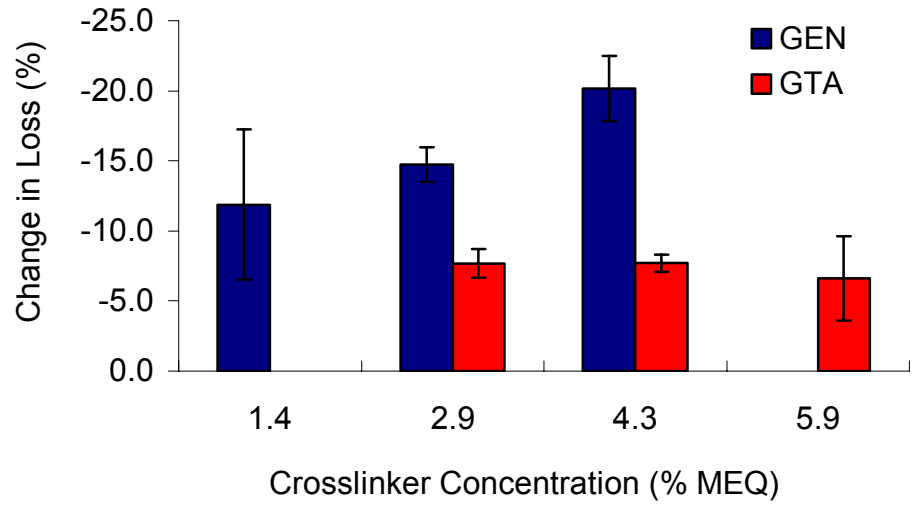

Figure 4-17. Mass loss of GEN and GTA crosslinked gelatin samples after swelling for 7 days in water. Samples were dried for 3 h at 50ºC.

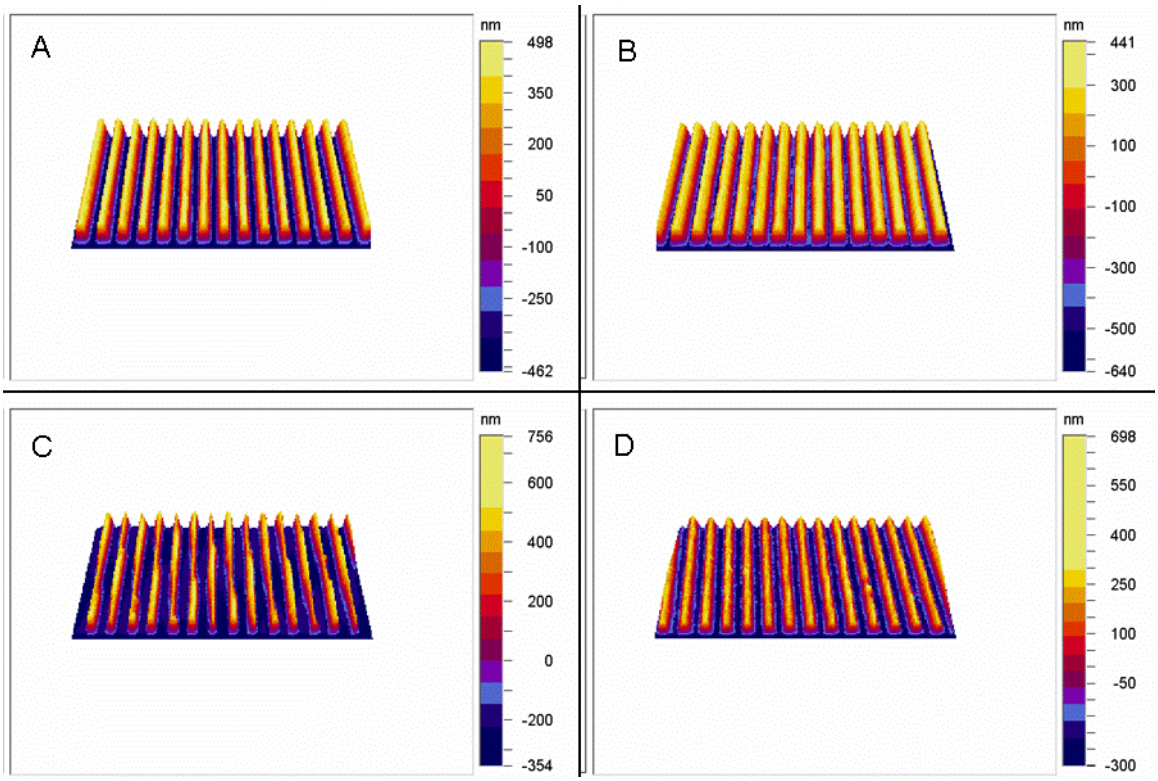

Figure 4-18. Profilometry images of channel topographies replicated in different materials. A) Silicon wafer. B) PDMSe mold. C) Dry gelatin. D) Rehydrated gelatin. Gelatin samples were crosslinked with 2.9% MEQ genipin. Images are of 48x76 µm2 sample areas.

Table 4-1. Diffusion Parameters Determined for GEN and GTA Crosslinked Gelatin

Crosslinker	Crosslinker Concentration (% MEQ)	Diffusion Coefficient, D ($\mu m^2/s$)	Time Exponent, n
GEN	1.4	13 ± 2	0.46 ± 0.08
	2.9	13 ± 1	0.39 ± 0.05
	4.3	13 ± 2	0.36 ± 0.03
GTA	2.9	15 ± 2	0.54 ± 0.06
	4.3	12 ± 2	0.49 ± 0.07
	5.9	14 ± 2	0.47 ± 0.04

Table 4-2. Feature Dimensions of Topographically Modified Substrates Measured by WLIP

Material	Ridge Width (μm)	Channel Width (μm)	Feature Depth (μm)
Silicone Wafer	2.3 ± 0.1	1.7 ± 0.1	0.90 ± 0.02
PDMSe	1.6 ± 0.1	2.4 ± 0.1	0.90 ± 0.01
Dehydrated Gelatin	2.7 ± 0.1	1.3 ± 0.1	0.77 ± 0.02
Rehydrated Gelatin	2.4 ± 0.1	1.6 ± 0.1	0.55 ± 0.01

CHAPTER 5
ENDOTHELIAL CELL GROWTH ON TOPOGRAPHICALLY PATTERNED SUBSTRATES

Introduction

Researchers have sought to improve the antithombogenic nature and hence the patency of artificial vascular grafts though the incorporation of endothelial cells onto the inner lumen of the graft surface [2, 3, 6-33]. They have shown that endothelial cells grow to confluence on a wide variety of substrates, but are removed when exposed to shear stresses equivalent to those present in natural human arteries. Attempts to improve endothelial cell adhesion have included surface modifications of the graft materials by coating with adhesion proteins such as albumin, extra cellular matrix, gelatin and fibronectin [15, 18, 28-30, 32, 33] as well as non-specific treatments such as carbon deposition and plasma discharge [33]. These methods have found some success at improving short term adhesion, but cellular retention is not maintained for longer exposures (>3 h). A more newly developed treatment has involved the use of a peptide sequence found in fibronectin. Covalent binding of synthetic versions of the arginine-glycine-aspartate (RGD) sequence has been shown to overcome late term removal of cells and to resist platelet adhesion and activation [13, 15, 32].

Another approach to improving endothelial resistance to shear looks at cell morphology in natural arteries. Endothelial cells located in vascular regions of relatively high shear stress tend to be elongated in the direction of flow and have actin filament bundles which terminate at focal adhesions that are aligned parallel to flow [35]. Alternatively, endothelial cells grown in static tend to be polygonal in morphology with only a small number of stress fibers confined to the cell periphery [36]. When statically cultured cells are exposed to shear, cytoskeletal and sometimes morphological changes

are induced. These changes are accompanied by a stiffening of the cell which is related to an increase in stress fiber density [37]. Depending upon the magnitude and duration of shear exposure, cells elongate and stress fibers align with the flow direction accompanied by the coalescence of focal contacts so that they are fewer in number but greater in size [36, 38]. In order for a cell grown in static culture to align itself in this manner, it must break many of the focal adhesions it created with the surface and form new ones. It is likely that during this transitional period cells are removed from a surface. If this is the case, then a method which would cause the cells to align prior to implantation would be advantageous.

It has long been known that cells respond to the shape of the substrate on which they grow. [41]. In the past several decades, literature on cellular responses to topography has expanded rapidly. Researchers have investigated numerous combinations of cell types and topographical geometries and dimensions as listed In Appendix A. Confining the discussion to only the area of endothelial cells, Barbucci and Magnani investigated the influence of the combination of topography and chemical patterning on cell behavior [31, 51]. They observed that endothelial cells increasingly align themselves to ridges as the topographical spacing is reduced from 100 to 10 μm. Similar results were found by Wilkerson during the study of endothelial cell growth on ridges ranging in spacing from 20 to 5 μm [52]. Additionally, Feinberg has shown that cells confluence is disrupted by topographies will profile heights greater than 1 μm and that focal adhesions form almost exclusively on fibronectin (FN) regions of FN-patterned polydimethylsiloxane elastomer (PDMSe) [54]. Additionally, he showed that the area of

individual focal adhesions does not vary with surface treatment and is approximately 2 μm^2.

This work proposes that microscale topographies can be used to orient the cytoskeletal components of endothelial cells. In the following studies, microscale channel and topographies were generated in PDMSe and gelatin. The height of the topographical features was maintained at ~1 μm so as not to disrupt endothelial cell spreading. Because this height was significantly shorter than for Sharklet AF™ (3 μm) which was introduced in Chapter 3, the new name of Sharklet CE™ was developed to indicate it is cell enhancing. The topographies of primary interest had lateral dimensions of ~3 μm so that focal adhesions could be supported. Additionally, the height of the primary topographical features was maintained at ~1 μm so as not to disrupt endothelial cell spreading. Porcine endothelial cells were cultured on the topographies and cell density, confluence, density and spreading were examined. Additionally the ability of topographies to align focal adhesions and nuclei was investigated

Materials and Methods

Engineered Topographies

Silicon wafer masters were prepared using standard photolithography techniques (processing performed by James Schumacher). Both channel and Sharklet CE™ patterns were included with feature heights of ~1 μm for most topographies. Negatives of these topographies were generated in the silicon wafers, so that positives (channels are defined by ridges protruding out of the surface) would be formed once a material is cast against them. For example, a channel in the wafer becomes a ridge in the replicating material. For convenience, the following naming scheme was developed by the Brennan group:

[depth]_[topography type]_[width]x[spacing]

All feature dimensions are given in micrometers. The depth was identified as '-' if the features were etched below the surrounding planar surface as in the case of the silicon wafer master and "+" if the features were raised above the surrounding material as in the initial replicating material (Fig. 5-1). The topography type was classified as either "CH" for channels or "SK" for Sharklet CE™. Although, the target lateral dimensions were 2x2 for most of the topographies in the following studies, the true dimensions for some of the topographies were closer to 3x1 (see Results section). For the purpose of naming topographies, the actual dimensions were used. As an example, +1_CH_1x3 refers to positive channel features that are 1 μm tall, 1 μm wide and 3 μm spaced. The names and descriptions of all topographies used are given in Table 5-1.

Two-dimensional representations were first created using AutoCAD® and then electronically transferred in chrome onto quartz optical photomasks using e-bream lithography. Clean silicon wafers were then coated with positive photoresist via spin coating. Two techniques for generating topography were then used: deep reactive ion etching (DRIE) and photoresist (PR) exposure. In the PR process, first the photoresist layer was exposed to UV light long enough to fully penetrate the photoresist. In areas of the mask where no chrome is present, the UV light is transmitted and chemically alters the photoresist to make it more soluble. Then wafers were exposed to a developer solution to remove all regions exposed to UV. In this manner, the pattern was reproduced in the photoresist.

In the DRIE process, wafers were then exposed to reactive ion etching so that the features are transferred into the underlying silicon. Etched wafers were cleaned via a piranha etch (50:1 of H_2SO_4 andH_2O_2) at 120°C for 10 minutes followed by subsequent

rinsing in acetone and ethanol prior to each replication with PDMSe. Clean wafers were treated with hexamethyldisilazane (HMDS) to prevent adhesion by generating unreactive methyl groups on the surface. The HMDS was applied by vapor deposition under 28 inHg (95 kPa) vacuum.

PDMSe Mold Preparation

Smooth and patterned PDMSe wells were formed using Dow Corning Corporation's Silastic T-2 as previously described in Chapter 4.

Preparation of Gelatin Films

Gelatin derived from bovine calf skin was supplied as a dry powder (Sigma). Genipin crosslinked (10 w/w%) gelatin films were prepared as previously described in Chapter 4. Briefly, the appropriate amount of genipin was dissolved in nanopure water and heated to 50°C. Then gelatin was added to create a 10 wt/v% aqueous solution. The mixture was then cast into the PDMSe mold (smooth or with topography) and allowed to react for 24 h at room temperature. In order to minimize the amount of residual unreacted GEN in the films, samples were immersed in nanopure water for 3 days at room temperature. The nanopure water was exchanged every 24 h.

Prior to cell seeding, all samples were sterilized in 70% ethanol and rinsed 3 times in phosphate buffered saline (PBS). They were then equilibrated in PBS at 37°C in an incubator for 4 h.

Preparation of PDMSe Films

PDMSe films were cast directly against silicon wafers. The base resin and curing agent were mixed (10:1 by weight), degassed and poured over top of the silicon wafer. Curing was carried out at room temperature for 24 h in a glass mold with spacers to generate ~1 mm thick films.

Characterization of Topographically Modified PDMSe and Gelatin Films

Dimensions of PDMSe and gelatin topographies were analyzed using scanning electron microscopy (SEM) and white light interference profilometry (WLIP).

Fibronectin Adsorption to Samples

Lyophilized bovine plasma fibronectin (Biomedical Technologies, Inc.) was dissolved (1 mg/mL) in 0.22 μm filtered water at 37°C for 45 minutes as described by the manufacturer. The solution was then diluted to 50 μg/mL in PBS. Samples were first sterilized in 70% ethanol for 30 minutes. Samples were rinsed 3 times with PBS and placed into the bottoms of the wells of culture plates. Gelatin samples were held in place with PDMSe washers placed above the samples. Enough fibronectin solution was added to just cover the surfaces (same volume for each sample) and allowed to react for 30 minutes (preliminary assay) or 1 h (all other studies) at room temperature. Samples were rinsed 3 times with PBS prior to cell seeding.

Cell Culture, Imaging and Processing

Porcine vascular endothelial cells (PVECs) were supplied by Dr. Edward Block (Veteran's Administration Hospital, Gainesville, FL) between passages 2 and 3. Cells were previously harvested from the pulmonary artery of 6 to 9 month old pigs [85, 91]. Cells were maintained in RPMI 1640 media supplemented with 10% fetal bovine serum and 1% antibiotic-antimycotic solution. They were incubated at 37°C and 5% CO_2. Unless used immediately, cells were passaged every 3-4 days when they were ~90% confluent. Cells were not typically used beyond passage 5. Prior to seeding cells on test surfaces, they were detached from the culture flasks by incubation with 1 mL of 0.05% trypsin for 10 minutes. Then 2 mL of media was added to stop the enzymatic reaction of

the trypsin. Cell concentration was measured using a hemocytometer and 1% crystal violet stain. Then the solution was diluted to achieve the desired seeding density.

Preliminary assay

The preliminary cell culture assay was carried out for 4 days using 12-well culture plates and two replicates of each sample described in Table 5-2. Cells (passage 6) were seeded at a density of 3.5×10^4 cells/mL with 1 mL being applied to each sample. Due to a lack of availability, cells could not be obtained between passages 2 and 5 at the time of the preliminary study. For the samples indicated, fibronectin treatment was carried out for 45 minutes.

On day 4, cells were washed twice with PBS and stained with 0.1% Mayer's hematoxylin (Sigma) for 8 minutes. They were then washed twice with water and stained with Eosin Y (Sigma) for approximately 30s. Cells were then washed twice with 95% ethanol. Cells were covered in PBS until imaged (less than 4 h). Preliminary cultures were imaged on a Zeiss Axioplan 2 microscope at 400X magnification. PDMSe and gelatin discs were removed from the well plates prior to imaging. A needle was used to minimize bending of the sample substrates. When necessary, the backside of the samples (the side without cells) was rinsed with isopropanol to remove residual H&E stains. Cell densities (cells/mm^2) were determined manually for each image.

Immunofluorescent assay

The immunofluorescence assay was carried out until confluence was reached on controls (4 days) using 6-well culture plates. Cells (passage 5) were seeded at a density of 1.0×10^4 cells/mL and 2.5 mL per well. Two replicates of each sample described in Table 5-3 were included. All samples were fibronectin treated for 1 h.

On day 4, cells were rinsed twice with PBS and then fixed in 4% formaldehyde for 5 minutes. Then permeability of the cell membranes was increased using 0.3% Triton X-100 (prepared with PBS) for 5 minutes. In order to stain for focal contact adhesions, cells were treated with mouse anti-vinculin primary antibody (1:400 in PBS) for 1 h at 37ºC. Cells were then rinsed 5 times in PBS and treated with goat anti-mouse conjugated to Alexa Fluor 488 (Molecular Probes, 1:400 in PBS)) for 1.5 h at 37ºC. After 5 rinses with PBS, cells were treated with 5 μm phalloidin-TRITC for 12 h at 37ºC in order to stain the actin cytoskeleton. Before placement in the incubator, 4 μL DAPI per mL PBS was added to stain the cell nuclei. Cells were then rinsed 5 times with PBS and covered in PBS until being imaged.

Fluorescent imaging was carried out using a Zeiss Axioplan 2 microscope with epifluorescence and digital capture system. Each sample was imaged at 2 locations each for 200X and 400X magnifications. At each location, 4 separate images were acquired. The first used white light and captured the topographical pattern. The remaining 3 used UV light though appropriate filters to capture the nuclei (DAPI), actin (TRITC) and focal adhesions (Alexa-Fluor 488) separately.

Images obtained for the fluorescent cell culture assay were processed using ImageJ software to create composite images as well as determine cell density, cell area and orientation of focal contact adhesions Cell density and orientation of nuclei were calculated from images of DAPI at 200X magnification. The image was first rotated so that the underlying topography (based on corresponding optical image) was oriented vertically. Then the image was converted to an 8-bit black and white image and ellipses were fitted to the cell nuclei using the “Analyze Particles” feature (Fig 5-2). ImageJ

generated a result file which includes a count of the ellipses, lengths of major and minor axes, and angle formed between major axis and horizontal reference line. Cell density was calculated by dividing the number of ellipses by the area of the field of view (0.095 mm^2). Elongation of nuclei was found by dividing the length of the major axis by the length of the minor axis. Orientation angles were found by subtracting the output angle by 90º, the angle formed between the topography and horizontal reference line. In this manner, orientation angles ranged from -90º to +90º. A negative sign in the orientation angle indicates that the nuclei are offset in the counterclockwise direction as opposed to the clockwise direction. The nuclear orientation within a given image was determined using Hermans orientation function. Hermans parameter is typically used to describe the degree of orientation of fibers within a composite. It is calculated from the following equation:

$$f = 2 < \cos^2 \theta > -1. \qquad (5\text{-}1)$$

In Equation 5-1, $<\cos^2 \theta>$ is the trigonometric average. Hermans parameter (f) ranges from -1 (perpendicular orientation to topography) to +1 (parallel orientation to topography). A value of zero indicates random orientation.

Cell area, elongation and orientation were determined from composite images of actin (Phalloidin-TRITC) and nuclei (DAPI) at 400X magnification (Fig 5-3A). Individual cells were traced in green (Fig 5-3B) and then these lines were separated from the image using the "RGB split" feature. The green image was converted to black and white and the interior of the cells filled with black (Fig 5-3C). The "Analyze Particles" feature was used and ellipses were fitted to the cells. ImageJ generated result files containing the area of each cell (based on number of pixels and not an elliptical fit) the

lengths of the major and minor axes, and the angles formed between the major axes and a horizontal reference line. Elongation and orientation of cells were calculated using the same methods as for nuclei.

Focal contact adhesions were analyzed from images of vinculin at 400X magnification (Fig. 5-4A). Images were converted to black and white (Fig. 5-4B) and then the "Analyze Particles" feature was used and ellipses were fitted to each focal adhesion (Fig. 5-4C). Due to inherent noise in the vinculin imaging, it was necessary to only include particles of the appropriate size (20 to 80 pixels) and shape (major axis at least 25% longer than minor axis). Hermans orientation of the focal adhesions is calculated using the same methods as for nuclei.

Cell culture assay 3

The third cell culture assay was carried out for 4 days using 6-well culture plates. Cells (passage 5) were seeded at a density of 1.0 x 104 cells/mL and 2.5 mL per well. Two replicates of each sample listed in Table 5-3 were included. All samples were fibronectin treated for 1 h.

On day 4, cells were rinsed twice with PBS and then fixed in 4% formaldehyde for 5 minutes. Cells were then rinsed thee times with PBS before being stained with 1% crystal violet for 2 minutes and rinsed with distilled water until water remained clear. Cells were immediately imaged using a Zeiss Axioplan 2 microscope at 50X and 200X. Five images per sample were taken at each magnification.

Cultures were imaged on a Zeiss Axioplan 2 microscope at 200X magnification. A manual count of cells in each image was made and densities (cells/mm^2) for each image reported. Images were then processed using ImageJ software to determine cell coverage area (i.e. confluence). The brightness and contrast were first adjusted and then the image

was converted to an 8-bit black and white image. Under "Set Measurements" only "area" and "area fraction" were selected and then the "Analyze Particles" tool was used to find the area fraction (ratio of black pixels to total pixels) for all cell groups. The average area per cell for each image was then calculated by multiplying the area fraction by the area of the field of view (0.38 mm^2) and then dividing by the number of cells.

Cell culture assay 4

The fourth cell culture assay was carried out until confluence was achieved on controls (6 days) using 6-well culture plates. Cells (passage 5) were seeded at a density of 1.0×10^4 cells/mL and 2.5 mL per well. Two replicates of each sample listed in Table 5-4 were included. All samples were fibronectin treated for 1 h.

On day 6, cells were rinsed twice with PBS and then fixed in 4% formaldehyde for 5 minutes. Cells were then rinsed thee times with PBS before being stained with 1% crystal violet for 2 minutes and rinsed with distilled water until water remained clear. Cells were immediately imaged using a Zeiss Axioplan 2 microscope at 200X and 400X. Thee images per sample were taken at each magnification.

Cultures were imaged on a Zeiss Axioplan 2 microscope at 200X and 400X magnifications. Cell confluence was determined from the 200X images using ImageJ software. The brightness and contrast were first adjusted and then the image was converted to an 8-bit black and white image. Under "Set Measurements" only "area" and "area fraction" were selected and then the "Analyze Particles" tool was used to find the area fraction (ratio of black pixels to total pixels) for all cell groups.

Cell density, area, elongation and orientation were determined from 400X images. A manual count of cells in each image was made and densities (cells/mm^2) for each image reported. Coverage area was determined as mentioned above and the average area

per cell for each image was then calculated by multiplying the area fraction by the area of the field of view (0.092 mm^2) and then dividing by the number of cells. In order to determine cell elongation and orientation, 12 cells from each image were traced and filled in black using ImageJ software. Cells were selected randomly with the only criteria being that their full outline could be observed. ImageJ software was then used to fit ellipses to the black-colored cells. Elongation was measured as the length of the major axis to minor axis of the cell. Orientations were measured according to Hermans orientation parameter as outlined in the immunofluorescence assay above.

Statistical Methods

All results are reported as mean values ±2 standard errors. One way analysis of variance (ANOVA, $\alpha = 0.05$) was performed for each dataset to determine if any statistical differences exist among the groups. Pair-wise t-tests ($\alpha = 0.05$) were performed as appropriate to determine which groups were statistically different.

Results

Characterization of Topographically Modified PDMSe and Gelatin

PDMSe samples replicated both the PR and DRIE wafers with high fidelity. Differences in fidelity between PR and DRIE replicates were evaluated using SEM images (Fig. 5-5). The DRIE process led to thinner ridges (wider channels) that more closely matched the target dimensions. WLIP was used to determine the dimensions of the features (Figs. 5-6 though 5-8). The profilometry data verified that the lateral dimensions of the topographies varied based on the wafer processing type, but there was not a significant difference in feature height (Table 5-5).

Preliminary Cell Culture Assay

As expected, PVECs did not grow on unmodified PDMSe substrates, but grew to confluence on fibronectin-adsorbed PDMSe (Fig. 5-9). Additionally, PVECS grew on all topographically modified PDMSe surfaces. Cells appeared slightly more elongated on the +1_SK_2x2 and +3_SK_2x2 topographies compared to smooth and channel-modified PDMSe. Cell densities did not vary significantly among smooth PDMSe and topographically modified PDMSe surfaces pretreated with fibronectin (Fig. 5-10).

Cells were not observed on gelatin surfaces. This may be due at least in part to the opacity of the gelatin samples. Because light could not be transmitted though the sample, the Zeiss Axioplan 2 microscope could not be used and instead samples were viewed using a Nikon scope lit though the objective. Even in this configuration, no cells were observed.

Immunofluorescent Cell Culture Assay

PVECs grew to confluence on smooth PS and all PDMSe substrates (Fig. 5-11). Cell densities were similar, ranging between 450 and 650 cells/mm^2 for all surfaces tested (Fig. 5-12). The +1_SK_3x1 (PR) patterned PDMSe yielded a significantly higher density of cells compared to all other surfaces except the +1_CH_2x2 (DRIE) patterned PDMSe. No significant differences existed among the remaining groups.

The average surface area of each cell showed greater variability than cell density (Fig. 5-13). Cells tended to be largest on the smooth PS and PDMSe surfaces with average areas of ~2000 and ~1800 μm^2 respectively. The +1_SK_3x1 (PR) pattern resulted in significantly smaller cells (~1300 μm^2) compared to all other surfaces. Additionally, cells on the +1_CH_1x3 (PR) pattern were significantly smaller (~1500 μm^2) than those on the PS controls. Cells on all surfaces tended to be elongated by ~80%

(Fig 5-14). No significant differences in elongation of cells were detected between smooth and topographically modified samples, although the orientation of the elongation appeared more random on the smooth surfaces.

The topographies were found to enhance alignment of cells, nuclei, and focal adhesions parallel to topographical features (Figs. 5-15, 5-16 and 5-17). Orientation of these elements were essentially random on smooth polystyrene and PDMSe surfaces, as the Hermans orientation parameters did not significantly differ from zero. Nuclei became partially aligned parallel to the topographical features as indicated by an increase in Hermans parameter. Although Hermans parameter for the +1_CH_1x3 (PR) topography was significantly different from zero, it was not significantly different from f for smooth PDMSe. The Sharklet CE™ topographies generated the highest degree of orientation (f~0.3) and orientation on these two surfaces were significantly different from smooth PS, smooth PDMSe and the +1_CH_1x3 (PR) topography.

Alignment of cells followed the same trend as the orientation of nuclei. All four topographies significantly enhanced orientation relative to smooth PS and PDMSe. The greatest degree of cell orientation was observed on the +1_SK_2x2 (DRIE) topography which yielded a Hermans orientation of ~0.45. Despite a trend for the Sharklet CE™ topographies to increase orientation of cells relative to channel topographies, no significant differences were observed.

Analysis of focal contact adhesions indicated that all surfaces promote alignment with the long axis of the underlying topography. Histograms of focal adhesion angles on PS and smooth PDMSe surfaces indicated an even distribution across all angles, whereas histograms for topographically modified PDMSe surfaces indicated a peak at or near the

topography angle (Fig. 5-18). Orientation was significantly enhanced on all four topographies relative to smooth PS and PDMSe surfaces. The greatest degree of orientation was observed on the two Sharklet CE™ topographies. Hermans orientation parameters for these two were ~0.44. Although orientations on channels topographies were not significantly different from that of the Sharklet CE™ topographies, Hermans parameter tended to be lower at a value of ~0.31 for each. This is consistent with the trends observed for cell bodies and nuclei.

Cell Culture Assay 3

Cells did not grow to confluence during the four culture days of assay 3 (Fig. 5-19) in which fibronectin treatment was increased to 1 hour from 30 minutes in the preliminary assay. Cell densities were highest on the two Sharklet CE™ surfaces and lowest on the two controls (PS and smooth PDMSe). All of the topographically modified PDMSe surfaces induced significantly greater cell densities than the smooth PDMSe control (Fig. 5-20). Additionally, all topographies with the exception of the +1_CH_1x3 (PR) pattern yielded a greater density of cells than on the PS control. The +1_CH_2x2 (DRIE) pattern provided the greatest density of cells, significantly greater than on all other surfaces except the +1_SK_3x1 (PR) pattern. Cells were significantly more dense on the +1_SK_3x1 (PR) pattern than the remaining surfaces except +1_CH_2x2 (DRIE) pattern.

Although the densities of cells on the Sharklet CE™ topographies were greatest, their degree of confluence did not vary significantly from the PS and smooth PDMSe controls (Fig. 5-21). Additionally, these did not vary significantly with the confluence on

the +1_CH_2x2 (DRIE) surface. The +1_CH_1x3 (PR) pattern, however, resulted in significantly less surface coverage than all other surface types.

Cells tended to spread less (smaller area) on the topographically modified surfaces than on the smooth PS and PDMSe controls (Fig. 5-22). The +1_CH_1x3 (PR) pattern did not vary significantly from the PS control, however. Cell areas did not vary significantly among the four different patterns, although the two Sharklet CE™ topographies had the lowest mean call area values.

Cell Culture Assay 4

Cells proliferated and were nearly confluent on all surfaces (Fig. 5-23). Cells on the smooth polystyrene and PDMSe controls varied in shape and had no apparent long range orientation. Most cells were more elongated than typical endothelial cells, and their appearance may be evidence of a mixed cell population. It is possible that either fibroblast or smooth muscle cells contaminated the primary culture.

In contrast to the cells on the smooth controls, cells appeared to orient with the long axis of features for all topographies studied. The topographies increased cell density relative to the smooth polystyrene and PDMSe controls (Fig. 5-24). This affect was greatest on the -3_CH_5x5 (DRIE) surface and became less apparent as the spacing of the channels increased to 10 and 20 μm. There was no significant difference in cell density among the two Sharklet CE™ topographies and these led to 55 and 22% increased in cell density compared to the smooth polystyrene and PDMSe controls respectively.

Quantitative analysis of the images indicated that the cells were most confluent on the +1_CH_2x2 (DRIE) topography (Fig. 5-25). Confluence was not statistically different on this surface compared to smooth polystyrene, smooth PDMSe, +1_CH_2x2

(DRIE) and -3_CH_5x20 (DRIE). Between 95 and 97% of these surfaces were covered with cells. Increasing the depth of the Sharklet CE™ topography led to a small but significant reduction in confluence as the surface coverage dropped from 97 to 93%. The -3_CH_5x5 (DRIE) topography resulted in the most disrupted confluence with only 89% of the surface are covered.

As was observed in the earlier assays, the topographies tended to reduce the average area occupied per cell to a value closer to that observed *in vivo* (Fig. 5-26). The largest cells (~1000 μm^2) were observed on tissue culture polystyrene and the smallest cells (~500 μm^2) were grown on the -3_CH_5x20 (DRIE) topography. Increasing the spacing between 5 μm wide channels to 20 μm led the cell area to approach that for smooth PDMSe (~800 μm^2). The areas of cells on +1_CH_2x2 (DRIE), +1_SK_2x2 (DRIE), and +3_SK_2x2 (DRIE) were similar at ~600 μm^2.

Cells elongated and oriented with features for all topographies studied. The affect of topography was more significant in this assay than any of the previous. The possibility of a mixed cell population might account for the difference among the assays. Cell elongation was similar on the +1_CH_2x2 (DRIE), +1_SK_2x2 (DRIE), +3_SK_2x2 (DRIE) and -3_CH_5x5 (DRIE) topographies which had mean values ranging from 3.6 to 4.0 (Fig. 5-27). For the 5 μm wide channels, elongation decreased with increased spacing between channels. Cell elongation on smooth polystyrene and PDMSe controls were not significantly different and were 1.7 and 1.8, respectively.

Hermans orientation parameter ranged from 0.94 to 0.98 for cells on all topographies with the +1_CH_2x2 (DRIE) topography resulting in the largest mean value (Fig. 5-28). It is unclear what caused the dramatic results. An older supply of fibronectin

was used in this study, but the increased alignment may have more to do with the biological variability in the cell source. Hermans orientation parameter for the smooth controls was not significantly different from zero, indicating random alignment of cells.

Discussion

Endothelial cells are not able to thive on the GEN crosslinked gelatin samples. This is most likely due to cytotoxic effects of residual unreacted GEN. This might be overcome with a more robust wash process, possibly involving longer leach times and immersion in PBS at 37ºC to more closely simulate the cell culture conditions.

When combined with fibronectin treated PDMSe, all four topographies with 2 μm lateral dimensions and 1 μm heights support endothelial cell growth. The subtle differences in topography generated by the photoresist and deep reactive ion etch processes did not result in significant differences in cellular response. The only exception was a slight increase in cell density and decrease in average cell area observed for the +1_SK_3x1 (PR) topography relative to its DRIE counterpart during the immunofluorescence assay. This difference was not observed in either the preliminary assay or assay 3, suggesting it may have been an outlying occurrence.

The microscale topographies tend to increase endothelial cell density relative to smooth FN-treated PDMSe, although the differences were not always significant for all assays. Additionally, cells on these topographies tend to spread across a smaller area and more closely approach the size observed in porcine arteries. Cell spreading, nuclei and focal adhesions are found to orient with the underlying topographies. In comparison to the channel topography of the same dimensions, the Sharklet CE™ topography tends to increase endothelial cell density and orientation of cytoskeletal components.

An increase in height of the Sharklet CE™ topography from 1 to 3 μm results in a slight (~3%) but significant decrease in the confluence of endothelial cells. Cell density and orientation are not significantly affected by the change in height. Cellular elongation and density decreased significantly as spacing increased from 5 to 20 μm on 3 μm deep channels, This is consistent with results observed by Wilkerson et al [52, 62]. Although cellular orientation on this topography is similar to that on +1_CH_2x2 (DRIE) and +1_SK_2x2 (DRIE) topographies, cell confluence was decreased significantly (~6%) indicating it is not a good candidate for cell seeding.

It is important to note that all of the PDMSe topographies were treated with fibronectin prior to cell culture. It is unclear what if any affect the protein adsorption had on the shape of the topography. It is conceivable that the protein may have filled in the topography to some degree so that the cells were presented with a somewhat smoother surface than what is indicated by the reported feature dimensions. If this work is carried forward in the future, the fibronectin adsorption to the topographies should be characterized. This might be accomplished with the use of immunofluorescently labeled fibronectin. A confocal microscope could be used to analyze the dimensions of the hydrated, labeled protein layer. Alternatively, the samples could be freeze dried after fluorescent labeling to lock in the structure. Then a microtome could be used to section the samples so that the Zeiss microscope with epifluorescence could be used to determine the thickness of the fibronectin layer in relation to the underlying topography.

Conclusion

Fibronectin treated PDMSe is a better substrate for culturing endothelial cells than fibronectin treated genipin crosslinked gelatin. In the PDMSe substrate, the +1_CH_2x2 (DRIE) and +1_SK_2x2 (DRIE) topographies are effective at orienting cytoskeletal

components while maintaining cellular confluence. These topographies will be evaluated for their ability to improve endothelial cell retention to shear in Chapter 6.

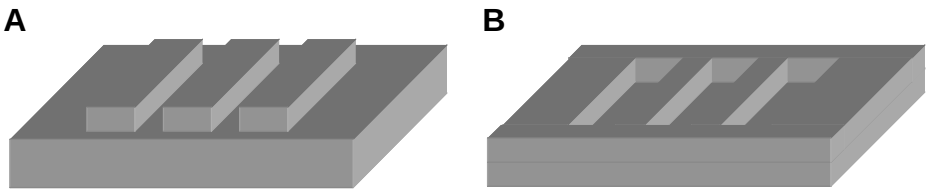

Figure 5-1. Example of convention used for naming topographies. A) Positive (+) features are raised above the plane of the surrounding material and B) negative (-) features are formed below the plane of the surrounding material.

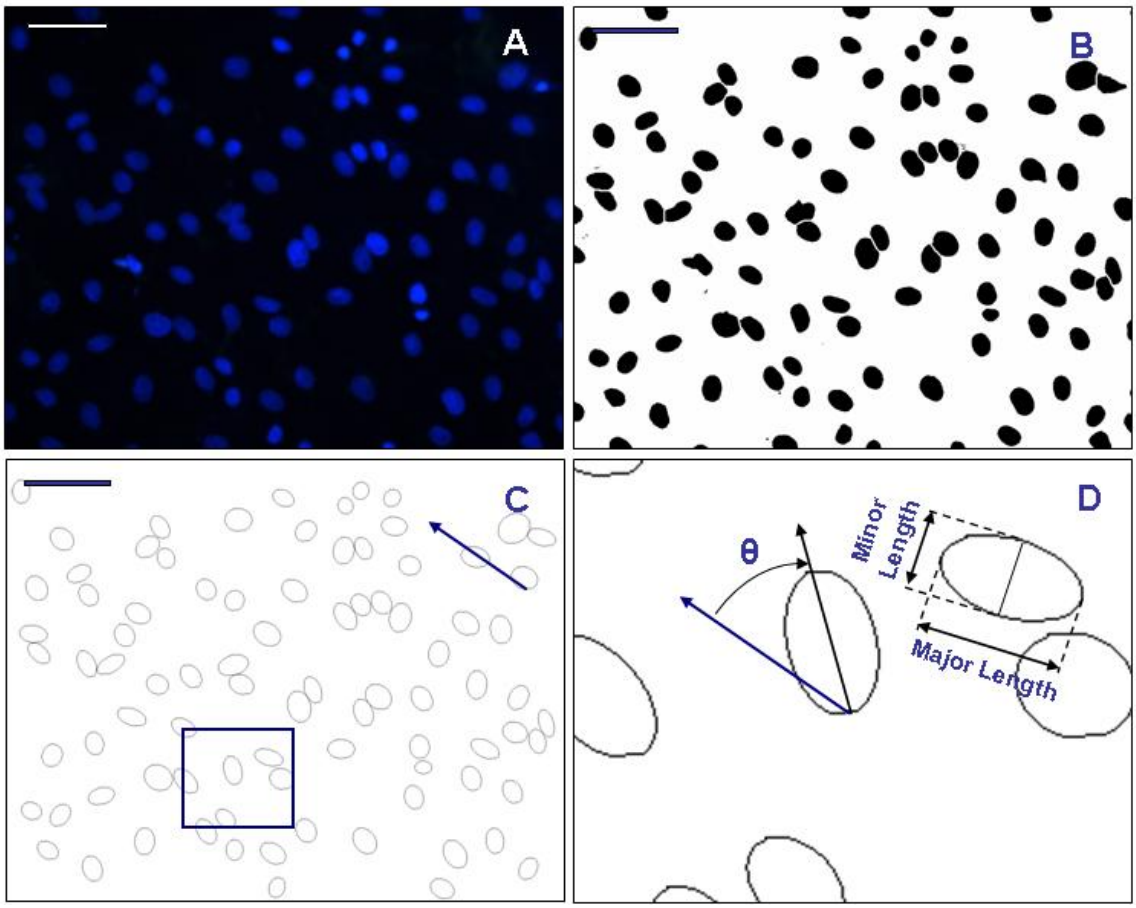

Figure 5-2. Processing of DAPI images to measure cell density and nuclear orientation. A) Image of nuclei on +1_SK_2x2 (DRIE) at 200X. B) Conversion to black and white. C) Ellipses fitted to nuclei and counted. D) Magnification of ellipses to demonstrate measurement of orientation angle and elongation. Blue arrows indicate topography direction. Scale bars represent 50 µm.

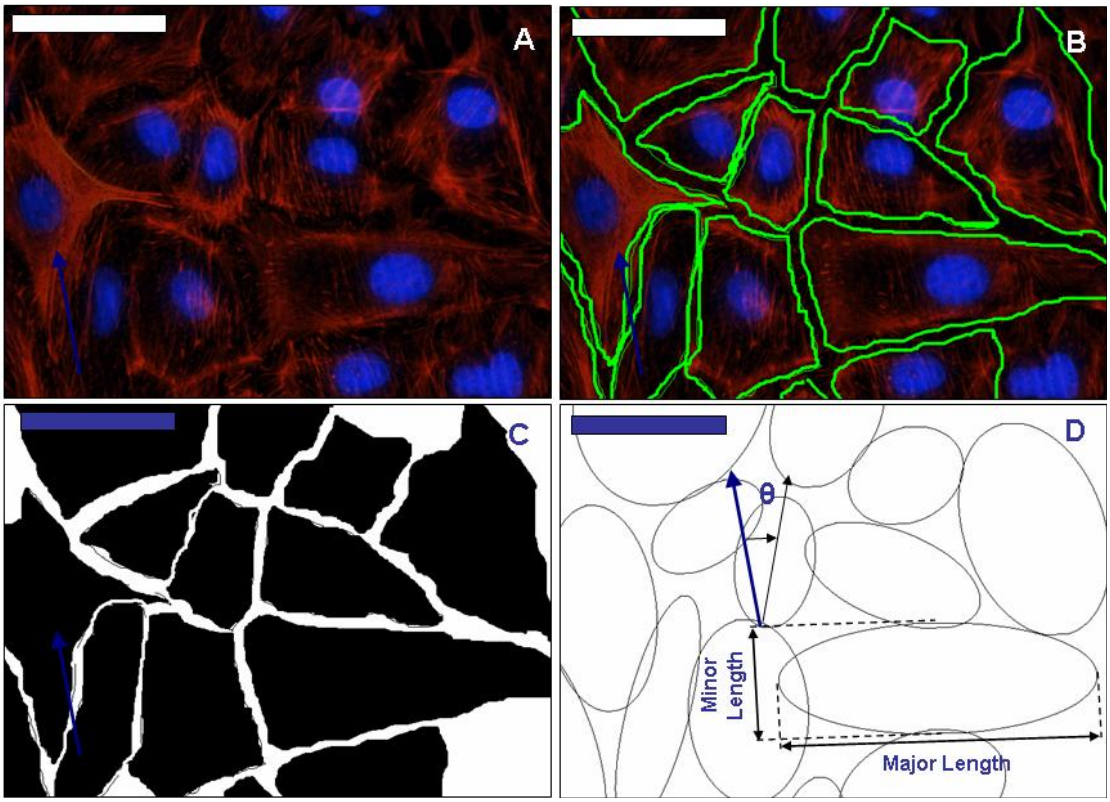

Figure 5-3. Processing of images to measure cell area, elongation and orientation. A) Portion of overlaid mage of nuclei (DAPI) and actin (phalloidin-TRITC for +1_CH_2x2 (DRIE) at 400X. B) Cells outlined in green. C) Cells filled with black for area calculation. D) Ellipses fitted to cells for measurement of orientation angle and elongation. Blue arrows indicate topography direction. Scale bars represent 25 μm.

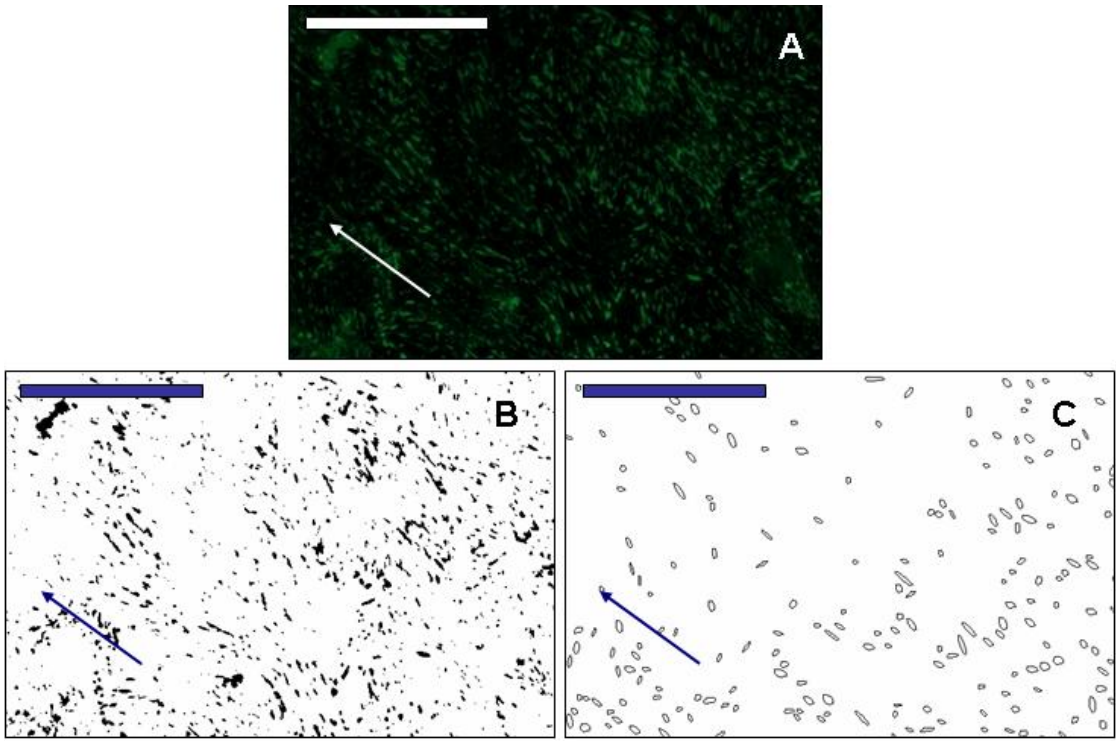

Figure 5-4. Processing of Alexa Fuor 488 images to measure alignment of focal adhesions. A) Image of focal adhesion (400X). B) Image converted to black and white. C) Image of ellipses fitted to adhesions and measured for alignment. Scale bars represent 25 μm.

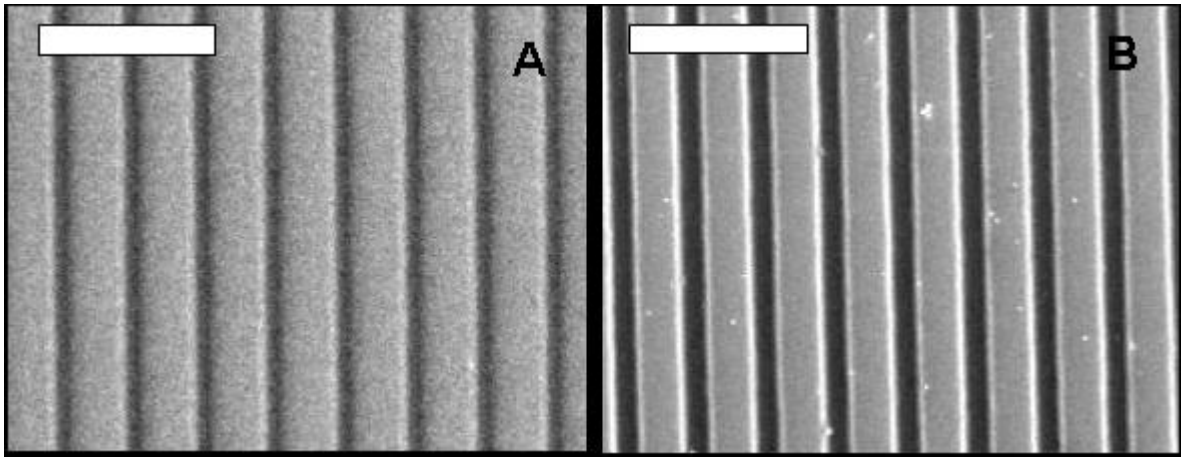

Figure 5-5. SEM images of PDMSe replicates of silicon wafers patterned by different processing methods. A) Photoresist. B) Deep reactive ion etching. Target dimensions of the channel topographies were 2 μm wide, 2 μm spaced and 1 μm depth. Scale bars represent 10 μm.

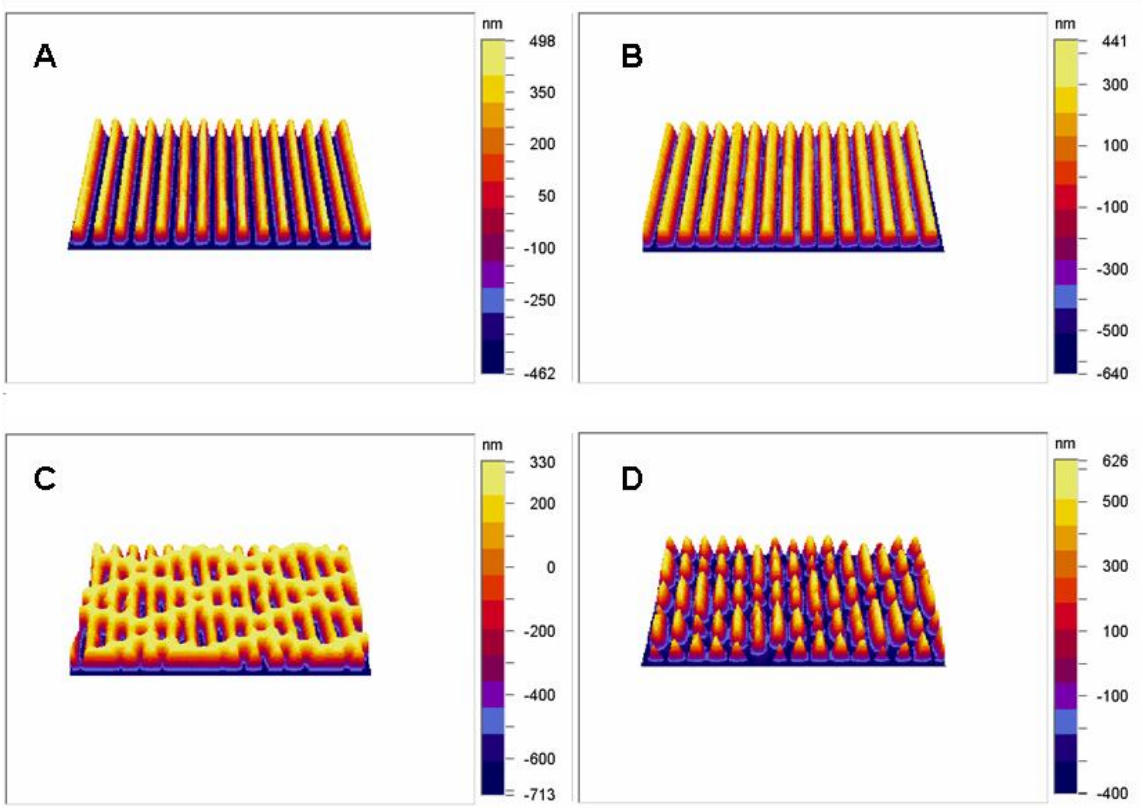

Figure 5-6. WLIP images of topographies formed by the DRIE process (100X). A)-1_CH_2x2 silicon wafer. B) +1_CH_2x2 PDMSe replicate of (A). C) -1_SK_2x2 silicon wafer. D) +1_SK_2x2 PDMSe replicate of (C). Images are of 48x76 μm^2 sample areas.

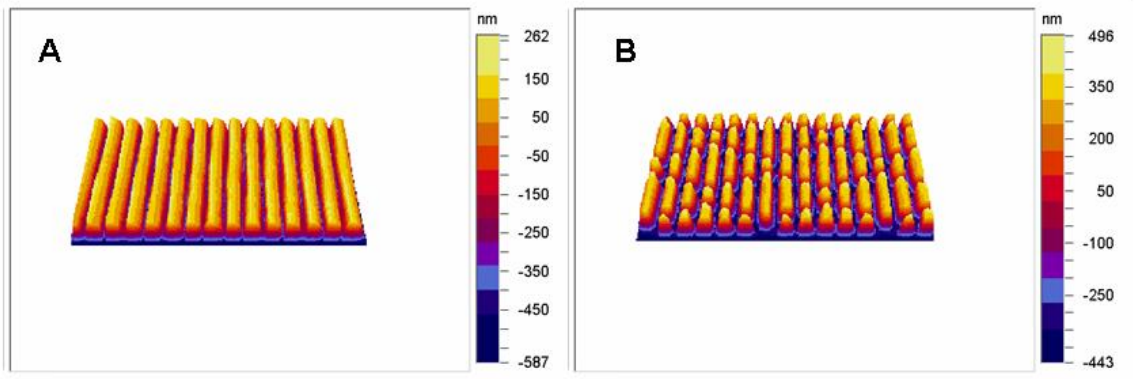

Figure 5-7. WLIP images of PDMSe topographies formed by the photoresist process (100X). A) +1_CH_1x3 PR. B) +1_SK_3x1 PR. Images were taken at 100X magnification and are of 48x76 µm sample areas.

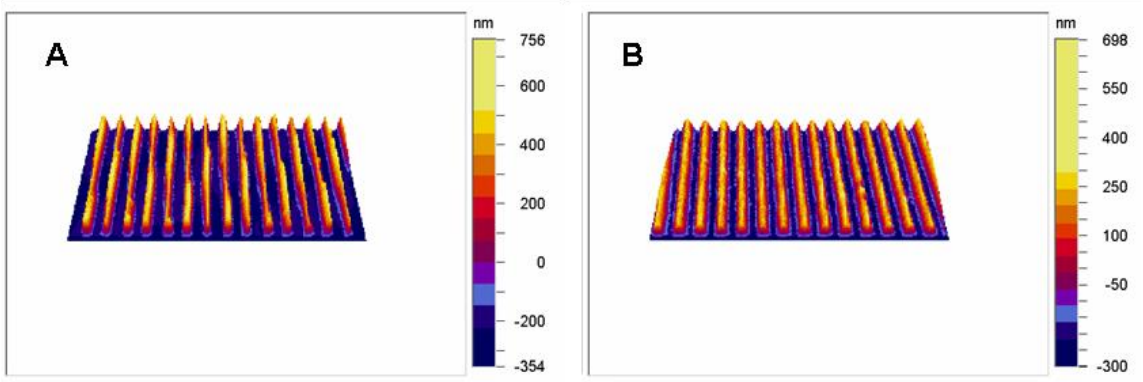

Figure 5-8. WLIP images of gelatin channels (100X). Gelatin topographies were replicated from the -1CH3x1 DRIE silicon wafer via a PDMSe intermediate. A) Dehydrated gelatin. B) Hydrated gelatin. Images are of 48x76 μm^2 sample areas.

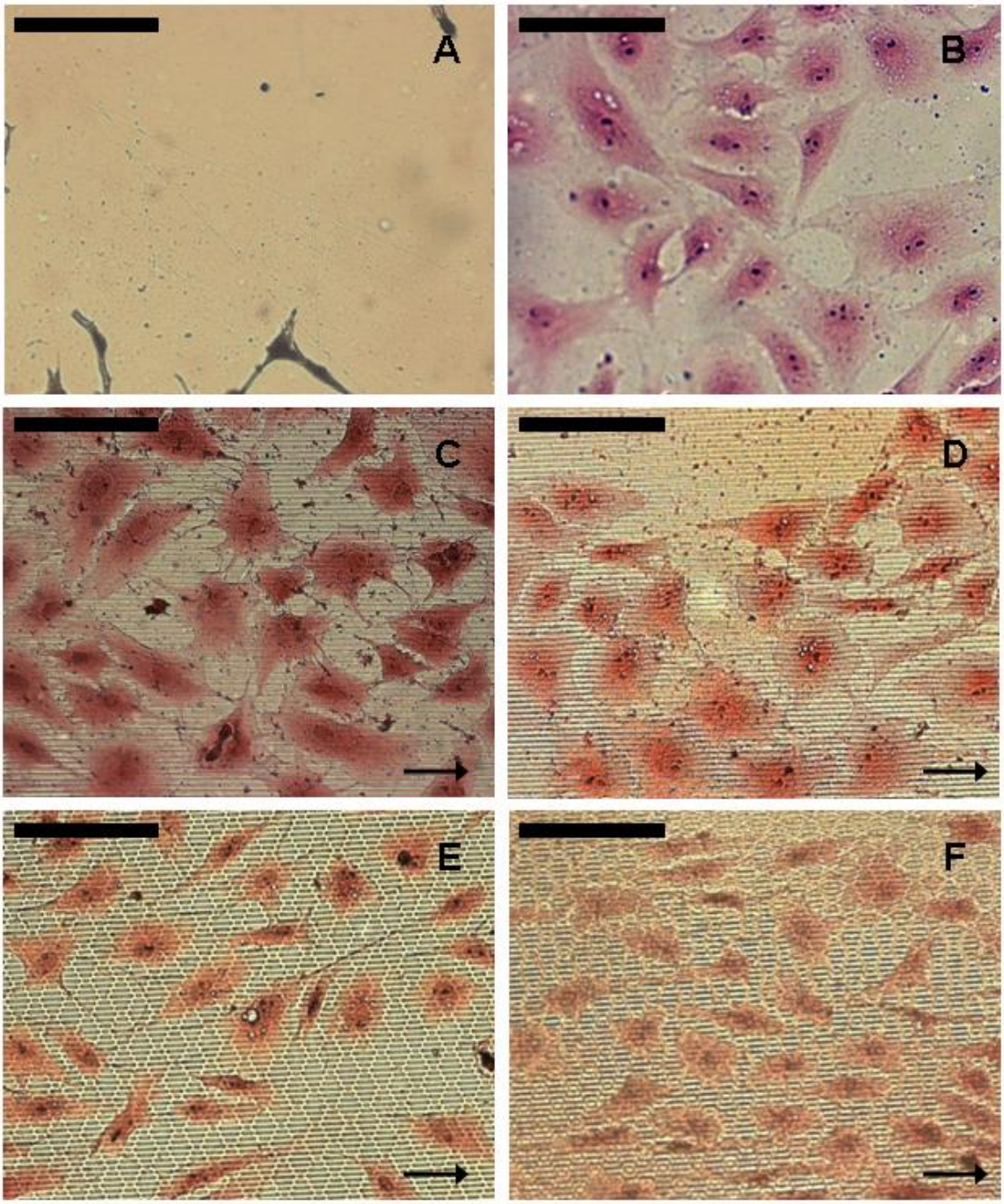

Figure 5-9. PVECs grown on PDMSe topographies in the preliminary assay. A) Smooth without fibronectin. B) Smooth. C) +1_CH_1x3 (PR). D) +1_CH_2x2 (DRIE). E) +1_SK_3x1 (PR). F) +1_SK_2x2 (DRIE). Fibronectin was adsorbed to all surfaces unless otherwise indicated. Topography directions are indicated by arrows. Images were captured at 400X. Scale bars represent 25 μm.

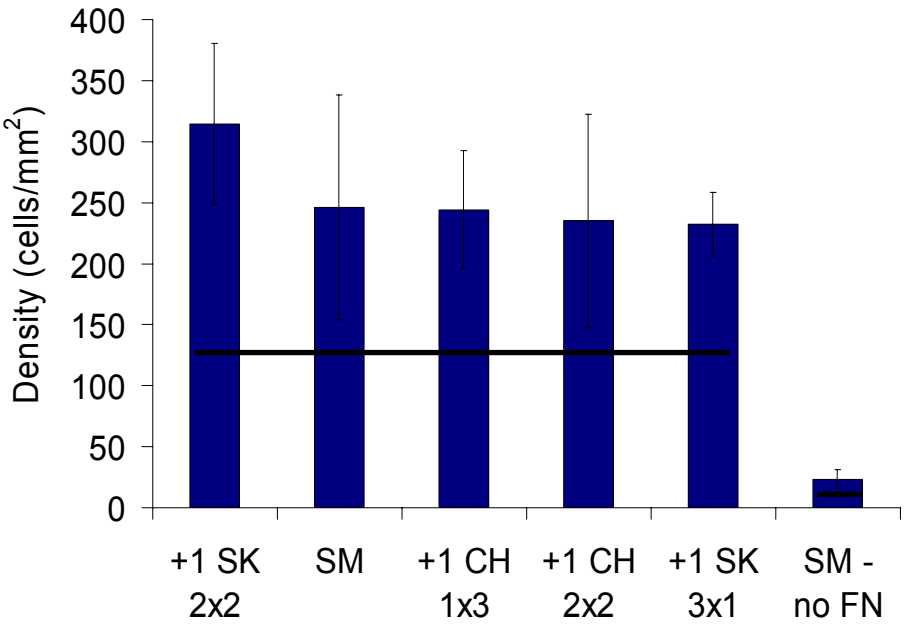

Figure 5-10. Density of PVECs on PDMSe topographies in the preliminary assay. All samples were pretreated with fibronectin (FN) unless stated otherwise. Data was obtained though manual count of images at 400X magnification. Groups of statistically indistinct means are indicated by tie bars (t-test, $\alpha = 0.05$).

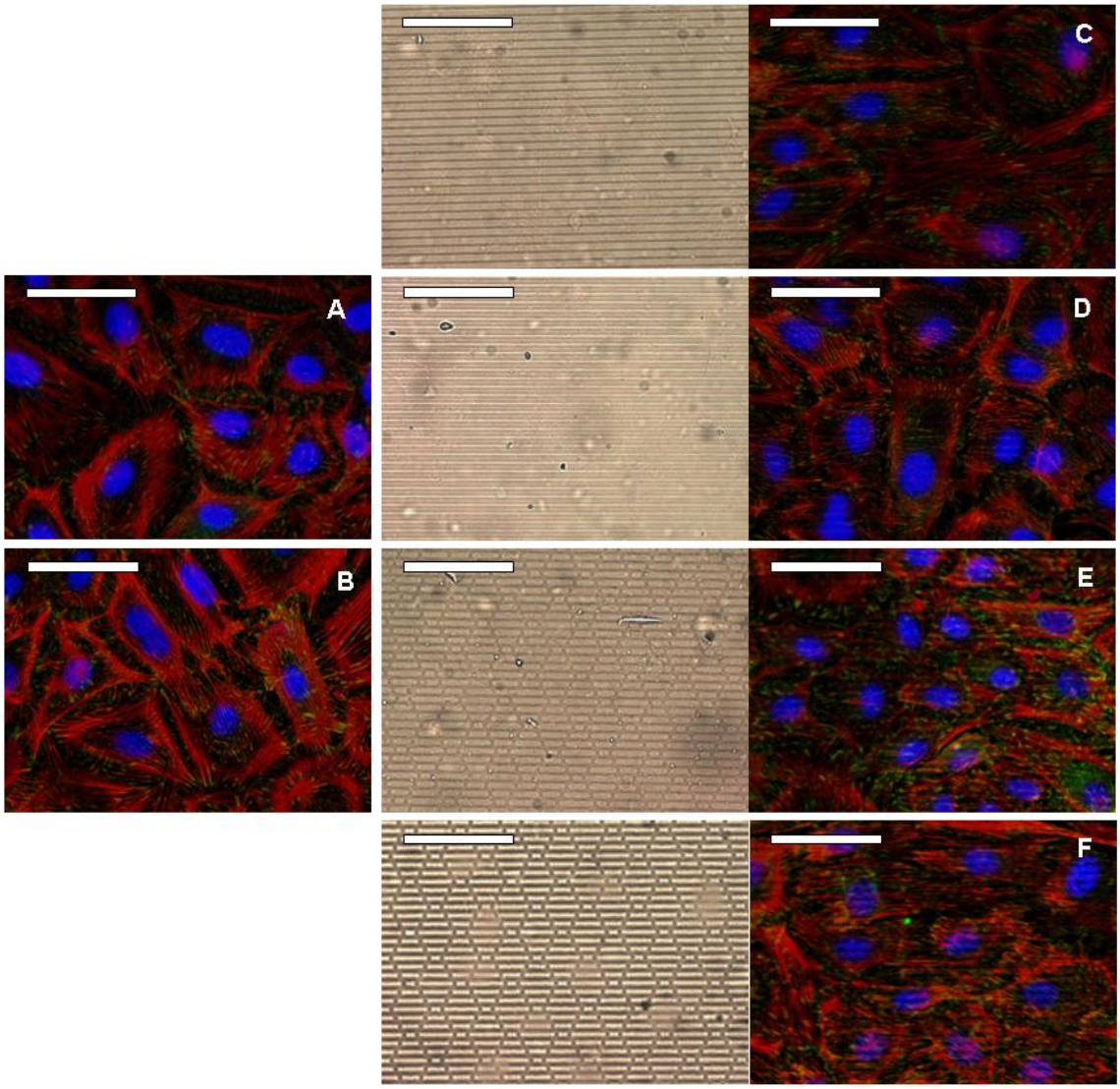

. Figure 5-11. Fluorescent images of PVECs grown on A) TCP, B) smooth PDMSe and C-F) topographically modified PDMSe. All PDMSe samples were pretreated with adsorbed fibronectin. The light microscope views at the left of images C though F show the underlying topography to the fluorescently labeled PVECs to the right of the images. Images were captured at 400X magnification and scale bars represent 25 μm.

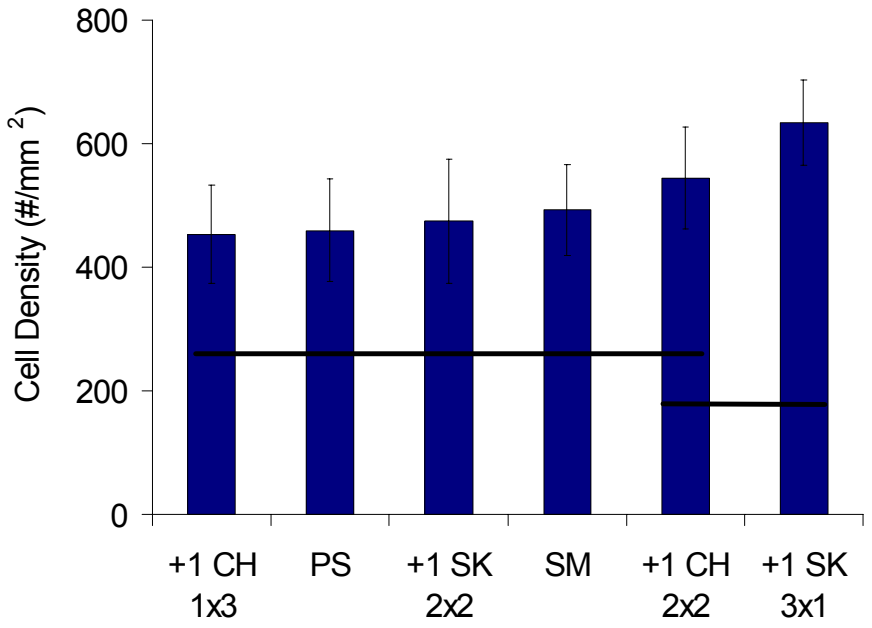

Figure 5-12. Density of PVECs on topographies in the fluorescent assay. Cells were grown on fibronectin-adsorbed PDMSe surfaces and PS. Data was obtained though processing of fluorescent DAPI images at 200X magnification. Tie bars connect groups with means that are not statistically different (t-test, $\alpha = 0.05$).

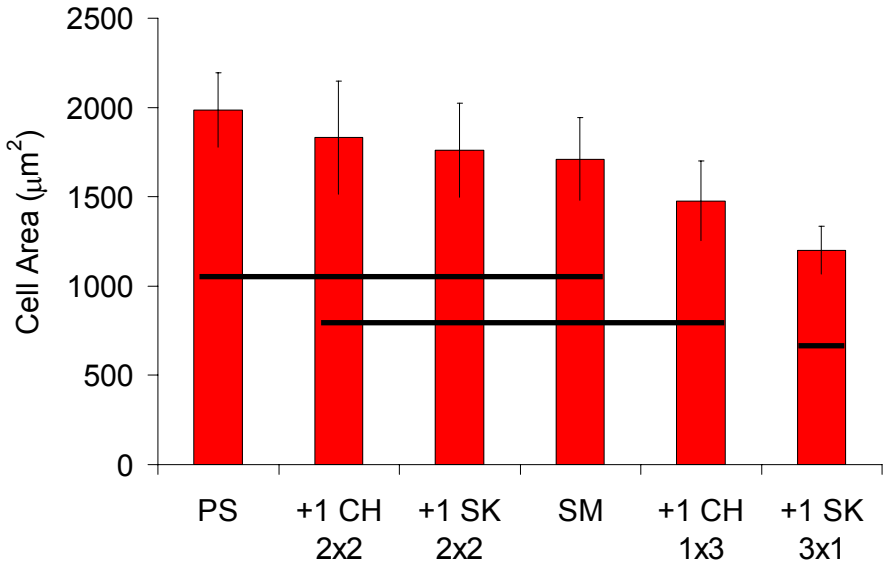

Figure 5-13. Mean cell area for PVECs on topographies in the fluorescent assay. Cells were grown on fibronectin-adsorbed PDMSe surfaces and TCP. Values were generated though the processing of overlaid images of cell nuclei (DAPI) and actin (phalloidin-TRITC). Tie bars connect groups with means that are not statistically different (t-test, $\alpha = 0.05$).

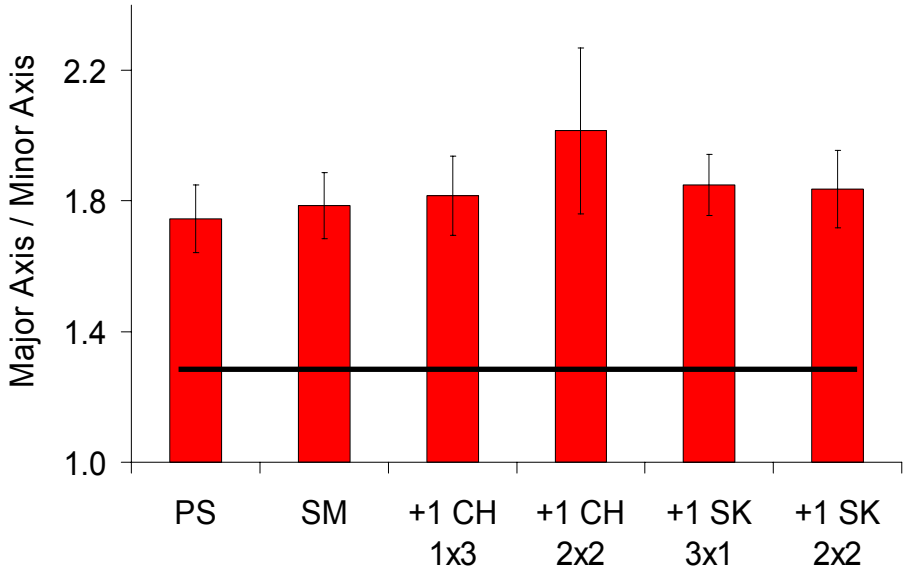

Figure 5-14. PVEC elongation on topographies in the fluorescent assay. Cells were grown on fibronectin-adsorbed PDMSe surfaces and TCP. Tie bar connects group with means that are not statistically different ($\alpha = 0.05$).

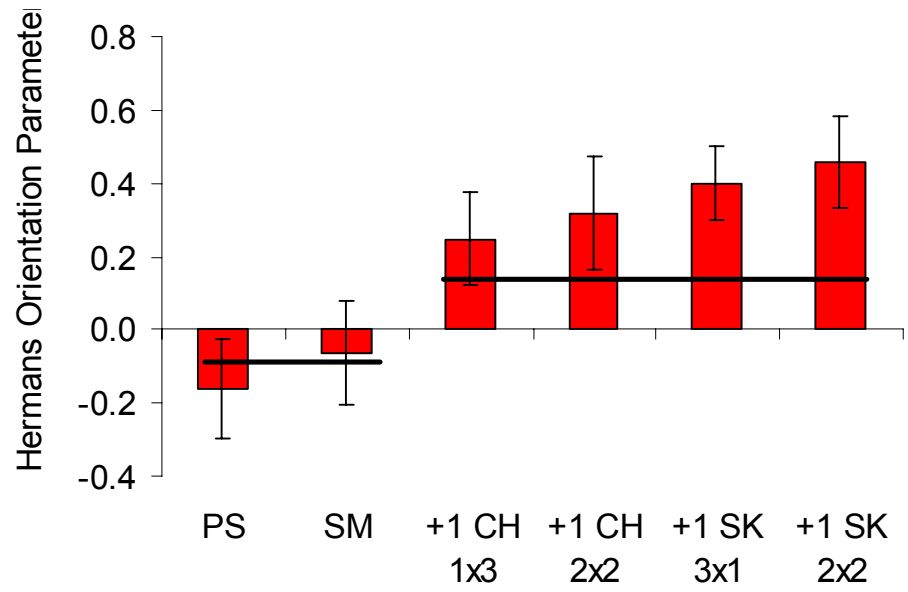

Figure 5-15. PVEC orientation on topographies in the fluorescent assay. Cells were grown on fibronectin-adsorbed PDMSe surfaces and PS. Smooth PS and PDMSe do not significantly alter orientation away from random (Parameter=0). All topographies significantly increase orientation. Tie bars connect groups with means that are not statistically different (t-test, $\alpha = 0.05$)

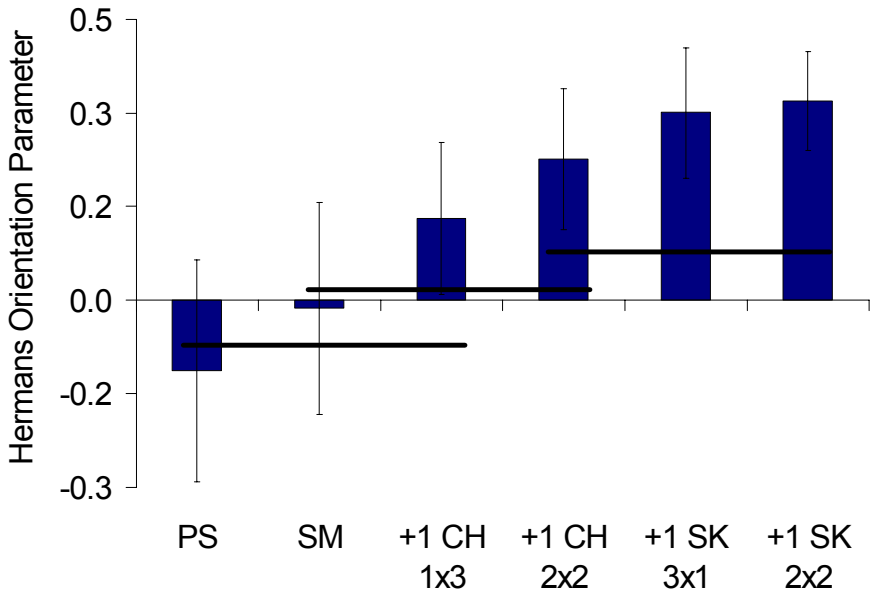

Figure 5-16. Orientation of PVEC nuclei on topographies in the fluorescent assay. Cells were grown on fibronectin-adsorbed PDMSe surfaces and PS. Smooth PS and PDMSe do not significantly alter orientation away from random (Orientation Parameter=0). All topographies significantly increase orientation relative to smooth PS. Tie bars connect groups with means that are not statistically different (t-test, $\alpha = 0.05$).

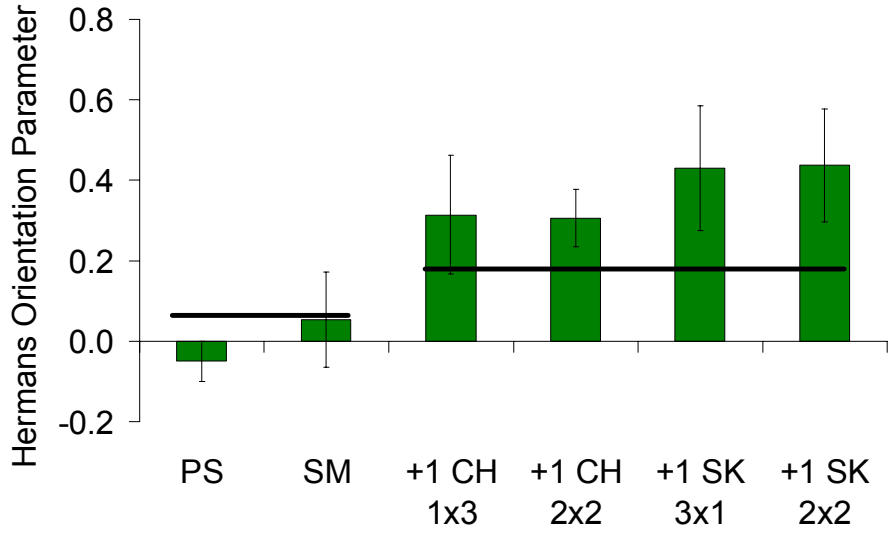

Figure 5-17. PVEC focal adhesion orientation on topographies in the fluorescent assay. Cells were grown on fibronectin-adsorbed PDMSe surfaces as well as PS. Error bars indicate ±2 standard errors. Orientation on smooth PS and PDMSe surfaces are not significantly different from random (parameter=0). All topographies significantly increase orientation. Tie bars connect groups with means that are not statistically different (t-test, $\alpha = 0.05$)

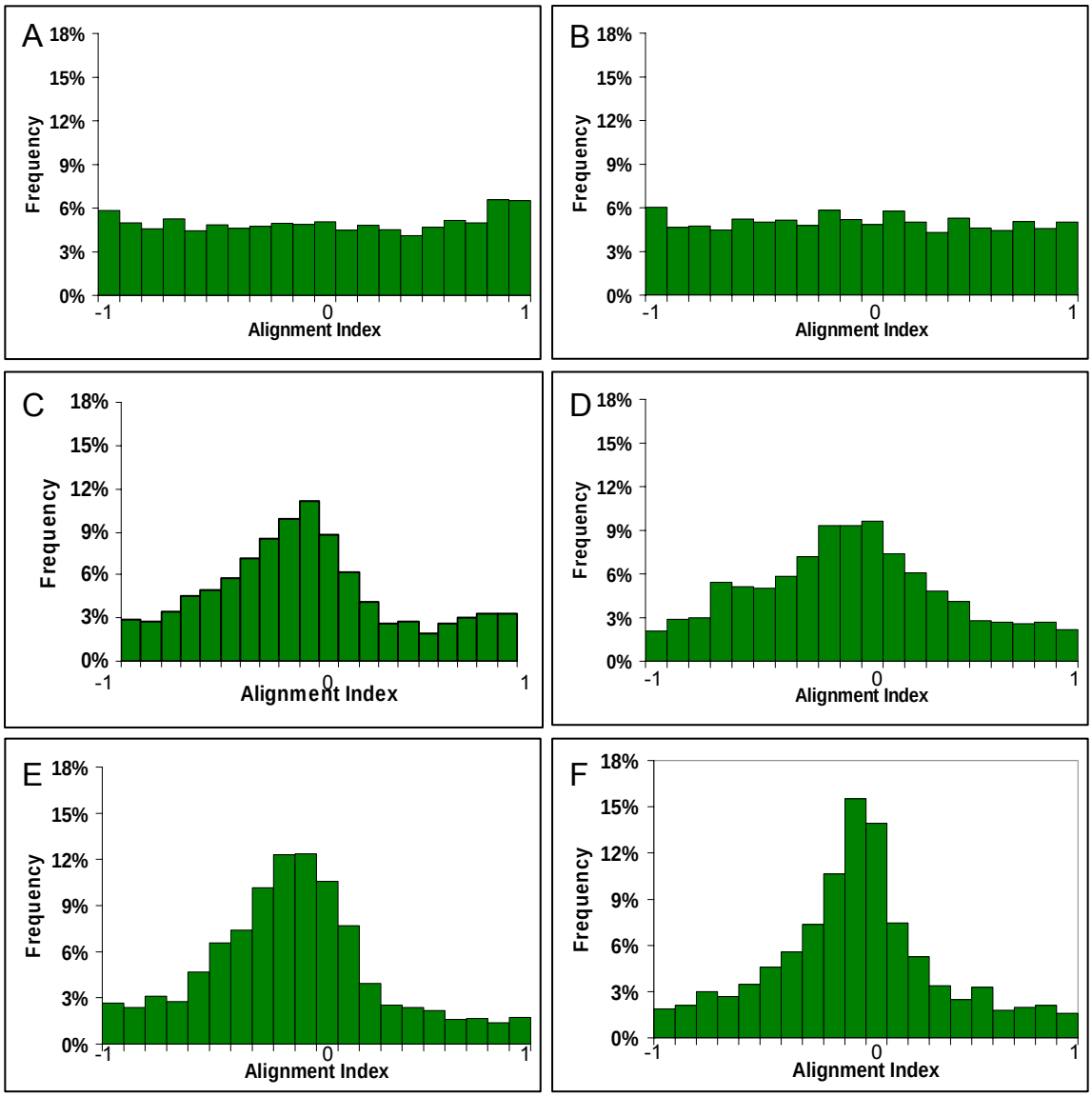

Figure 5-18. Histograms of alignment indices for focal adhesions on A) TCP, B) smooth PDMSe, C) +1_CH_1x3 (PR) PDMSe, D) +1_CH_2x2 (DRIE) PDMSe, E) +1_SK_3x1 (PR) PDMSe, and F) +1_SK_2x2 (DRIE) PDMSe. An alignment index of zero indicated the adhesion is perfectly aligned with the topography, while indices of -1 and 1 indicate adhesions are off-angle from topography by 90 º clockwise and 90º counter-clockwise respectively.

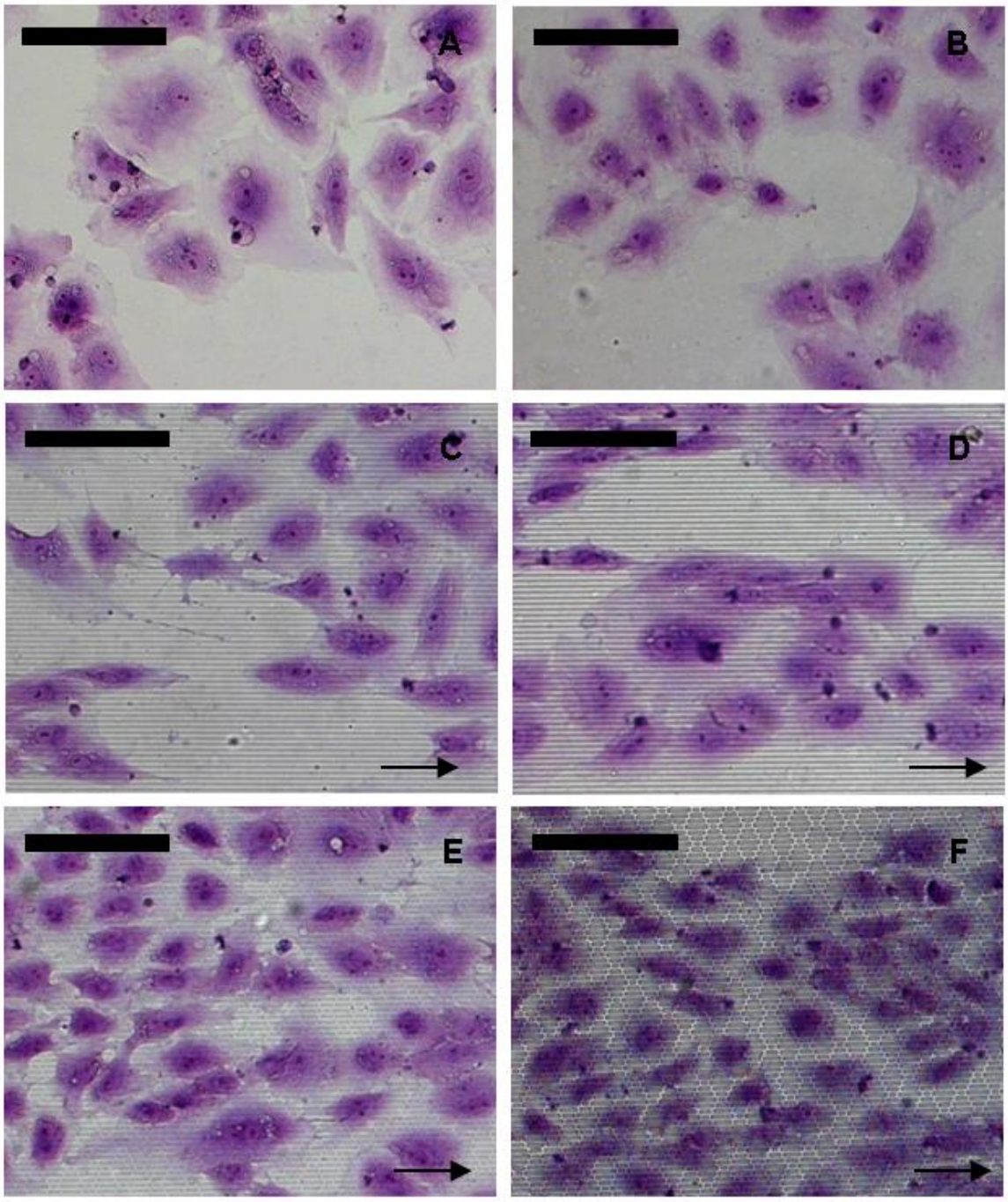

Figure 5-19. Light microscope images of PVECs grown on topographies for Assay 3. A) PS, B) smooth PDMSe, C) +1_CH_1x3 (PR) PDMSe, D) +1_CH_2x2 (DRIE) PDMSe, E) +1_SK_3x1 (PR) PDMSe, and F) +1_SK_2x2 (DRIE) PDMSe. All surfaces were pretreated with 50 µg/mL fibronectin for 1 h. Topographies are oriented from left to right as indicated by arrows. Scale bars represent 50 µm.

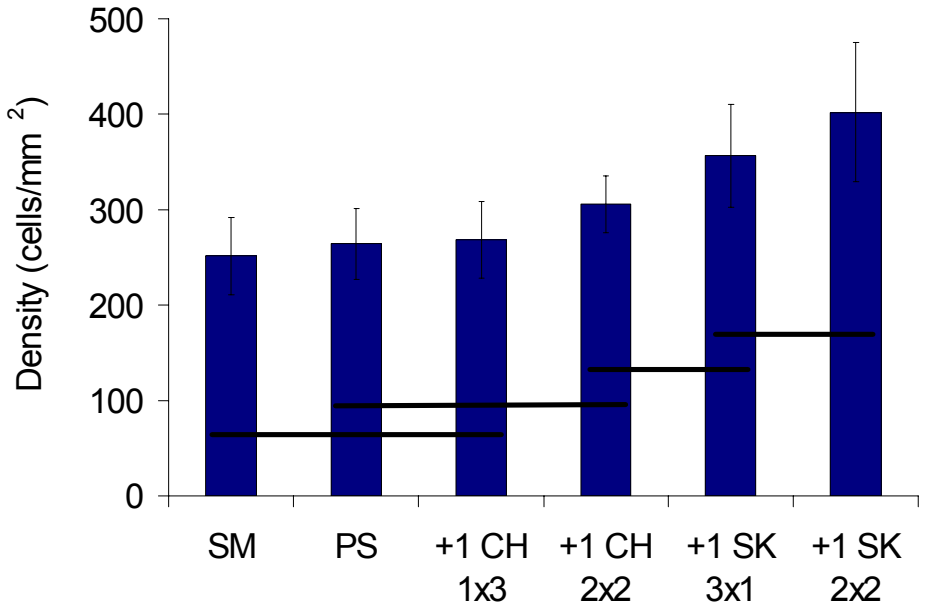

Figure 5-20. PVEC density on topographies in Assay 3. All surfaces were pretreated with 50 μg/mL fibronectin for 1 h. Tie bars connect groups with means that are not statistically different (t-test, $\alpha = 0.05$).

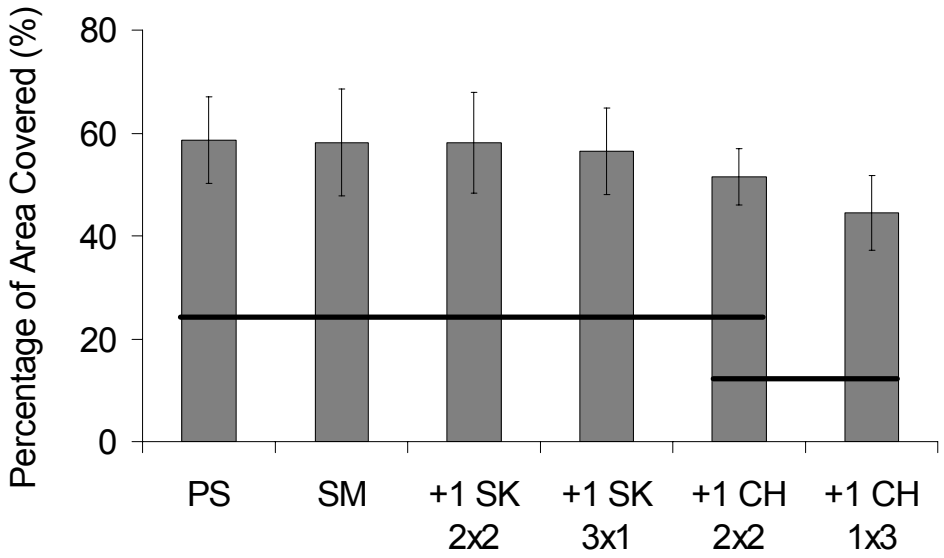

Figure 5-21. PVEC coverage on topographies in Assay 3. All surfaces were pretreated with 50 μg/mL fibronectin for 1 h. Tie bars connect groups with means that are not statistically different (t-test, $\alpha = 0.05$).

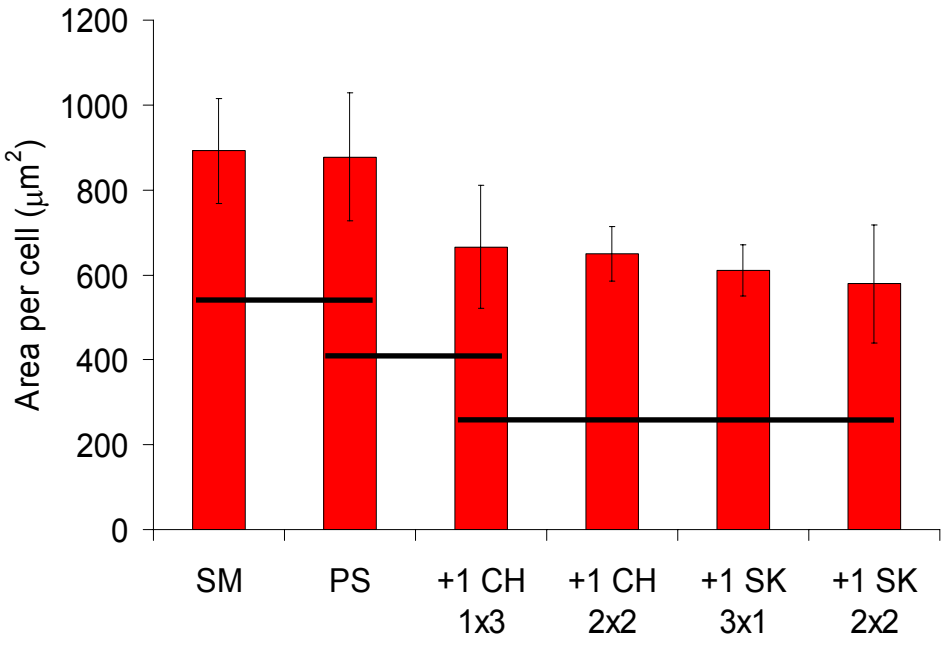

Figure 5-22. PVEC area on topographies in Assay 3. All surfaces were pretreated with 50 μg/mL fibronectin for 1 h. Tie bars connect groups with means that are not statistically different (t-test, $\alpha = 0.05$).

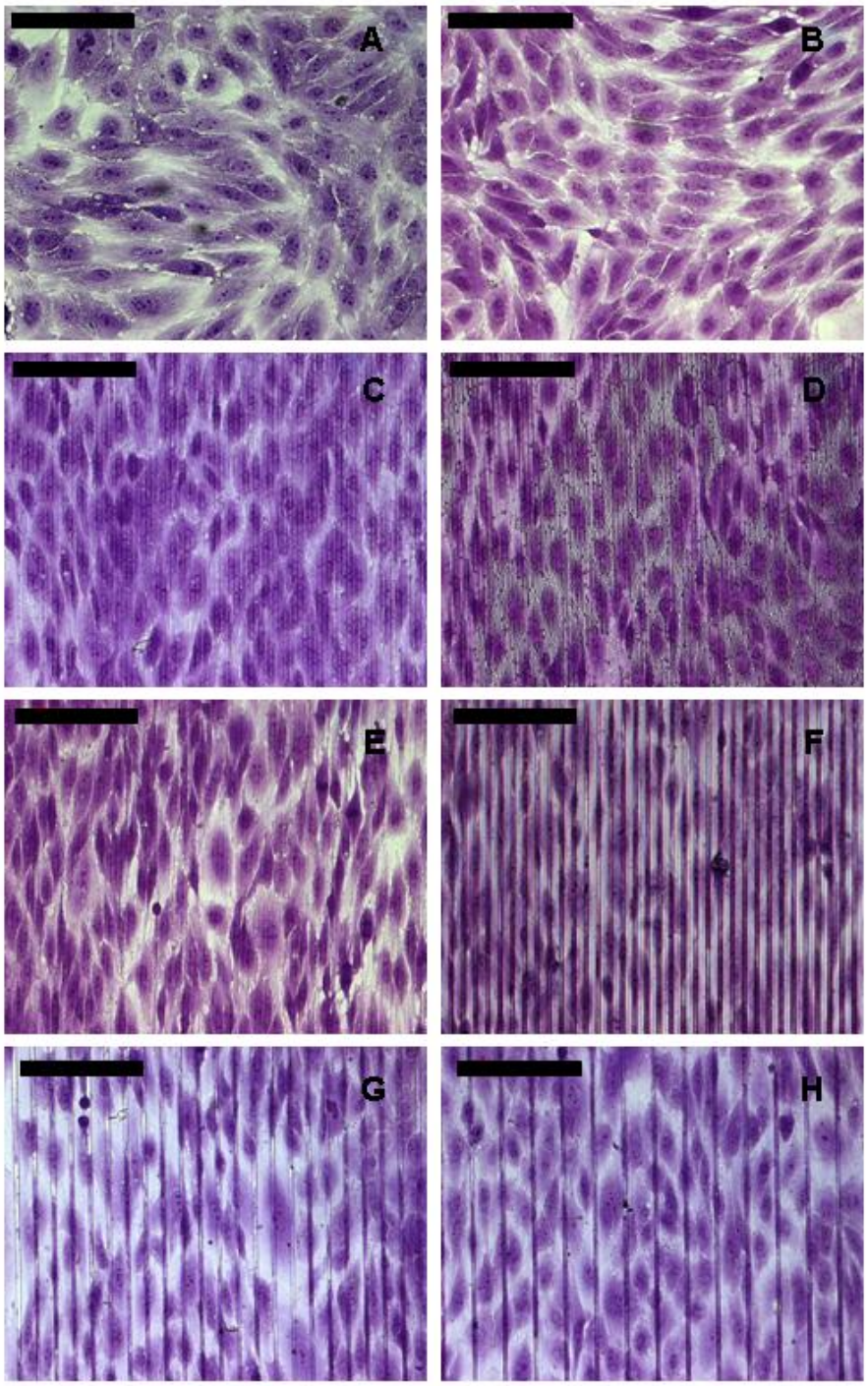

Figure 5-23. Light microscope images of PVECs grown on topographies for assay 4. A) TCP. B) smooth PDMSe. C) +1_SK_2x2 PDMSe. D) +3_SK_2x2 PDMSe. E) +1_CH_2x2 PDMSe. F) -3_CH_5x5 PDMSe. G) -3_CH_5x10 PDMSe. H) -3_CH_5x20 PDMSe. All topographies were replicated from deep-reactive-ion-etched wafers. All surfaces were pretreated with 50 μg/mL fibronectin for 1 h. Topographies are oriented vertically in all images. Scale bars represent 100 μm.

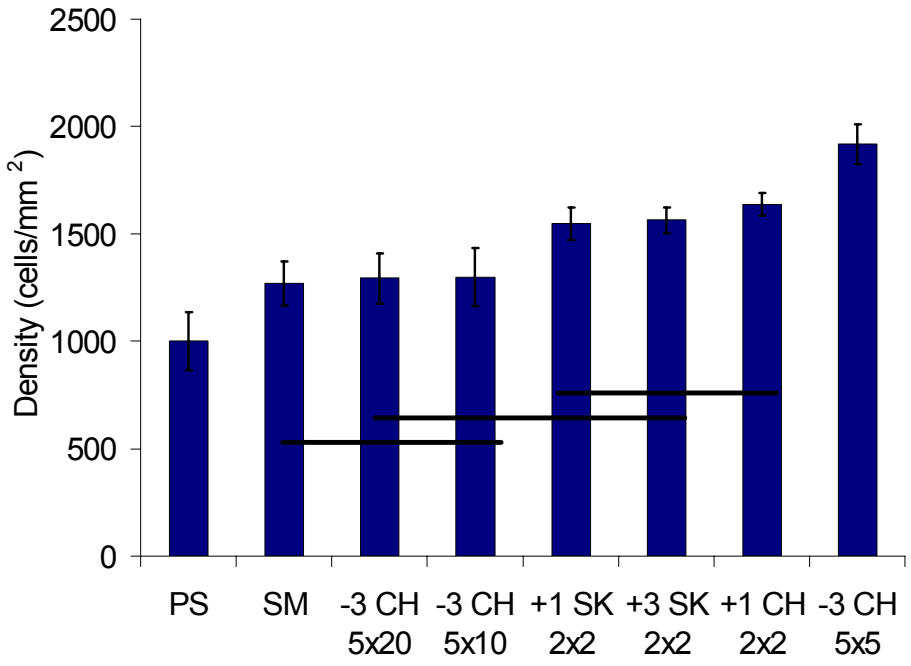

Figure 5-24. PVEC density on topographies in Assay 4. All surfaces were pretreated with 50 µg/mL fibronectin for 1 h. Tie bar connect group with means that are not statistically different (t-test, $\alpha = 0.05$).

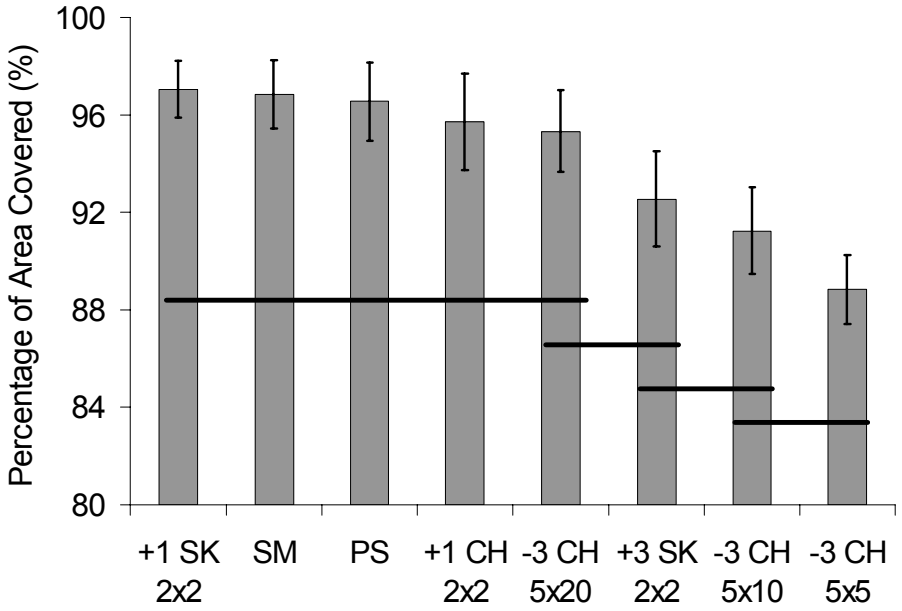

Figure 5-25. PVEC confluence on topographies in Assay 4. All surfaces were pretreated with 50 µg/mL fibronectin for 1 h. Tie bars connect groups with means that are not statistically different (t-test, $\alpha = 0.05$).

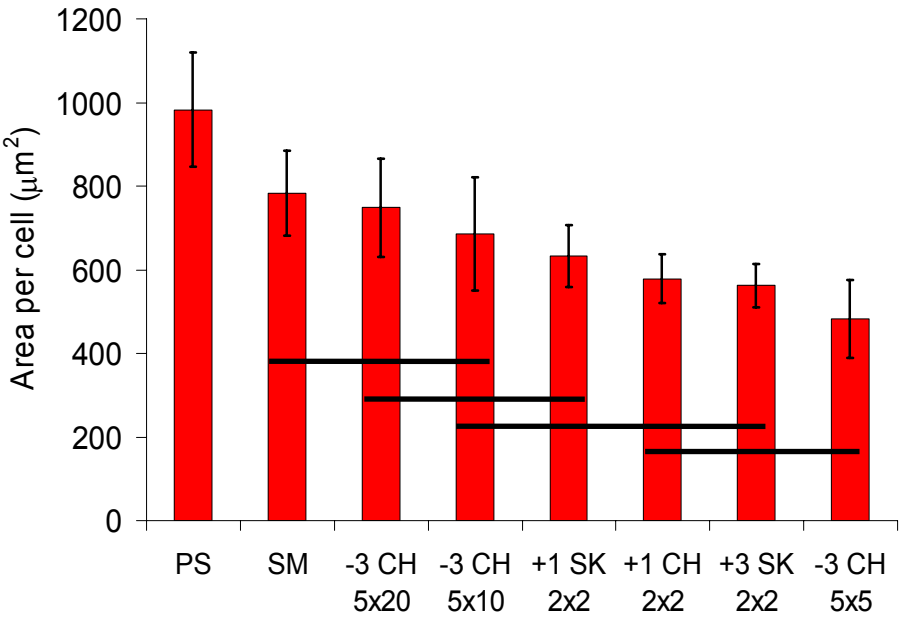

Figure 5-26. PVEC spreading on topographies in Assay 4. All surfaces were pretreated with 50 μg/mL fibronectin for 1 h. Tie bars connect groups with means that are not statistically different (t-test, $\alpha = 0.05$).

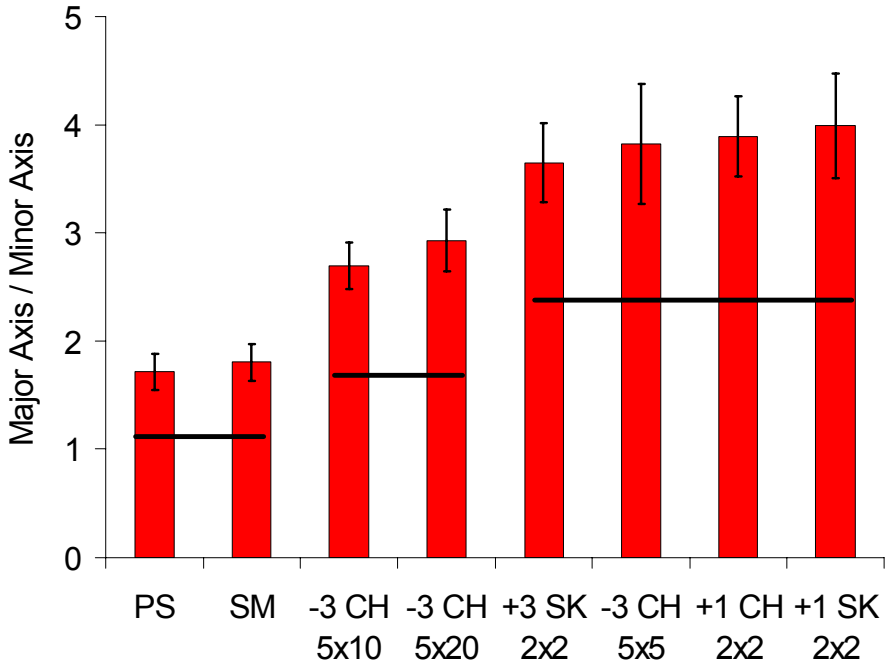

Figure 5-27. PVEC elongation on topographies in Assay 4. All surfaces were pretreated with 50 μg/mL fibronectin for 1 h. Tie bars connect groups with means that are not statistically different (t-test, $\alpha = 0.05$).

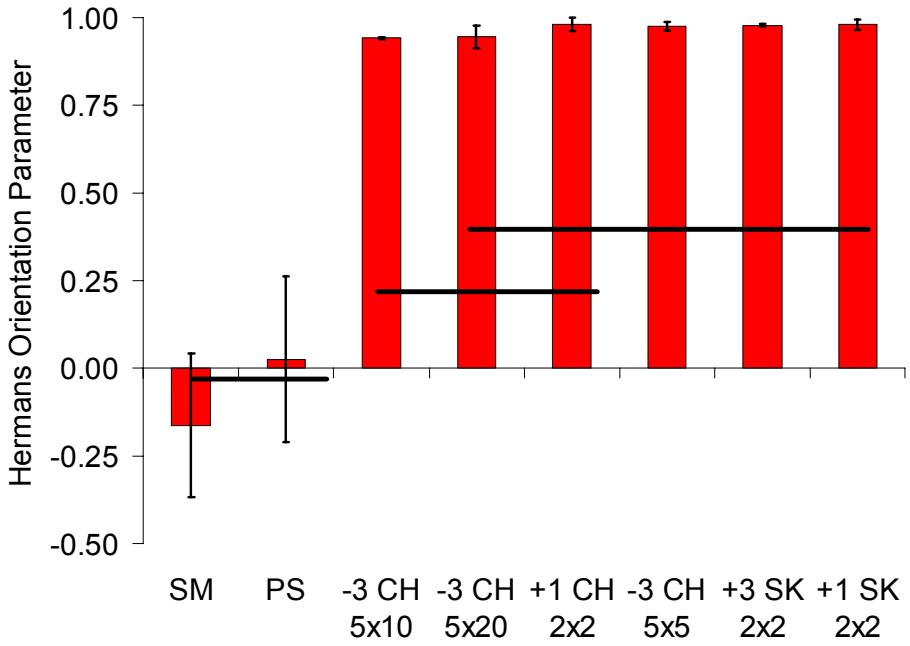

Figure 5-28. PVEC orientation on topographies in Assay 4. All surfaces were pretreated with 50 µg/mL fibronectin for 1 h. Tie bars connect groups with means that are not statistically different (t-test, $\alpha = 0.05$).

Table 5-1. Names of Topographies

Topography Description	Name
1 µm wide channels formed between 3 µm wide ridges that protrude out of the surface by 1 µm	+1_CH_1x3
3 µm wide and 1 µm spaced channels formed below the surface to a depth of 1 µm	-1_CH_3x1
2 µm wide channels formed between 2 µm wide ridges that protrude out of the surface by 1 µm	+1_CH_2x2
3 µm wide and 1 µm spaced ribs arranged in the Sharklet AF™ pattern. Ribs protrude out of the surface by 1 µm	+1_SK_3x1
2 µm wide and 2 µm spaced ribs arranged in the Sharklet AF™ pattern. Ribs protrude out of the surface by 1 µm	+1_SK_2x2
2 µm wide and 2 µm spaced ribs arranged in the Sharklet AF™ pattern. Ribs protrude out of the surface by 3 µm	+3_SK_2x2
5 µm wide and 5 µm spaced channels formed below the surface to a depth of 3 µm	-3_CH_5x5
5 µm wide and 10 µm spaced channels formed below the surface to a depth of 3 µm	-3_CH_5x5
5 µm wide and 20 µm spaced channels formed below the surface to a depth of 3 µm	-3_CH_5x5

Table 5-2. Samples for Preliminary Assay

Materials	Topography	Fibronectin (Y/N)	# of Replicates
PDMSe	Smooth	Y	2
	Smooth	N	2
	+1_CH_2x2 (DRIE)	Y	2
	+1_CH_3x1 (PR)	Y	2
	+1_SK_2x2 (DRIE)	Y	2
	+1_SK_3x1 (PR)	Y	2
Genipin Crosslinked Gelatin	Smooth	Y	2
	Smooth	N	2
	+1_CH_2x2 (DRIE)	Y	2
	+1_CH_2x2 (DRIE)	N	2

Table 5-3. Samples for Immunofluorescence Assay and Assay 3

Material	Topography	Fibronectin (Y/N)	# of Replicates
TCP	Smooth	Y	2
PDMSe	Smooth	Y	2
	+1_CH_2x2 (DRIE)	Y	2
	+1_CH_3x1 (PR)	Y	2
	+1_SK_2x2 (DRIE)	Y	2
	+1_SK_3x1 (PR)	Y	2

Table 5-4. Samples for Assay 4

Material	Topography	Fibronectin (Y/N)	# of Replicates
PS	Smooth	Y	2
PDMSe	Smooth	Y	2
	+1_CH_2x2 (DRIE)	Y	2
	+1_SK_2x2 (DRIE)	Y	2
	+3_SK_2x2 (DRIE)	Y	2
	3_CH_5x5 (DRIE) -3_CH_5x10 (DRIE) -3_CH_5x20 (DRIE)	Y	2

Table 5-5. Feature Dimensions of Topographies Determined by WLIP

Material	Topography Name	Width (μm)	Spacing (μm)	Depth (μm)
PDMSe	+1_CH_3x1 (PR)	2.8 ± 0.1	1.2 ± 0.1	0.66 ± 0.02
	+1_CH_2x2 (DRIE)	2.3 ± 0.1	1.7 ± 0.1	0.86 ± 0.03
	+1_SK_3x1 (PR)	2.5 ± 0.1	1.5 ± 0.1	0.70 ± 0.02
	+1_SK_2x2 (DRIE)	1.8 ± 0.1	2.2 ± 0.1	0.89 ± 0.02
Hydrated Gelatin	-1_CH_2x2 (DRIE)	2.4 ± 0.1	1.6 ± 0.1	0.55 ± 0.01
Dehydrated Gelatin	-1_CH_2x2 (DRIE)	2.7 ± 0.1	1.3 ± 0.1	0.77 ± 0.02

CHAPTER 6
INFLUENCE OF TOPOGRAPHY ON SHEAR STABILITY OF ENDOTHELIAL CELLS

Introduction

The overall goal of this research was to investigate the potential for microscale topographies to improve endothelial cell resistance to flow induced shear stresses. This would be a significant advance in the development of a successful small diameter vascular graft. As shown in Chapter 5, microscale topographies can be used to orient endothelial cells along with their nuclei and focal adhesions. It is proposed that this will stabilize the cells against removal by shear stresses applied parallel to the orientation direction.

Parallel plate flow chambers often have been used to evaluate cellular adhesion [71] as well as flow induced changes to cell structure [119, 120] and physiological functions [121]. These chambers generate constant shear stresses across the test substrates as defined by the following equation:

$$\tau_w = \frac{6\mu Q}{h^2 w}. \tag{6-1}$$

In this relationship τ_w refers to the shear stress at the wall (ie. sample substrate), μ is the viscosity of the fluid medium, Q is the volumetric flow rate, and h and w define the chamber height and width respectively. A derivation of Equation 6-1 can be found in Appendix B.

In this study, porcine vascular endothelial cells were cultured on microscale topographies. Both channels and the Sharklet CE™ topography were produced in fibronectin-treated polydimethylsiloxane (PDMSe) elastomer. For both microtopographies, the protruding features (ridges and ribs) were 3 μm wide, 1 μm spaced and 1 μm tall. Porcine vascular endothelial cells (PVECs) were cultured on these substrates and then exposed to a physiological shear stress (2 Pa). Cellular retention and morphological changes were then evaluated.

Materials and Methods

Design of Parallel Plate Flow Chamber

The top and bottom plates of the chamber were generously supplied by Dr. Roger Tran-Son-Tay's group. They are made of Lexan™ polycarbonate and the upper plate contains inlet and outlet ports (Fig. 6-1). The lower plate has an indentation and cut-out designed to fit a 1 inch by 3 inch glass slide. Preliminary tests of the flow chamber with a plain glass slide proved that it has a tendency to leak. Consequently, the chamber design was modified to create a better seal (Fig. 6-2). A glass slide was placed in the indentation to create a level surface and then the height and width of the chamber were defined by the use of specially prepared PDMSe gaskets.

The gaskets were prepared so that the chamber dimensions (height x width) were 0.4x17.0 mm for the preliminary study and 0.5x12.5 mm for the final study. A Harvard compact infusion pump (Model 975) was used to provide continuous and steady flow. The pump held two 60 mL syringes and these were connected though a Y-shaped adapter. The second highest flow setting was used to deliver fluid at 60 mL/min. This arrangement resulted in shear stress of 2 Pa on the test substrate for both studies based on an approximate viscosity of PBS and media (~1 cP = 0.001 Pa*s),

Production of PDMSe Topographies

Topographically modified PDMSe films were prepared by direct casting against etched silicone wafers. Two topographies were included: 2 μm channels separated by 2 μm wide ridges that are 1 μm tall (+1_CH_2x2) and the Sharklet CE™ pattern with 2 μm wide and 2 μm spaced ribs that are 1 μm tall (+1_SK_2x2). The topographically modified wafers were prepared by James Schumacher using a 19 second DRIE cycle. Prior to replication with PDMSe, wafers were rinsed with ethanol and then treated with hexamethyldizilazane (HMDS) via vapor phase

deposition for approximately 5 min. During this time, polyester sheets were taped to one side of two clean glass plates. HMDS treated wafer were placed on top of one of the plates and 1 mm thick spacers were placed at the corners of the plate. Silastic T2 was mixed (10:1 ratio of base resin to curing agent), degassed and poured over the wafers. The top place was lowered onto the PDMSe until it rested on the spacers. The PDMSe was allowed to cure for 24 h at room temperature before being removed from the mold.

Preliminary Shear Study

Sample gasket preparation

A razor blade was used to cut 16 mm wide samples from each topographically modified PDMSe film. The +1_CH_2x2 topography was 2 in long and the +1_SK_2x2 topography was 1 in long. The samples were cut to leave a 3 mm border at the ends of each length.

In order to prepare each sample gasket, transparency films were cut to create thee 17 mm by 77 mm strips. Three strips were taped together using double sided tape (a total of two tape layers) and then the laminate was taped to a polyester-sheet-covered glass plate. Next a topographically modified PDMSe sample was suctioned pattern-side-down to the center of the transparency laminate. Spacers (2 mm thick) were placed in the corners of the plate. PDMSe was mixed, degassed and poured over top. A second polyester sheet covered glass plate was then lowered on top until it rested on the spacers. The PDMSe was allowed to cure for 24 h at room temperature and then the sample gasket was cut from the film.

Samples were sterilized by soaking in 70% ethanol for 1 h. Then the depression of the sample gasket was treated with fibronectin (Biomedical Technologies, Inc.). It was supplied as a 1 mg/mL solution of 0.03 M Tris Cl buffer (pH 7.8) in 30% glycerol. It should have been diluted to 50 μg/mL in phosphate buffered saline (PBS), but it was mistakenly diluted using nanopure water. The indentation of each sample gasket was filled with 0.5 mL of the fibronectin solution

and it was allowed to adsorb for 1 h at room temperature. Samples were then rinsed 2 times each with PBS and covered with PBS until cell seeding.

Cell culture

Porcine vascular endothelial cells were generously supplied by Dr. Block (Veteran's Administration Hospital, Gainesville, FL). PDMSe sample gaskets were placed in the bottom of 150 mm diameter Petri dishes. Four samples of each type (smooth, +1_CH_2x2 and +1_SK_2x2) were included. PVECs (passage 3) were diluted to 100,000 cells/mL in 10% FBS supplemented RPMI media. Then the indentations of each sample gasket were filled with the cell suspension (~0.5 mL per sample) to give a seeding density of 4,000 cells/cm^2. Cells were allowed to settle for 4 h and then more media was added so that the final level was approximately 2mm above the gasket. Samples were incubated at 37ºC and 5% CO_2 and cells were allowed to grow for 7 days.

Shear treatment

Two samples of each type were exposed to a wall shear stress of 2 Pa using the parallel plate flow chamber. Phosphate buffered saline (PBS, 1X)) was used as the fluid medium and flow was applied at 60 mL/min for 2 minutes which represents the longest time frame possible for the 2 Pa wall shear stress on the substrates based on the syringe pump used.

Staining and imaging

Samples (both static and shear treated) were first fixed in 4% formaldehyde for 10 minutes. They were subsequently rinsed 3 times with PBS and then stained with 1% crystal violet for 5 minutes. Slides were gently rinsed in water until water remained clear. Imaging was performed using a Zeiss Axioplan 2 microscope at 400X magnifications. Eight images per sample were taken at each magnification for a total of 16 images per surface treatment and shear combination.

Images were taken from the central 1 cm wide by 2.5 cm long area of the shear samples to ensure fully developed flow had been applied. Cell density was measured by processing of the images using ImageJ software.

Final Shear Study

Gasket preparation

Samples were prepared separately from the gasket for the final shear study. The change was made so that smaller volumes of media would be needed during cell culture and so that all samples could be seeded with the same suspension of cells. Spacers (2 mm thick) were placed in the corners of a clean glass plate. PDMSe (50 g) was mixed, degassed and poured over top. A second clean glass plate was then lowered on top until it rested on the spacers. The PDMSe was allowed to cure for 24 h at room temperature and then the outline of the gasket was cut from the film. A 12.7 mm (0.5 in) wide and 76.2 mm (3 in) long section was cut from the gasket center to define the chamber dimensions. Note that all although the gasket was 2 mm thick, it compressed to 1.6 mm thick when clamped into the flow chamber. As such, the gasket provided a chamber height of 0.5 mm when combined with a 1.1 mm thick sample.

PDMSe culture well preparation

During a second preliminary study (not presented here) it was found that the PDMSe samples tended to float in the culture media. This was problematic because the endothelial cells settled on the Petri dish instead of the samples. To prevent this, a PDMSe culture well was produced which provides better adhesion to the samples. To produce the culture well, two stacks containing five 2 inch by 3 inch glass slides each were taped together using double-sided tape. The two stacks were taped side-by-side to a clean glass plate to create a 4 inch by 3 inch mold. Spacers (6 mm thick) were placed around the mold and then PDMSe (160 g) was mixed, degassed and poured over top. A second glass plate was pressed above the mold until it rested

on the spacers. The PDMSe was allowed to cure for 24 h at room temperature and then it was removed from the mold. Excess PDMSe was cut away, leaving ~5 mm thick border around the 4 inch by 3 inch well. The well was then placed in a 15 mm diameter Petri dish to provide support.

Sample preparation

Samples for the final shear study were 12.7 mm (0.5 in) wide, 76.2 mm (3 in) long and 1.1 mm thick. Each sample contained regions of smooth, +1_CH_2x2 and +1_SK_2x2 (Fig. 6-3). A razor blade was used to cut 25.4 mm wide and 12.7 mm long sections from each topographically modified PDMSe film. For each sample, one section of each of the topographies was suctioned patterned-side down to a clean glass plate with a half inch (12.7 mm) long gap between them. A fresh batch of uncured PDMSe (30 g per samples) was then mixed, degassed and poured over top. Spacers (1.1 mm thick) were used and a second glass plate was then pressed over top. The PDMSe was allowed to cure for 24 h at room temperature and then the 1 inch by 3 inch samples were cut from the film.

Four samples were suctioned to the bottom of the PDMSE culture well and then the well and samples were immersed in 70% ethanol for 1 h to sterilize. After that time, they were rinsed thee times with PBS and then 20 mL of 50 μg/mL fibronectin was pipetted over the samples in the well. The fibronectin solution was allowed to adsorb for 1 h and then the samples were rinsed thee times with PBS just prior to cell seeding.

Cell culture

Porcine vascular endothelial cells (passage 2) were generously supplied by Dr. Block (Veteran's Administration Hospital, Gainesville, FL). PVEC density was determined using a hemocytometer and then the suspension was diluted to 30,000 cells/mL in 10% FBS supplemented RPMI 1640 media. Twenty-five milliliters were placed above the samples in the

PDMSE culture well to give a seeding density of 10,000 cells/cm^2. Samples were incubated at 37ºC and 5% CO_2 and cells were allowed to grow for 3 days.

Shear treatment

A razor blade was used to cut each sample in half down its long axis. One half was immediately fixed and stained as described below and the other half was exposed to 2 Pa of wall shear stress using the parallel plate flow chamber. In this manner, four samples were shear tested and four were not. The samples were suctioned into the indentation of the gasket using a minimal amount of vacuum grease. Serum-free RPMI 1640 media was used as the fluid medium and shear was applied for 2 minutes which represents the longest time frame possible for the 2 Pa wall shear stress based on the syringe pump used.

Staining and imaging

Samples (both static and shear treated) were first fixed in 4% formaldehyde for 10 minutes. They were subsequently rinsed 3 times with PBS and then stained with 1% crystal violet for 5 min. Slides were gently rinsed in water until water remained clear. Imaging was performed using a Zeiss Axioplan 2 microscope at 400X magnifications. Twelve images were taken per surface treatment and shear combination. Images were taken from the central 1 cm wide and 38 mm long area to ensure fully developed flow had been applied. Cell density, elongation and orientation were measured by processing the images using ImageJ software as described in Chapter 5.

Statistical Methods

Two way analysis of variance (ANOVA, $\alpha = 0.05$) was used to determine if any significant differences exist among the topography and shear treatments. Mean values ±2 standard errors are reported.

Results

Preliminary Shear Study

Endothelial cells did not grow well for the preliminary shear study. The cells grew sporadically across the samples, with areas of good cell growth surrounded by regions nearly devoid of healthy cells (Fig. 6-4). The poor proliferation was attributed to the error in fibronectin treatment mentioned in the description of methods. The protein was dissolved in water rather than PBS which would have disrupted the conformation of the protein and disrupted its ability to adsorb evenly to the PDMSe surfaces.

Because of the wide discrepancies in cell proliferation within a sample, the variability in cell density was too great for any definitive conclusions to be drawn. In general, the density of cells grown in static culture did not vary among the smooth and topographically modified PDMSe samples (Fig. 6-5). The mean cell density on all samples was ~300 cells/mm^2. After exposure to 2 Pa of shear stress on the test substrate, greater differences in mean cell density were observed among the surfaces. Although statistical differences do not exist, the +1_SK_2x2 topography tended to improve cellular retention whereas the +1_CH_2x2 topography tended to decrease cellular retention relative to smooth PDMSe.

Final Shear Study

The floor of the PDMSe sample well for the final shear study must not have been level. After 3 days of cell culture, it was discovered that nearly all of the cells settled and proliferated on one sample located against a far edge of the well. Only this sample was used in the analysis of results. Cell density before exposure to flow on the other 3 samples was far too low (<1 cell/mm^2) to evaluate cell retention.

Cells were nearly confluent on the smooth and topographically modified sections of the remaining sample prior to exposure to flow (Fig. 6-6). Cell growth was much more consistent

than observed in the preliminary study. Cell density did not significantly vary with surface topography and the average cell density before flow among all surfaces was 520 ± 60 cells/mm^2 (Fig. 6-7).

The topographies induced morphological changes in the PVECs consistent with the results of Chapter 5. Cell elongation increased from 2.3 ± 0.3 on smooth fibronectin-treated PDMSe to 3.7 ± 0.3 and 3.8 ± 0.3 on the +!_SK_2x2 and +1_CH_2x2 topographies respectively (Fig. 6-8). Orientation was also increased by the topographies. Hermans parameter for the smooth control was not significantly different from zero, indicating random orientation (Fig. 6-9). The +!_SK_2x2 and +1_CH_2x2 topographies induced orientation to a similar degree, with Hermans parameter values of 0.90 ± 0.04 and 0.92 ± 0.01 respectively.

Cell density decreased significantly on all topographies after exposure to 2 Pa of wall shear stress in the flow chamber for 2 minutes (Fig. 6-7). The average settlement density after flow among all surfaces was 220 ± 40 cells/mm^2 and it did not significantly vary with topography. Likewise, cell retention was statistically equivalent on all surfaces with 43 ± 20% of cells retained (Fig. 6-10).

Closer inspection of the after flow images revealed that PVECs on both the +1_SK_2x2 and +1_CH_2x2 topographies appeared to maintain better spreading than cells on smooth fibronectin-treated PDMSe (Fig. 6-6). The cells on the topographically modified sections were spread relatively evenly across the surface, whereas the cells on the smooth section tended to be isolated to small, dense clusters. Evaluation of mean cell areas before and after flow confirmed these results (Fig. 6-11). Cell spreading on smooth fibronectin-treated PDMSe was reduced from 1,100 ± 100 μm^2 to 470 ± 100 μm^2. Alternatively, PVEC spreading on both topographies

was ~1000 μm^2 and did not significantly change after exposure to 2 Pa of shear stress on the test substrate.

Discussion

In the preliminary shear study, the +1_SK_2x2 topography tended to improve cell retention after exposure to shear whereas the +1_CH_2x2 topography tended to decrease it. Initially these results seemed promising and were consistent with the trend seen with algae spores (*Ulva*) for similar topographies with 3 μm feature heights [122]. Unfortunately, no definitive conclusions regarding cell retention can be drawn from the preliminary study because the PVECs response was too variable due to inadequate pretreatment of the PDMSe surfaces with fibronectin. The results of this study clearly demonstrate that surface chemistry is more important that topography when attempting to support endothelial cell growth.

Unfortunately, the trends in endothelial cell retention suggested by the preliminary study could not be confirmed. The final shear study indicates cell retention is not significantly improved by either topography, at least not in terms of cell density. Alternatively, both the +1_SK_2x2 and +1_CH_2x2 topographies enhance the ability of PVECs to maintain cell spreading during exposure to flow. This is consistent with the hypothesis outlined in Chapter 1 which states that cells are removed when exposed to flow because they must break focal adhesions to adapt their morphology. These results suggest that endothelial cell retention might be improved by further optimization of material chemistry and topographical dimensions.

The discussion from Chapter 5 on the possible infilling of the topographical recesses with fibronectin needs to be revisited here. It is unclear what if any affect the protein adsorption had on the shape of the topography. It is conceivable that the protein may have filled in the topography to some degree so that the cells were presented with a smoother surface than what is indicated by the reported feature dimensions.

In the most extreme scenario of infilling, fibronectin may be wicked away from the ridge tops and completely fill the topographical recesses. In such a case, the resulting surface is smooth but still has the potential to direct cellular growth based on patterned chemical and mechanical (due to phase contrast) cues. The fibronectin in the recesses would be thicker than a monolayer and therefore more susceptible to being partially desorbed by flowing media. This would help explain why so many cells were removed from the topographically modified surfaces despite the fact that the PVECs were aligned in the flow direction. As such, combining the topographies with a different material or switching to two-dimensional chemical patterns might yield better results.

Conclusion

This study investigated endothelial cell adhesion to topographies with 1 μm tall features having 2 μm lateral dimensions. Such topographies incorporated into fibronectin-treated PDMSe help PVECs maintain cell spreading but do not improve cell retention after exposure to 2 Pa of shear stress on the substrate. The adsorbed fibronectin layer should be characterized in order to gain further insight into the nature of contact guidance observed in this study. Endothelial cell retention may be improved by combining the topographies with a different material or by switching to two-dimensional chemical patterns.

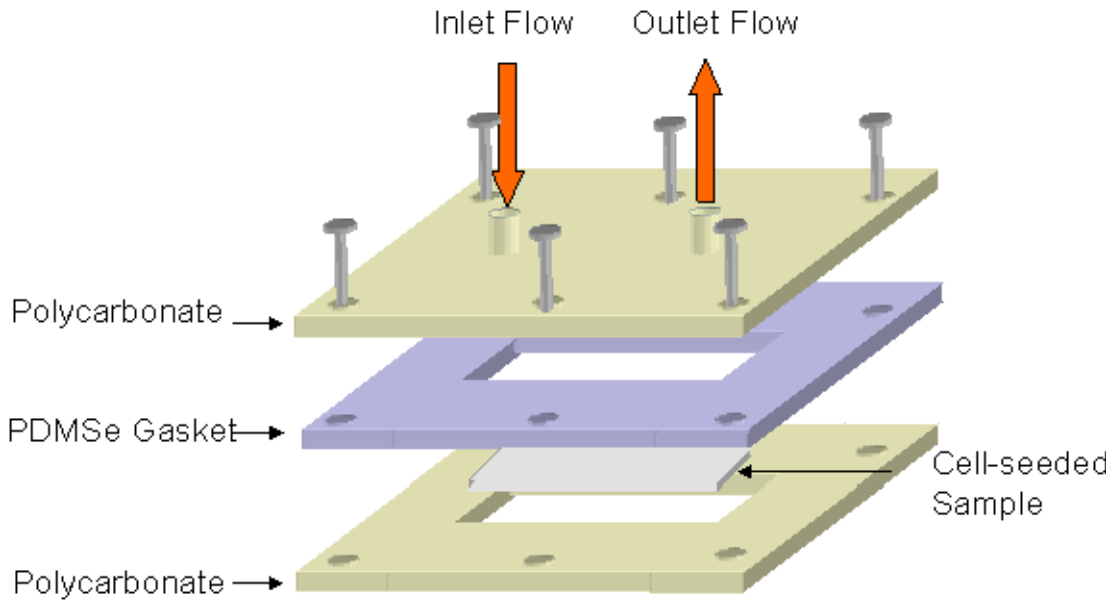

Figure 6-1. Original design of flow chamber.

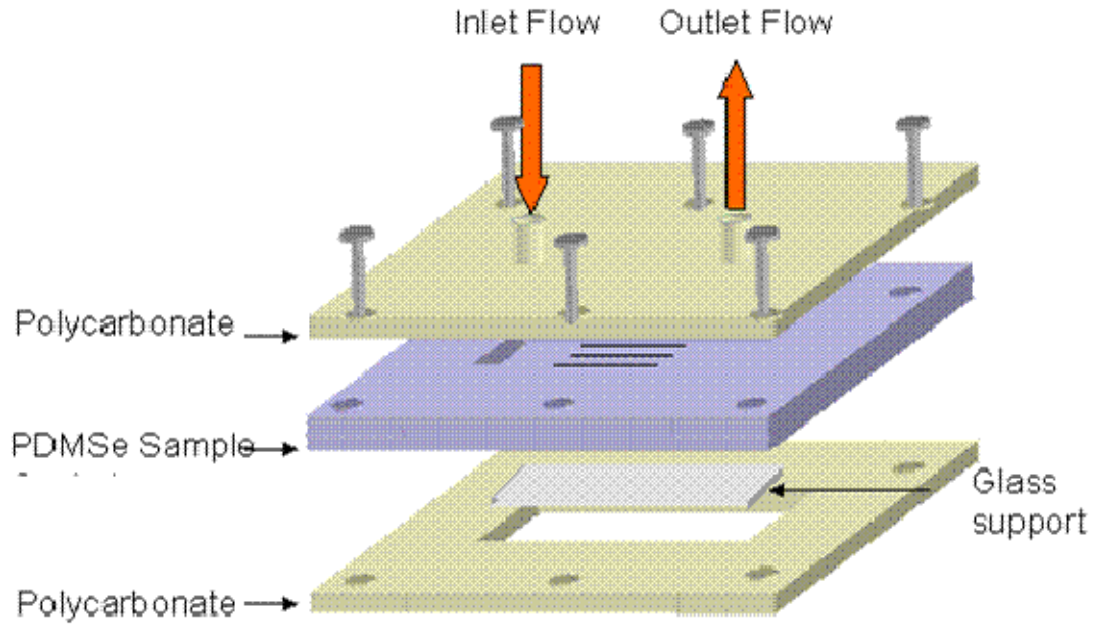

Figure 6-2. Modified design of flow chamber.

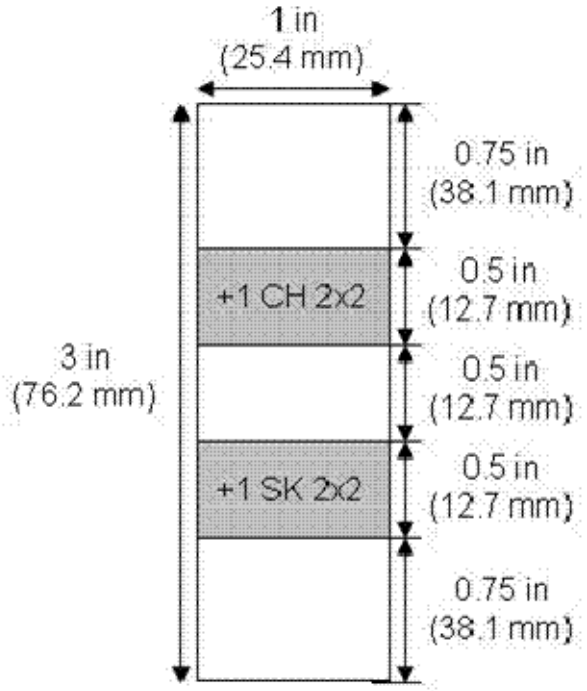

Figure 6-3. Layout of samples for the final shear study. White regions depict smooth areas of the sample.

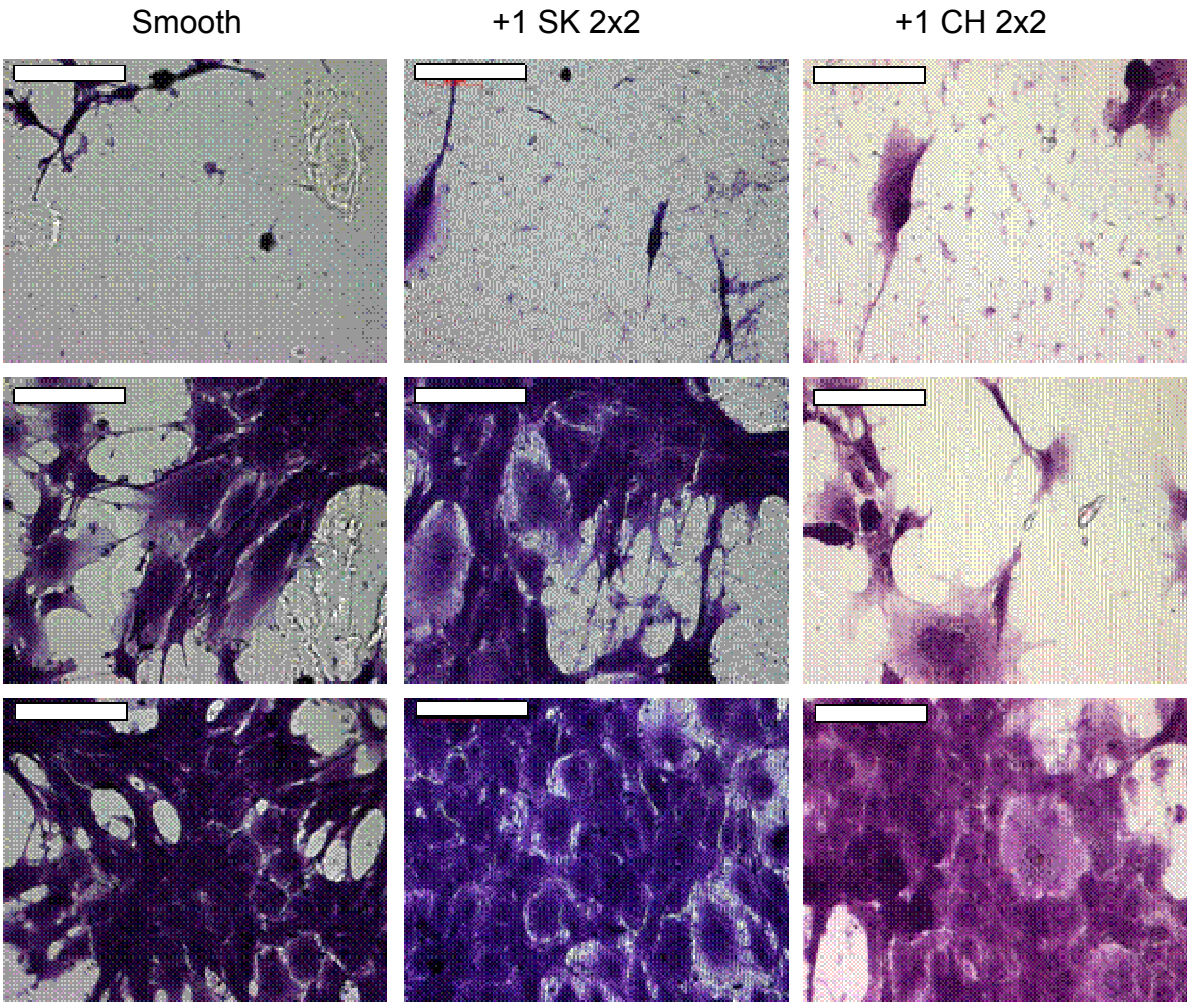

Figure 6-4. PVECs before exposure to flow in the preliminary shear study. Images were taken at 400X. Thee images (low, middle and high density) are given per surface type to indicate the high variability observed. Scale bars represent 100 µm

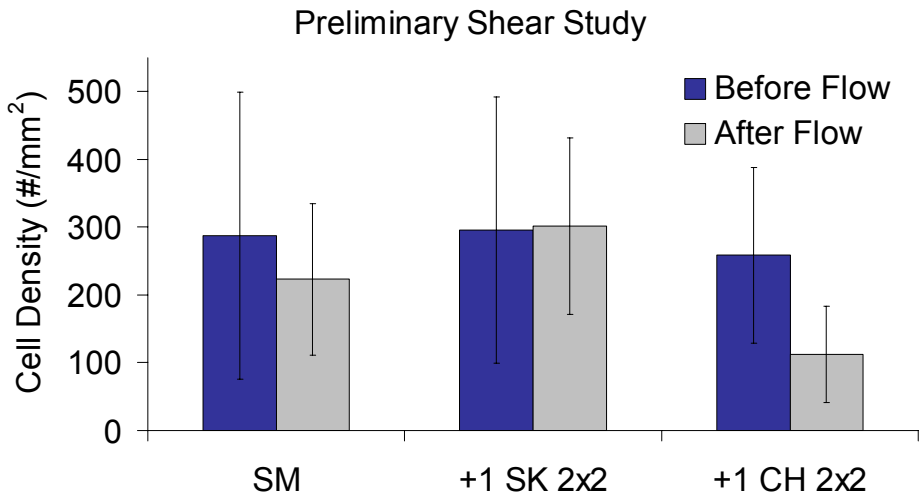

Figure 6-5. Density of PVECs before and after flow in the preliminary shear study. Smooth and textured PDMSe samples were fibronectin treated. Cells were grown for 7 days and then exposed to 2 Pa wall shear stress for 2 min. There are no significant differences between any of the treatments (ANOVA, $\alpha = 0.05$).

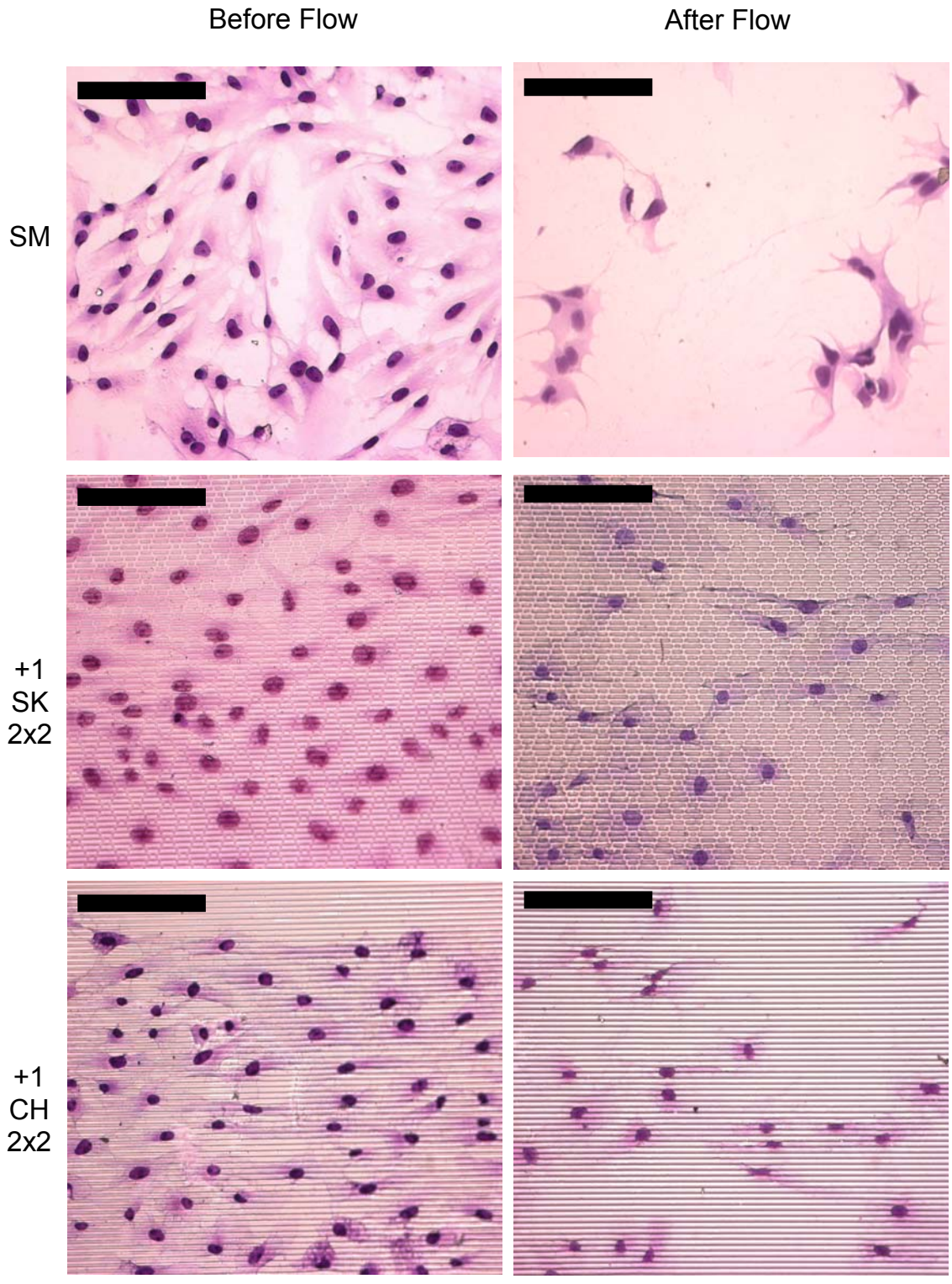

Figure 6-6. PVECs grown on topographies in the final shear study. Cells were grown on smooth, +1_SK_2x2 and +1CH_2x2 fibronectin treated PDMSe. Images were taken at 400X before and after exposure to flow. Topographical features are oriented horizontally in the images. Scale bars represent 100 μm

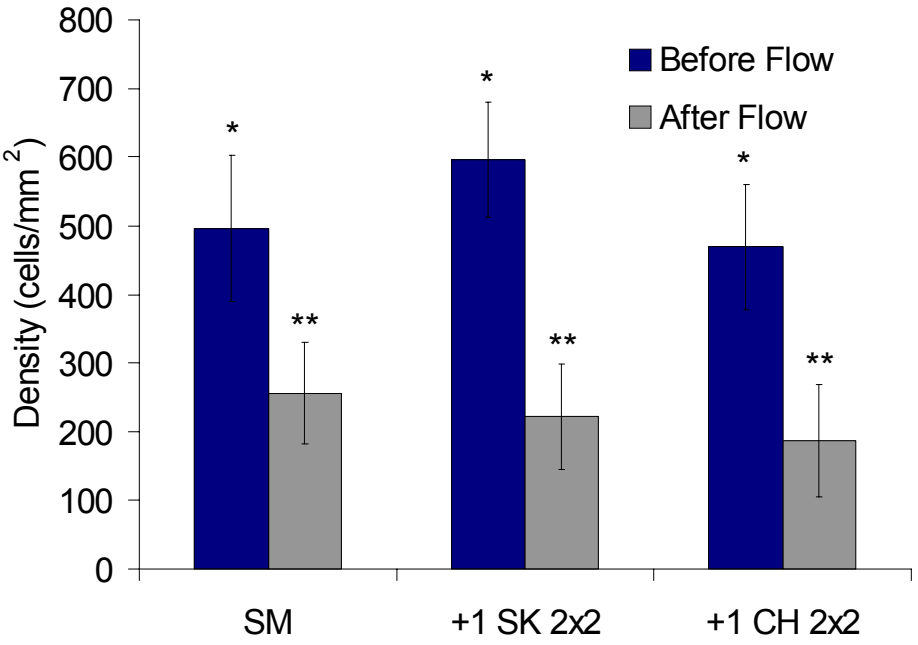

Figure 6-7. Density of PVECs on topographies before and after flow in the final shear study. Cells were grown on smooth and topographically modified PDMSe for 3 days and then exposed to 2 Pa wall shear stress for 2 min. Asterisks denote statistically indistinct groups (t-test, $\alpha = 0.05$).

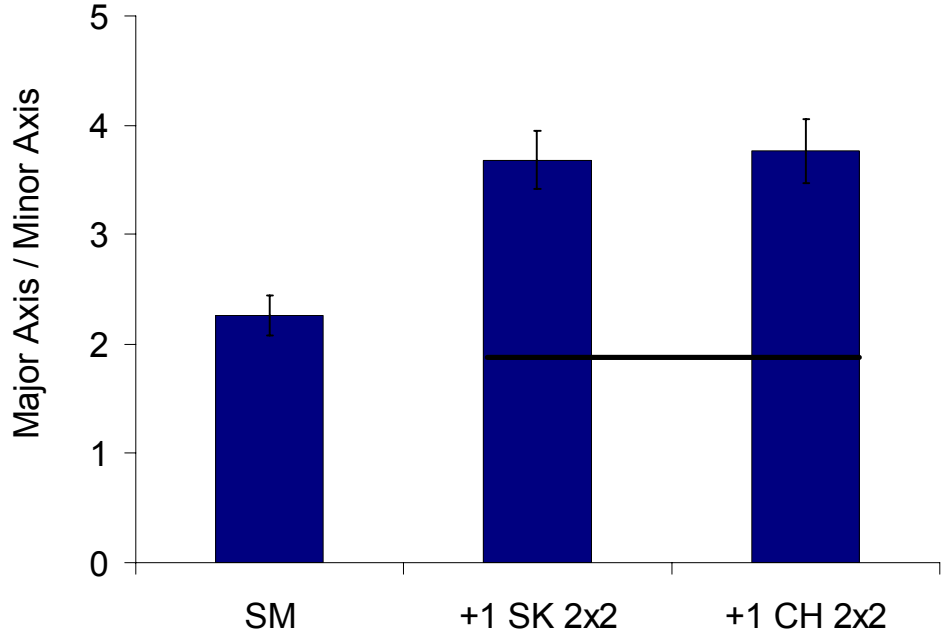

Figure 6-8. Elongation of PVECs on topographies before flow in the final shear study. Cells were grown on smooth and topographically modified PDMSe for 3 days. Tie bars denote statistically indistinct groups (t-test, $\alpha = 0.05$).

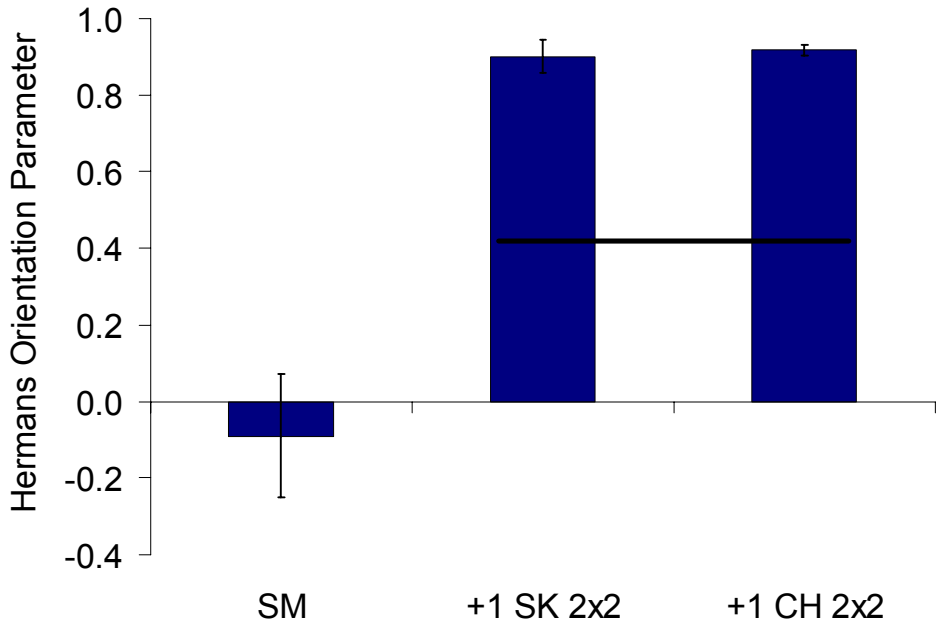

Figure 6-9. Orientation of PVECs on topographies before flow in the final shear study. Cells were grown on smooth and topographically modified PDMSe for 3 days. Tie bars denote statistically indistinct groups (t-test, $\alpha = 0.05$).

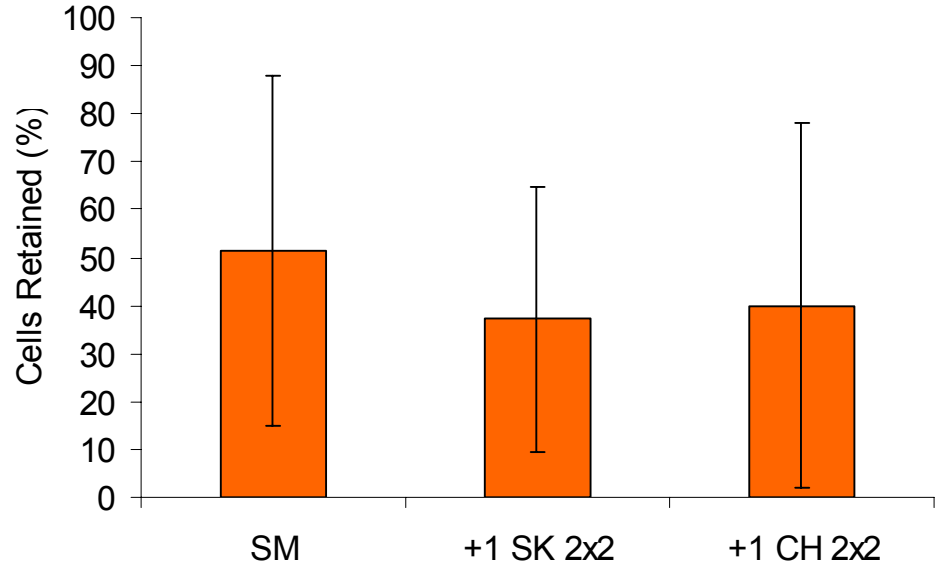

Figure 6-10. Retention of PVECs based on topography in the final shear study. Cells were grown on smooth and topographically modified PDMSe for 3 days and then exposed to 2 Pa wall shear stress for 2 min. Retention does not vary significantly among the surfaces (t-test, $\alpha = 0.05$).

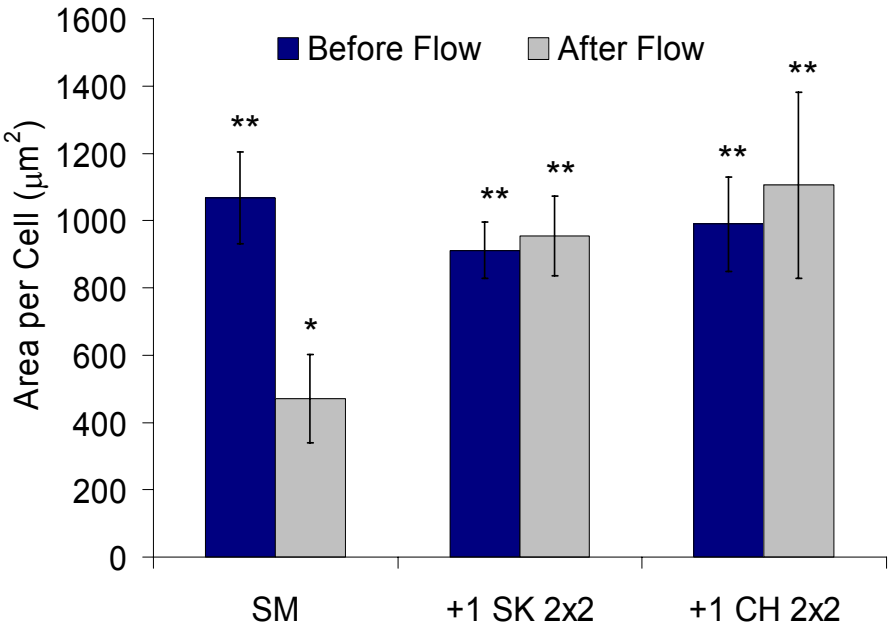

Figure 6-11. Average area for PVECs on topographies before and after flow in the final shear study. Cells were grown on smooth and topographically modified PDMSe for 3 days and then exposed to 2 Pa wall shear stress for 2 min. Asterisks denote statistically indistinct groups (t-test, $\alpha = 0.05$).

CHAPTER 7
CONCLUSIONS AND FUTURE WORK

Conclusions

The ability to improve endothelial cell retention to biomaterial surfaces would be a significant advancement in the search for a suitable synthetic small diameter vascular graft. This work is the first known attempt to evaluate the influence of engineered microscale topographies on endothelial cell retention during exposure to flow. The engineered microtopographies were designed to orient endothelial cells in static culture with the goal of increasing their resistance to shear.

Engineered topographies significantly influence both wettability and biological adhesion to biomaterials. The topographies were developed though insights gained from classical wetting theories. It was shown that the water contact angle of hydrophobic PDMSe can be increased from 108 ± 4º to 135 ± 3º though properly scaled topographies. Channel topographies with widths ranging from 5 to 20 μm and a depth of 5 μm increase alignment of PVECs relative to smooth PDMSe. Endothelial cells settle within the channels and do not migrate over ridges, preventing confluence from being reached.

Based on this earlier work with cell adhesion to fibronectin-treated PDMSe microtopographies, it was decided that smaller topographical features would be necessary to achieve confluence. A feature width and spacing of 2 μm was selected based on the size of focal adhesions in endothelial cells. Additionally, gelatin was investigated for its ability to be micropatterned and maintain shape. Because gelatin dissolves readily in water under physiological temperatures, two crosslinking systems were investigated for their ability to stabilize the film. Genipin and glutaraldehyde were found to be equally efficient at improving modulus, but genipin is far better at decreasing the swelling of gelatin in water. The results

indicate that 10% (w/w) genipin in gelatin (2.9% MEQ) is the most efficient choice for stabilizing the films. It was shown that 2 μm features were sufficiently replicated in gelatin films of this composition.

Porcine vascular endothelial cells (PVECs) were cultured on genipin crosslinked gelatin and PDMSe substrates. Unfortunately, the cells would not grow on the gelatin substrates even after extending leaching of genipin into water and fibronectin adsorption to the gelatin surface. It is suspected that the toxicity of residual unreacted genipin is too high for the cells to remain viable. Cells grew to confluence on smooth and micropatterned PDMSe samples with adsorbed fibronectin and the topographies resulted in a significant increase in focal adhesion and nuclear alignment. Additionally PVECs on some of the topographies spread so that the average area occupied per cell more closely approximated that of endothelial cells found in vivo.

Endothelial cell adhesion to topographies with 1 μm tall features having 2 μm lateral dimensions was investigated in shear studies. Such topographies incorporated into fibronectin-treated PDMSe help PVECs maintain cell spreading but do not improve cell retention after exposure to flow generating 2 Pa shear stress on the test substrate. The adsorbed fibronectin layer should be characterized in order to gain further insight into the nature of contact guidance observed in this study. Endothelial cell retention may be improved by combining the topographies with a different material or by switching to two-dimensional chemical patterns. The ability to improved endothelial cell retention would be a great step forward in the development of viable synthetic small diameter vascular grafts.

Future Work

Future directions of this project could include further examination of the alignment of cytoskeletal components to microtopographies as well as the examination of the physiological state of the endothelial cells as a function of the topography. In particular, the alignment of actin

filaments with flow has been discussed in the literature and it would be a nice advance if this could be evaluated on the microtopographies presented here as well. This was one of the goals of the fluorescent cell culture assay in Chapter 5, but the resolution of the images was not high enough to achieve this. It would be recommended that a higher aperture objective be used to improve this so that individual actin filament bundles could be distinguished from each other.

Even though cells grew to confluence on the textured substrates that does not necessarily indicate that they are performing normal biological functions. Endothelial cells are responsible for maintaining the homeostasis of the vasculature. Endothelial cells accomplish this though the release and expression of factors which affect coagulation state, cellular proliferation and leukocyte trafficking. One indicator of endothelial dysfunction is the impairment of endothelial nitrous oxide formation which modulates vessel tone [123]. This results in stiffening of the vessel wall which is associated with atherosclerosis. Additionally, it has been shown that endothelial production of nitrous oxide modulates platelet adhesion which is a hallmark of inflammation [124]. Release of nitrous oxide into the culture media by cells grown on the textured substrates should be examined as an indicator of the physiological state of the cells.

Another indication of endothelial dysfunction is the induction of adhesive glycoproteins on the cell surface. During inflammation, activated endothelial cells present selectin molecules to their surfaces which bind with lectin molecules on leukocytes in the blood. For instance, E-selectin on endothelial cells (an inducible glycoprotein receptor) binds with Sialyl Lewis X of various leukocytes. As demonstrated by Feinberg, atomic force microscopy (AFM) could be used to probe the presence of E-selectin on endothelial cells cultured on the microtopographies though the use of a tip modified with Sialyl Lewis X [54]. Additionally, leukocytes isolated

from blood could be exposed to endothelial cells cultured on the microtopographies within a parallel plate flow chamber to examine their interaction under controlled shear.

It would be interesting to also investigate whether the engineered topographies can be used to sort out robust cells from a population of cultured endothelial cells. Among any given cell population, a distribution of cell viabilities exists. As shown in Chapter 6, the endothelial cells that remain on the engineered topographies maintain spreading better than the cells remaining on the smooth control. The cells that remain may have survived because of an inherent biological advantage. Dr. Mark Segal (Department of Nephrology, University of Florida) suggests that it would be beneficial to re-culture the remaining cells to confluence and then expose to flow again to determine if shear resistance is improved in the second generation.

In addition to the proposed studies on actin alignment and endothelial functions, there is also a need for further research into producing a microtextured hydrogel capable of supporting endothelial cell growth. This would be especially important in the development of a tissue engineered vascular graft because the supporting membrane would need to allow the transport of water and nutrients. Genipin crosslinked gelatin, the hydrogel examined here, was capable of replicating microscale topographic features with adequate mechanical stability but endothelial cells did not proliferate on it *in vitro*. This might be able to be accomplished though a better process of leaching unreacted genipin from the gelatin. Genipin is more soluble in ethanol than water and so an extended (several days) soak in 70% ethanol may be sufficient. Gelatin would remain swelled while unreacted genipin should diffuse to the surrounding ethanol. Additionally, extended soaks under *in vitro* conditions (RPMI 1640 media at 37ºC) may also work. If work is continued with this hydrogel, it would also be beneficial to examine its pore structure by capturing scanning electron microscope (SEM) images of lyophilized samples.

The ability to improve endothelial resistance to shear removal while maintaining normal cellular function would be a significant advance toward engineering an effective small diameter vascular graft.

APPENDIX A
SUMMARY OF LITERATURE ON CELLULAR RESPONSES TO TOPOGRAPHY

Table A. Chronological Listing of Literature on Cellular Responses to Topography

Year	Author(s)	Material(s)	Topography	Cell Types(s)	Results
1911	Harrison [125]	spider webs	cylindrical	frog embryonic neuronal cells	spindle shape cells long projections align with fibers
1914	Harrison [41]	spider webs and clotted plasma	cylindrical	mesenchymal stem cells from sea urchin embryo frog embryonic neuronal cells chicken embryonic neuronal cells	cells aligned to the fibers
1979	Ohara and Black [126]	polystyrene epoxy	channels - 2 and 10 µm wide with 5 to 30 µm repeat spacing depth not indicated	chick heart fibroblasts murine epithelial cells	percent aligned cells increased with decreasing spacing cells bridged 2 and 20 µm channels
1982	Wilkinson et al. [127]	serum-coated glass	channels - 2 µm wide and 2 µm deep	human neutrophil leukocytes	cells were more likely to migrate along channels than across them
1983	Brunette et al. [128]	titanium-coated silicon	channels (V shaped) - 70, 130 and 165 µm wide with 80, 140 and 175 µm repeat spacing	human gingivival cells porcine epithelial cells	cells aligned to long axis of channels epithelial cells didn't bend around ridges cells migrated along channels
1986	Brunette [129]	titanium coated silicon epoxy replicates and photoresist	channels (square and V-shaped) - 0.5 to 60 µm depth and 30 to 220 µm repeat spacing	porcine periodontal ligament epithelial cells	cells aligned to channels orientation increased with decreased spacing some cells crossed ridges and extended into channels migration directed by channels deep depth enhanced guidance of cells
1986	Dunn and Brown [130]	quartz	channels - 1.65 to 8.96 µm wide with 3.0 to 32.0 µm repeat spacing and 0.69 µm depth	chick heart fibroblasts	alignment depended greater on ridge width than spacing alignment increased with decreasing ridge width
1986	Brunette [131]	titanium coated silicon epoxy replicates and photoresist	major channels (square and V-shaped)- 5 to 120 µm depth (width not indicated) minor channels - 2 µm deep on floor at 54° to major channels	human gingivival fibroblasts	cells aligned on channels and flat ridges cells oriented preferentially with major channels cells oriented with minor channels if no major channels

Table A. Continued

Year	Authors	Material(s)	Topography	Cell Types(s)	Results
1987	Clark et al. [132]	Perspex	steps - 1, 3, 5, 10 and 18 µm heights	BHK cells chick embryonic neural cells chick heart fibroblasts rabbit neutrophils	as step height increased, cells oriented more and were less likely to cross the step rabbit neutrophils crossed 5 µm steps twice as often as other cell types
1987	Hoch et al. [133]	polystyrene	ridges - 0.5 to 100 µm wide and 0.5 to 62 µm spacing with 0.03 to 5 µm heights	Uromyces appendiculatus fungus	differentiation maximized on 0.5 µm tall ridges no differentiation on ridges shorter than 0.25 µm or taller than 1.0 µm germ tubes highly oriented on ridges spaced 0.5 to 6.7 µm
1988	Chehroudi et al. [133]	epoxy	channels (v shaped) - 17 µm wide and 10 µm deep with 22 µm wide ridges	porcine periodontal ligament epithelial cells rat parietal implant model	channels increased epithelial attachment and orientation shorter length epithelial attachment and longer connective tissue attachment to channel sections of implant compared to smooth parts channels impeded epithelial down growth
1988	Wood [134]	quartz	channels - .98 to 4.01 µm wide and spaced with 1.12 to 1.17 µm depths	mesenchymal tissue cells	cells migrated along channels highest alignment seen on widest repeat spacing
1989	Campbell et al. [43]	Versapor filters PDMS coated filters	Pore diameters – 0.4 to 3.6 µm	subcutaneously implanted into dogs	nonadherent, contracting capsules around implants with pore diameters < 0.5 µm thin, tightly adhered capsules on implants with pores from 1.4 to 1.9 µm pores ≥ 3.3 µm infiltrated by inflammatory tissue little variation with respect to surface chemistry

Table A. Continued

Year	Authors	Material(s)	Topography	Cell Types(s)	Results
1990	Chehroudi et al. [135]	titanium-coated epoxy	channels (square and V-shaped)- 30 µm repeat spacing with 3,10 or 22 µm depth; 7 and 39 µm repeat spacing with 3 or 20 µm depth	rat parietal implant model	endothelial cells attached to smooth and 3,10 µm channels endothelial cells bridged 22 µm channels fibroblasts encapsulated smooth and 3,10 µm channels fibroblasts inserted into 22 µm channels epithelial down growth greatest on smooth and channels oriented parallel to implant length epithelial down growth least on 10 and 22 µm channels perpendicular to implant length
1990	Clark et al. [136]	Perspex	channels - 4-24 µm repeat with equal width and spacing and 0.2 to 1.9 µm depths	BHK and MDCK	alignment inversely proportional to spacing and directly related to depth alignment influence by depth more than spacing
1991	Schmidt and von Recum [44]	silicone	dimples - 2, 5 and 8 µm wide/spaced; 0.38 to 0.46 µm high	murine peritoneal macrophages in vivo study in rabbits	2 and 5 µm textures yielded less mononuclear cells and thinner fibrous capsules cells on 2 and 5 µm textures were more elongated and contained more pseudopods
1991	Clark et al. [136]	Quartz with poly-l-lysine adsorption	channels - ~130 nm wide and ~130 nm spaced at depths of 100, 210 and 400 nm	BHK MDCK chick embryonic neurons	BHK alignment increased with depth single MDCK aligned perfectly on all and elongation increased with depth epithelial islands of MDCK and all embryonic neurons unaffected by the topography

Table A Continued

Year	Authors	Material(s)	Topography	Cell Types(s)	Results
1993	Clark et al. [137]	quartz treated with hydrophobic silane and laminin	chemical stripes - 2,3,6,12 and 25 µm wide with equal spacing and 2 µm stripes spaced by 50 µm	chick embryo neurons murine dorsal root ganglia neurons	alignment decreased with decreased width growth cones bridged narrow non adhesive stripes neurite branching reduced by 15 µm stripes
1993	Meyle et al. [138]	epoxy	channels (square) - 0.5 µm width and sapce with 1 µm depth	human gingivival fibroblasts	cells aligned with channels and either bridged or conformed to features
1993	Meyle et al. [139]	epoxy	channels (square) - 0.5 µm width and space with 1 µm depth	human gingivival fibroblasts	cellular prostheses did not extend into channel corners cytoskeletal elements oriented along channels
1993	Oakley and Brunette [140]	titanium-coated silicon	channels (V-shaped) - 15 µm wide and spaced with 3 µm depth	human gingivival fibroblasts	microtubules oriented at bottom of channels at 20min actin first observed at wall-ridge edges after 40 to 60min most cells had aligned focal contacts by 3hrs
1994	Meyle [141]	PDMS treated by radio frequency glow discharge	shannels (square) - 1 µm wide, 4 µm spaced and 1 µm deep	human gingivival fibroblasts	cells and focal contacts aligned with channels
1995	Webb et al. [142]	chrome-plated quartz coated with poly-l-lysine	channels - 0.13 to 4.01 µm wide and 0.13 to 8 µm spaced with 0.1 to 1.17 µm depths	rat optic nerve oligodendrocytes (ONOs) optic nerve astrocytes (ONAs) hippocampal and cerebellar neurons (HCNs)	ONOs and ONAs aligned with channels HCNs did not align ONAs showed extensive network of actin stress fibers while ONOs did not ONOs alignment maximized when channel width same as axon diameter
1995	Chesmel and Black [143]	polystyrene	channels - radial arrays of 5 µm long channels at 1° intervals;, 0.5 µm wide and 0.5 or 5 µm deep	rat calavarial cells	multi-layer protein adsorption confluence in 4 days ECM in 7 days
1995	Chou et al. [144]	titanium-coated silicon treated with radio frequency glow discharge	channels (V shaped) - 3 µm wide with 6 to 10 µm repeat spacing depth not indicated	human gingivival fibroblasts	cells aligned and secreted more fibronectin on channels twice as much ECM on channels

Table A. Continues

Year	Authors	Material(s)	Topography	Cell Types(s)	Results
1995	den Braber et al. [145]	PDMS treated with ultraviolet (UV) light and radiofrequency glow discharge (RFGD)	channels (square) – 2, 5 and 10 µm wide with equal spaces and 0.5 µm depth	rat dermal fibroblasts	2 and 5 µm channels induced stronger orientation than 10 µm channels growth lower on UV treated surface than RFGD treated surface
1995	Meyle et al. [146]	silicon dioxide	channels - 0.5 µm wide and spaced and 1 µm deep	human fibroblasts gengivival keratinocytes neutrophils, monocytes macrophages	100% of fibroblasts and 20% of macrophages aligned no orientation of keratinocytes or meutrophils
1995	Oakley and Brunette [147]	titanium coated silicon treated with radio frequency glow discharge	channels (V shaped) - 15 µm wide and spaced and 3 µm deep	porcine epithelial cells	cells oriented along channels actin filaments and microtubules oriented along wall and ridges cell alignment less variable within single cells than clusters of cells
1995	Wojciak-Stothard et al. [148]	quartz	channels - 0.5, 5, 10 and 25 µm wide with equal spacing and 0.5 and 5.0 µm depths	murine P388D1 macrophages	cells spread faster on shallower channels cells elongated faster on deeper channels cells elongated more on wider channels channels increased F-actin during initially attachment
1995	Wojciak-Stothard et al. [149]	quartz	channels - 5, 10 and 25 µm widths and 0.5, 1, 2 and 5 µm depths; spacing not indicated	BHK cells	F-actin condensation at discontinuities in topography condensation typically at right angles to channel edge with 0.6 µm periodicity vinculin orientation similar to actin microtubules formed after 30min
1996	den Braber et al. [98]	silicon treated with radio frequency glow discharge	channels - 2, 5 and 10 µm wide/spaced and 0.5 µm tall	rat dermal fibroblasts	proliferation did not vary with texture alignment of cells increased with decreasing channel width
1996	den Braber et al. [150]	PDMS treated with radio frequency glow discharge	channels - 1 to 10 µm wide and 1 to 10 µm spaced with 0.45 and 1.00 µm depths	rat dermal fibroblasts	cells oriented on ridge ≤4 µm wide channel width and depth did not affect cellular alignment

Table A Continued

Year	Authors	Material(s)	Topography	Cell Types(s)	Results
1996	Britland et al. [151]	quartz	channels - 100, 50, 25, 12 and 5 µm repeats with 0.1, 0.5, 1, 3, and 6 µm depths microcontact printing (µCP) on smooth, in channels, on ridges and perpendicular to topography	BHK21 C13	cells aligned strongest to 25 µm wide µCP and 5 µm wide, 6 µm deep channels stress fibers and vinculin aligned with µCP and channels cell alignment enhanced on parallel channels and µCP cells aligned to adhesive tracks on channels with matched pitch strength of cues became more matched when channels became narrower and deeper
1996	Matsuda and Sugawara [47]	photoreactive poly(N,N-dimethylacrylamide -co-3-azidostyrene on tissue culture PS	channels - 130, 80, 60, 40 and 20 µm wide spaced 20 µm apart	bovine aortic endothelial cells	cells avoided photoreactive regions & aligned in channels alignment increased with decreased channel width
1996	Mrksich et al. [48]	polyurethane coated with gold and patterned with alkane thiols and adsorbed fibronectin	V-sahped channels - 25 and 50 µm wide with equal spacing; depth not indicated	bovine capillary endothelial cells	cells only attached to fibronectin regions cells attached to channels or ridges, whichever possessed the alkane thiol and therefore adsorbed fibronectin
1996	Wokciak-Stothard et al. [152]	fused silica	square channels - 2 and 10 µm widths with 30 to 282 nm depths	P388D1 macrophages rat peritoneal macrophages	cells activated and spread along channels increased membrane protrusions increased F-actin and vinculin along edges of single steps or channels
1997	Rajnicek et al. [153]	quartz coated with poly-l-lysine	channels (square) - 1, 2 and 4 µm wide and 14 nm to 1.1 µm deep	embryonic Xenopus spinal cord neurons rat hippocampal neurons	Xenopus neurites grew parallel to all channels hippocampal neurons grew perpendicular to shallow, narrow channels and parallel to deep, wide channels

Table A Continued

Year	Authors	Material(s)	Topography	Cell Types(s)	Results
1997	Chehroudi et al. [154]	epoxy coated with titanium	channels (V-shaped) - 35-165 µm wide at 30,60 and 120 µm depths pits (V-shaped) - 35 to 270 µm wide and 30, 60 and 120 µm depths	rat parietal bone implant model	mineralization only on topographies bone-like foci decreased as channel depth increased more mineralization as channel depth increased bone-like foci orient on channels
1997	Rajnicek and McCaig [155]	quartz polystyrene both were coated with poly-l-lysine	channels (square) - 1, 2 and 4 µm wide and 14 nm to 1.1 µm deep	embryonic Xenopus spinal cord neurons rat hippocampal neurons	cell orientation unaffected by cytochalasin B taxol and nocodazole disrupted hippocampal microtubules but did not affect orientation alignment of neurites affected by some calcium channel, G protein, protein kinase and protein tyrosine kinase inhibitors
1998	Chou et al. [156]	titanium-coated silicon	channels (V shaped) - 6 to 10 µm repeat spacing with 3 µm depth	human gingivival fibroblasts	cells oriented along channels by 16 hrs channels altered the expression and levels of adhered matrix metalloproteinase-2 mRNA
1998	den Braber et al. [99]	silicone	channels (square) – 2, 5 and 10 µm wide and spaced with 0.5 µm depths	rat dermal fibroblasts	microfilaments and vinculin aggregates aligned with 2 µm channels only vinculin located mainly on ridges fibronectin and vinculin located in channels
1998	van Kooten et al. [157]	PDMS	channels (square) – 2, 5 and 10 µm wide with 4, 10 and 20 µm spaces and 0.5 µm depths	human skin fibroblasts	topography slowed cell entrance to s-phase of cell cycle cells proliferated less on 10 µm channels than on 2 and 5 µm channels
1999	Palmaz et al. [49]	nitinol	channels - 1, 3, 15 and 22 µm	human aortic endothelial cells	increasing channel sizes increased migration rate cells aligned and elongated with channels

Table A Continued

Year	Authors	Material(s)	Topography	Cell Types(s)	Results
1999	van Kooten and von Recum [45]	silicone coated with fibronectin (FN)	ridges - 2, 5 and 10 µm wide and spaced 4, 10 and 20 µm apart respectively with 0.5 µm heights	human skin fibroblasts human umbilical vein endothelial cells	topography influenced initial focal adhesion size and density and initial FN deposition no difference in FN networks by day 6
1999	Walboomers et al. [158]	polystyrene (PS) titanium-coated polystyrene (Ti-PS) silicone poly-L-lactic acid (PLLA) -all samples were plasma treated	channels – 1, 2, 5 and 10 µm widths and spaces with depths of 0.5 µm	rat dermal fibroblasts	PS and PLLA reproduced better than silicone or Ti-PS cell proliferation greater on PLLA and silicone surfaces alignment on PS, PLLA and silicone surfaces increased with decreased channel width cells aligned on all Ti-PS channels equally greatest alignment on 1 µm PLLA channels
1999	Walboomers et al. [46]	polystyrene	channels - 1-20 µm wide and 0.5-5.4 µm deep	rat dermal fibroblasts	orientation increased with channel depth cells follow contours of shallow and wide channels but bridge narrow and deep features
2000	Deutsch et al. [159]	silicone	pillars (rounded) - 10 µm wide and 10 to 50 µm spaced channels - 10 µm wide and spaced all were 5 µm deep	rat myocytes	myocytes attached four times as often to pillars than to smooth PDMSe cells oriented on channels
2000	Pins et al. [160]	gelatin collagen-glycosaminoglycan co-precipitate	channels 40-200 µm wide and 40 to 200 µm deep	keratinocyte	cells differentiated to form analogs of basal lamina with invaginations
2002	Petersen et al. [161]	agarose gel	pits (rectangular) - - 35x5, 35x10, 45x5, 25x5, 25x10, 55x5, 15x5, 15x10 and 55x5 µm depths were 18 to 40 µm	avian chondrocytes	cells isolated in wells more cells isolated per well as dimension increased from 15 to 25 µm cells not retained in wells >35 µm; shallower cells retained fewer cells

Table A Continued

Year	Authors	Material(s)	Topography	Cell Types(s)	Results
2002	Barbucci et al. [31]	sulfonated hyaluronic acid (HyalS) on glass	chemical stripes – 10, 25, 50 and 100 µm wide & spaced HyalS ridges in HyalS -step height 300 nm - 1 µm	HGTFN endothelial cells	decreasing stripe dimensions increases cell locomotion and orientation
2003	Dalby et al. [162]	quartz	channels - 12.5 µm wide, 2.5 µm spaced with 2 µm depth	immortalized primary human fibroblasts	cells and nuclei aligned within channels
2003	Magnani et al. [51]	hyaluronic acid (Hyal) and sulfonated hyaluronic acid (HyalS) on glass	chemical stripes – 10, 25, 50 and 100 µm;wide and spaced HyalS ridges in HyalS -step height of less than 300 nm to 1 µm	mouse fibroblasts (3T3) human primary fibroblasts bovine aortic endothelial cells human aortic endothelial cells	decreasing stripe dimensions increased cell locomotion and orientation;
2003	Scheideler et al. [163]	titanium coated silicon (channels) and epoxy replicates (ridges)	channels – 1 to 20 µm wide and 0.4 to 2 µm deep ridges - 1-20 µm wide and 0.44 to 2 µm tall	human foreskin fibroblasts keratinocytes	fibroblasts aligned to topography keratinocytes did not align on ridges 2 to 10 µm wide adsorbed fibronectin enhanced cell spreading
2003	Teixeira et al. [164]	silicon oxide deposited on silicon wafers	channels (width x space)) - 70x330, 250x550, 400x800, 650x950, 850x1150, and 1900x2100 nm with depths of 0.6 or 0.15 µm	human corneal epithelial cells	cells aligned with ridges percent aligned cells independent of lateral dimensions alignment increased with channel depth actin filaments and focal adhesions aligned
2004	Tan and Saltzman [165]	hydroxyapatite on silicon	micro - 4 µm wide and deep ridges spaced 10 µm apart and 4 µm wide and tall pillars spaced 4 µm apart; nano – randomly rough	human osteoblast-like Saos-2 and MG-63 cell lines	cells aligned parallel to ridges on both micro and micro/nano structured surfaces
2004	Wang and Ho [166]	chitosan and gelatin	channels - 10, 20, 30 and 50 µm wide and 10 or 50 µm spaced with 10 µm depth protein resisistant tri-block copolymer applied to ridges	human microvascular endothelial cells	cells restricted to channels by tri-block copolymer cell spreading decreased as channel width decreased
2005	Recknor et al. [167]	polystyrene	channels - 10 µm wide, 20 µm spaced and 3 µm deeofor astrocytes and 16 µm wide, 13 µm spaced and 4 µm deep for AHPCs	rat type-1 astrocytes adult rat hippocampal progenitor cells (AHPCs)	greater than 85% alignment of astrocytes seen on lamin coated channels AHPCs adhered and extended processes axially along channels

Table A Continued

Year	Authors	Material(s)	Topography	Cell Types(s)	Results
2005	Uttayarat et al. [50]	PDMSe	channels - 2.7 to 3.9 µm wide and 3.3 to 5.5 µm spaced with depths of 0.2, 0.5, 1.0 and 4.6 µm	Bovine aortic endothelial cells	cell elongation and alignment increased with channel depth focal adhesions formed in channels for all topographies except 4.6 µm deep cell proliferation was similar on all substrates
2005	Yang and Ou [112]	gelatin crosslinked with glutaraldehyde and bound to glass	ridges - at least 5 µm wide and at least 10 µm spaced with 1.5 µm height	human mesenchymal stem cells	cells selectively adhered to gelatin and away from glass
2006	Charest et al. [168]	polyimide	channels - 8 µm wide, 4 µm deep, 16 µm spaced chemical stripes - 10 µm wide lanes of FN spaced by 10, 20 or 100 µm wide lanes pf PEG	MC3T3-E1 osteoblast-like cells	cells aligned to both topography and chemical patterns separately when presented with both, cells align to topography rather than chemistry
2006	Pins et al. [169]	glass treated with organosilane and printed with fibronectin (FN), fibrinogen (FG) and bovine serum albumin (BSA)	chemical stripes - 600 nm wide and either 10 or 40 µm spaced and 20 µm long	human dermal fibroblasts	cells on FN and FG patterns had greater tendency to spread across adjacent structures than on BSA patterns
2006	Yu et al. [170]	chitosan-collagen-gelatin blend	channels – 200 and 500 µm wide and spaced with 80 µm depth and 10, 20 and 50 µm wide and spaced with 20 µm depth	human mesenchymal stem cells	cells on 200 µm channels initially adhered in channels and later migrated to ridges cells oriented parallel to the 200 µm channels topographies smaller than cells hindered proliferation
2006	Teixeira et al. [171]	silicon	channels (width x space)) - 70x330, 250x550, 400x800, 650x950, 850x1150, and 1900x2100 nm 600 nm depth for all features	primary human corneal epithelial cells	cell alignment switched from perpendicular to parallel when pitch increased from 400 to 4000nm between 800 and 1600nm pitches both parallel and perpendicular alignment is observed

APPENDIX B
CALCULATION OF SHEAR IN PARALLEL PLATE FLOW

The following is the calculation of shear stress at the plate for pressure flow through two parallel plates. The important chamber dimensions are the width (w) of the plats and height (h) of the separation (Fig. B). The calculation assumes laminar, fully developed flow with h<<w.

Start with the equation of continuity assuming constant density as shown below:

$$\frac{\partial v_x}{\partial x} + \frac{\partial v_y}{\partial y} + \frac{\partial v_z}{\partial z} = 0 . \tag{B-1}$$

In this equation, v_i refers to flow in the i-direction. Under fully developed flow, fluid movement only occurs in the x direction which gives rise to the following:

$$v_y = v_z = 0 \text{ and } \frac{\partial v_y}{\partial y} = \frac{\partial v_z}{\partial z} = 0 . \tag{B-2}$$

Substituting these into Equation B-1 gives the following:

$$\frac{\partial v_x}{\partial x} = 0 . \tag{B-3}$$

Now apply the Navier-Stokes equation for the x-component as given below where p refers to pressure and g refers to the gravitational force:

$$\rho\left(\frac{\partial v_x}{\partial t} + v_x \frac{\partial v_x}{\partial x} + v_y \frac{\partial v_x}{\partial y} + v_z \frac{\partial v_x}{\partial z} \right) = \mu\left(\frac{\partial^2 v_x}{\partial x^2} + \frac{\partial^2 v_x}{\partial y^2} + \frac{\partial^2 v_x}{\partial z^2} \right) - \frac{\partial p}{\partial x} + \rho g_x \tag{B-4}$$

Assume steady-state flow so that the following holds true:

$$\frac{\partial v_x}{\partial t} = 0 . \tag{B-5}$$

For the case of the chamber height being much smaller than the chamber width, flow does not vary in the z-direction so that the following holds true:

$$\frac{\partial v_x}{\partial z} = \frac{\partial^2 v_x}{\partial z^2} = 0 . \tag{B-6}$$

Substituting this into Equation B-4 gives the following:

$$0 = \mu\left(\frac{\partial^2 v_x}{\partial y^2}\right) - \frac{\partial p}{\partial x} + \rho g_x . \tag{B-7}$$

Because flow direction is perpendicular to gravitational force, g_x=0 and Equation B-7 becomes:

$$\frac{\partial p}{\partial x} = \mu\left(\frac{\partial^2 v_x}{\partial y^2}\right). \tag{B-8}$$

Because velocity is zero in all directions except x (Equation B-2) and velocity in the x-direction is independent of x (Equation B-3), solution of Navier-Stokes equations for y and z components proves the following:

$$\frac{\partial p}{\partial y} = \frac{\partial p}{\partial z} = 0 . \tag{B-9}$$

Therefore, pressure is only a function of x (or a constant). Equations B-3, B-5 and B-6 indicate that v_x is only a function of y (or a constant). In order for Equation B-8 to be true, the derivative of P with respect to x must be equal to a constant as shown below:

$$\frac{\partial p}{\partial x} = C_1 . \tag{B-10}$$

$$\frac{\partial^2 v_x}{\partial y^2} = \frac{1}{\mu}\frac{\partial p}{\partial x} = C_2 . \tag{B-11}$$

Integrating Equation B-11 once gives

$$\frac{\partial v_x}{\partial y} = \left(\frac{1}{\mu}\frac{\partial p}{\partial x}\right) y + C_3 . \tag{B-12}$$

Application of the following boundary condition based on symmetry in the y-direction to Equation B-12

$$\left.\frac{\partial v_x}{\partial y}\right|_{y=0} = 0 \tag{B-13}$$

gives the equation below:

$$\frac{\partial v_x}{\partial y} = \left(\frac{1}{\mu}\frac{\partial p}{\partial x}\right) y \,. \tag{B-14}$$

Integration of Equation B-14 results in the following:

$$v_x = \left(\frac{1}{2\mu}\frac{\partial p}{\partial x}\right) y^2 + C_3 \,. \tag{B-15}$$

Apply the boundary condition that velocity at the plate (y=0.5h) is zero to Equation B-15 to get the equation below:

$$v_x = \left(\frac{1}{2\mu}\frac{\partial p}{\partial x}\right)\left[y^2 - \left(\frac{h}{2}\right)^2\right]. \tag{B-16}$$

Based on symmetry, the maximum velocity occurs at y=0 which gives the following:

$$v_{x\max} = -\frac{1}{2\mu}\frac{\partial p}{\partial x}\left(\frac{h}{2}\right)^2 \tag{B-17}$$

and

$$v_x = v_{x\max}\left[1 - \left(\frac{2y}{h}\right)^2\right]. \tag{B-18}$$

Shear stress of a Newtonian fluid is given by the following:

$$\tau_{yx} = -\mu\frac{\partial v_x}{\partial y} \,. \tag{B-19}$$

Substitution of Equation B-18 into Equation B-19 and derivation gives the equation below:

$$\tau_{yx} = 8\mu v_{x\max}\frac{y}{h^2} \,. \tag{B-20}$$

Shear stress at the plate becomes the following:

$$\tau_{yx}\Big|_{y=0.5h} = 4\frac{\mu v_{x\max}}{h}. \tag{B-21}$$

The flowrate (Q) through the parallel plate chamber is the average velocity (<vx>) multiplied by the cross-sectional area as shown below:

$$Q = \langle v_x \rangle hw. \tag{B-22}$$

The average velocity can be calculated by integrating Equation B-18 and dividing by the chamber height as shown in the following equation:

$$\langle v_x \rangle = \frac{\int_{-0.5h}^{0.5h} v_{x\max}\left[1-\left(\frac{2y}{h}\right)^2\right]dy}{h} = \frac{2}{3}v_{x\max}. \tag{B-23}$$

Substitution of Equation B-23 into Equation B-22 gives the following:

$$Q = \left(\frac{2}{3}v_{x\max}\right)hw. \tag{B-24}$$

Rearranging yields the equation below

$$v_{x\max} = \frac{3Q}{2hw}. \tag{B-25}$$

Substitution into Equation B-21 gives the final equation of shear stress in terms of the volumetric flowrate and chamber dimensions as shown below:

$$\tau_{yx}\Big|_{y=0.5h} = \frac{6\mu Q}{h^2 w}. \tag{B-26}$$

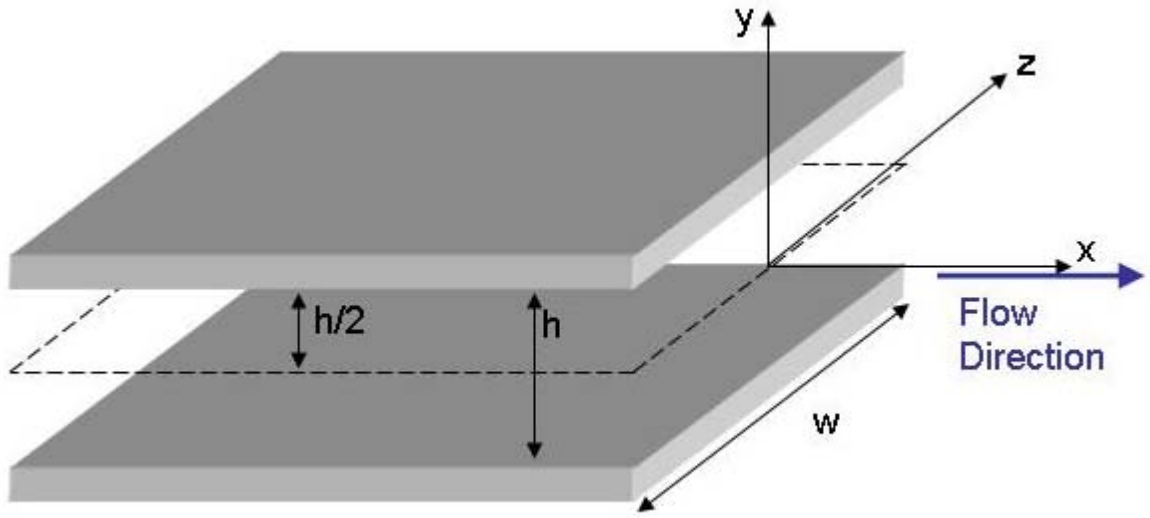

Figure B. Diagram of flow between parallel plates.

LIST OF REFERENCES

[1] Hoyert D, Heron M, Murphy S, Kung H. Deaths: final data for 2003. National Vital Statistics Reports 2006; 54(13)

[2] Dardik A, Liu A, Ballermann BJ. Chronic *in vitro* shear stress stimulates endothelial cell retention on prosthetic vascular grafts and reduces subsequent i*n vivo* neointimal thickness. Journal of Vascular Surgery 1999; 29(1):157-67.

[3] Ott MJ, Ballermann BJ. Shear stress-conditioned, endothelial cell-seeded vascular grafts improved cell adherence in response to *in vitro* shear stress. Surgery 1995; 117(3):334-9.

[4] Weiss P. Experiments on cell and axon orientation *in vitro*: the role of colloidal exudates in tissue organization. The Journal of Experimental Zoology 1945; 100:353-85.

[5] Lin F-H, Yao C-H, Sun J-S, Liu H-C, Huang C-W. Biological effects and cytotoxicity of the composite composed by tricalcium phosphate and glutaraldehyde cross-linked gelatin. Biomaterials 1998; 19(10):905-17.

[6] Teebken OE, Pichlmaier AM, Haverish A. Cell seeded decellularized allogenic matrix grafts and biodegradeable polydioxanone-prostheses compared with arterial autografts in a porcine model. European Journal of Vascular Endovascular Surgery 2001; 22:139-45.

[7] Muller-Hulsbeck S, Walluscheck KP, Priebe M, Grimm J, Cremer J, Heller M. Experience on endothelial cell adhesion on vascular stents and stent-grafts. Investigative Radiology 2002; 37(6):314-20.

[8] Birchall IE, Lee VWK, Ketharanathan V. Retention of endothelium on ovine collagen biomatrix vascular conduits under physiological shear stress. Biomaterials 2001; 22(23):3139-44.

[9] Birchall IE, Field PL, Ketharanathan V. Adherence of human saphenous vein endothelial cell monolayers to tissue-engineered biomatrix vascular conduits. Journal of Biomedical Materials Research 2001; 56(3):437-43.

[10] Fernandez P, Bareille R, Conrad V, Midy D, Bordenave L. Evaluation of an *in vitro* endothelialized vascular graft under pulsatile shear stress with a novel radiolabeling procedure. Biomaterials 2001; 22(7):649-58.

[11] Salacinski HJ, Tai NR, Punshon G, Giudiceandrea A, Hamilton G, Seifalian AM. Optimal endothelialisation of a new compliant poly(carbonate-urea)urethane vascular graft with effect of physiological shear stress. European Journal of Vascular and Endovascular Surgery 2000; 20(4):342-52.

[12] Dunkern TR, Paulitschke M, Meyer R, Buttemeyer R, Hetzer R, Burmester G, Sittinger M. A novel perfusion system for the endothelialisation of PTFE grafts under defined flow. European Journal of Vascular and Endovascular Surgery 1999; 18(2):105-10.

[13] Tiwari A, Kidane A, Salacinski H, Punshon G, Hamilton G, Seifalian AM. Improving endothelial cell retention for single stage seeding of prosthetic grafts: Use of polymer sequences of arginine-glycine-aspartate. European Journal of Vascular and Endovascular Surgery 2003; 25(4):325-9.

[14] Gourevitch D, Jones CE, Crocker J, Goldman M. Endothelial cell adhesion to vascular prosthetic surfaces. Biomaterials 1988; 9(1):97-100.

[15] Walluscheck KP, Steinhoff G, Kelm S, Haverish A. Improved endothelial cell attachmenton ePTFE vascular grafts pretreated with synthetic RGD-containing peptides. European Journal of Vascular and Endovascular Surgery 1996; 12:321-30.

[16] Schneider PA, Hanson SR, Price TM, Harker LA. Performed confluent endothelial cell monolayers prevent early platelet deposition on vascular prostheses in baboons. Journal of Vascular Surgery 1988; 8:229-35.

[17] Allen BT, Long JA, Clark RE, Sicared GA, Hopkins KT, Welch MJ. Influence of endothelial cell seeding on platelet deposition and patency in small-diamter Dacron arterial grafts. Journal of Vascular Surgery 1984; 1984:224-33.

[18] Kadletz M, Magometschnigg H, Minar E, Konig G, Grabenwoger M, Grimm M, Wolner E. Implantation of *in vitro* endothelialized polytetraethylene grafts in human beings: A preliminary report. Journal of Thoracic and Cardiovascular Surgery 1992; 104(3):736-42.

[19] Magometschnigg H, Kadletz M, Vodrazka M, Duck W, Grimm M, Grabenwoger M, Minar E, Staudacher M, Fenzel G, Wolner E. Prospective study with *in vitro* endothelial cell lining of expanded polytetraethylene grafts in crural repeat reconstruction. Journal of Vascular Surgery 1992; 15(3):527-35.

[20] Laube HR, Duwe J, Rutsch W, Konertz W. Clinical experience with autologous endothelial cell-seeded polytetrafluoroethylene coronary artery bypass grafts. Journal of Thoracic and Cardiovascular Surgery 2000; 120(1):134-41.

[21] Graham LM, Burkel WE, Ford JW, Vinter DW, Kahn RH, Stanley JC. Immediate seeding of enzymatically derived endothelialium in Dacron Vascular grafts. Archives of Surgery 1980; 115:1289-94.

[22] Herring M, Gardner A, Glover J. A single-staged technique for seeding vascular grafts with autogenous endothelium. Surgery 1978; 84:498-504.

[23] Ortenwall P, Wadenvik H, Kutti J, Risberg B. Endothelial cell seeding reduces thrombogenicity of Dacron grafts inhumans. Journal of Vascular Surgery 1990; 11(403-410)

[24] Rademacher A, Paulitschke M, Meyer R, Hetzer R. Endothelialization of PTFE vascular grafts under flow induces significant cell changes. The International Journal of Artificial Organs 2001; 24(4):235-42.

[25] Rosenman JE, Pearce WH, Silberstein EB, Kempczinski RF. Kinetics of endothelial seeding. Journal of Vascular Surgery 1985; 2:778-84.

[26] Walluscheck KP, Steinhoff G, Haverich A. Endothelial cell seeding of de-endothelialized human arteries: improvement in adhesion molecule induction and flow-seeding technology. European Journal of Vascular and Endovascular Surgery 1996; 12:46-53.

[27] Salacinski HJ, Tiwari A, Hamilton G, Seifalian AM. Cellular engineering of vascular bypass grafts: role of chemical coatings for enhancing endothelial cell attachment. Medical & Biological Engineering & Computing 2001; 39(6):609-18.

[28] Zhu Y, Gao C, He T, Shen J. Endothelium regeneration on luminal surface of polyurethane vascular scaffold modified with diamine and covalently grafted with gelatin. Biomaterials 2004; 25(3):423-30.

[29] Hsu S, Tseng H, Wu M. Comparative *in vitro* evaluation of two different preparations of small diameter polyurethane vascular grafts. Artificial Organs 2000; 24(2):119-28.

[30] Chan BP, Bhat VD, Yegnasubramanian S, Reichert WM, Truskey GA. An equilibrium model of endothelial cell adhesion via integrin-dependent and integrin-independent ligands. Biomaterials 1999; 20(23-24):2395-403.

[31] Barbucci R, Lamponi S, Magnani A, Pasqui D. Micropatterned surfaces for the control of endothelial cell behaviour. Biomolecular Engineering 2002; 19(2-6):161-70.

[32] Hsu SH, Sun SH, Check DC. Improved retention of enothelial cells seeded on polyurethane small-diameter vascular grafts modified by a recombinant RGD-containing protein. Artificial Organs 2003; 27(12):1068-78.

[33] Seifalian AM, Tiwari A, Hamilton G, Salacinski HJ. Improving the clinical patency of prosthetic vascular and coronary bypass grafts: The role of seeding and tissue engineering. Artificial Organs 2002; 26(4):307-20.

[34] Kempczinski RF, Ramalanjaona GH, Douville C, Silberstein EB. Thrombogenicity of a fibronectin-coated experimental polytetrafluoroethylene graft. Surgery 1987; 101:439-44.

[35] Wong AJ, Pollard TD, Herman IM. Actin filament stress fibers in vascular endothelial cells *in vivo*. Science 1983; 219(4586):867-9.

[36] Franke R-P, Grafe M, Shchnittler H, Seiflge D, Mittermayer C. Induction of human vascular endothelial fibres by fluid shear stress. Nature 1984; 307(16):648-9.

[37] Sato M, Nagayama K, Kataoka N, Sasaki M, Hane K. Local mechanical properties measured by atomic force microscopy for cultured bovine endothelial cells exposed to shear stress. Journal of Biomechanics 2000; 33(1):127-35.

[38] Davies PF, Robotewskyj A, Griem ML. Quantitative studies of endothelial cell adhesion: direction remodeling of focal adhesion sites in response to flow forces. Journal of Clinical Investigation 1994; 93(5):2031-8.

[39] Wechezak AR, Wight TN, Viggers RJ, Sauvage LR. Endothelial adherence under shear stress is dependent upon microfilament reorganization. Journal of Cellular Physiology 1989; 139:136-46.

[40] Ballermann BJ, Dardik A, Eng E, Liu A. Shear stress and the endothelium. Kidney International 1998; 54(Suppl. 67):S-100 - S-8.

[41] Harrison RG. The reaction of embryonic cells to solid structures. The Journal of Experimental Zoology 1914; 17(4):521-44.

[42] Clark P, Connolly P, Curtis ASG, Dow JAT, Wilkinson CDW. Topographical control of cell behoviour: II. Multiple grooved substrata. Development 1990; 108:635-44.

[43] Campbell CE, von Recum AF. Microtopography and soft tissue response. Journal of Investigative Surgery 1989; 2:51-74.

[44] Schmidt JA, von Recum AF. Texturing of polymer surfaces at the cellular level. Biomaterials 1991; 12(4):385-9.

[45] van Kooten TG, von Recum AF. Cell adhesion to textured silicone surfaces: The influence of time of adhesion and texture on focal contact and fibronectin fibril formation. Tissue Engineering 1999; 5(3):223-40.

[46] Walboomers XF, Monaghan W, Curtis AS, J.A. J. Attachment of fibroblasts on smooth and microgrooved polystyrene. Journal of Biomedical Materials Research 1999; 46(2):212-20.

[47] Matsuda T, Sugawara T. Control of cell adhesion, migration, and orientation on photochemically microprocessed surfaces. Journal of Biomedical Materials Research 1996; 32(2):165-73.

[48] Mrksich M, Chen CS, Xia YN, Dike LE, Ingber DE, Whitesides GM. Controlling cell attachment on contoured surfaces with self-assembled monolayers of alkanethiolates on gold. Proceedings of the National Academy of Sciences of the United States of America 1996; 93(20):10775-8.

[49] Palmaz JC, Benson A, Sprague EA. Influence of surface topography on endothelialization of intravascular metallic material. Journal of Vascular and Interventional Radiology 1999; 10(4):439-44.

[50] Uttayarat P, Toworfe GK, Dietrich F, Lelkes PI, Composto RJ. Topographic guidance of endothelial cells on silicone surfaces with micro- to nanogrooves: Orientation of actin filaments and focal adhesions. Journal of Biomedical Materials Research Part A 2005; 75A(3):668-80.

[51] Magnani A, Priamo A, Pasqui D, Barbucci R. Cell behaviour on chemically microstructured surfaces. Materials Science and Engineering: C 2003; 23(3):315-28.

[52] Wilkerson WR. Contribution of modulus to the contact guidance of endothelial cells on microtextured siloxane elastomers. M.S., University of Florida, 2001.

[53] Feinberg AW, Wilkerson W, Seegert C, Gibson A, Hoipkemeier-Wilson L, Brennan A. Systematic variation of microtopography, surface chemistry and elastic modulus and the state dependent effect on endothelial cell alignment. Journal of Biomedical Materials Research Part A 2007; SUBMITTED

[54] Feinberg AW. Endothelial cell response to microengineered surfaces analyzed by fluorescent and atom force microscopy. PhD Fissertation, University of Florida, Department of Biomedical Engineering, 2004.

[55] Young T. An essay on the cohesion of fluids. Philosophical Transactions of the Royal Society of London 1805; 95:65-87.

[56] Johnson RE, Jr., Dettre RH. Wettability and contact angles. Surface and Colloid Science 1969; 2:85-153.

[57] Marmur A. Wetting on hydrophobic rough surfaces: to be heterogeneous or not to be? Langmuir 2003; 19(20):8343-8.

[58] Chen W, Fadeev AY, Hsieh MC, Oner D, Youngblood J, McCarthy TJ. Ultrahydrophobic and ultrahydrophilic surfaces: some comments and examples. Langmuir 1999; 15:3395-9.

[59] Wenzel RN. Resistance of solid surfaces to wetting by water. Industrial and Engineering Chemistry 1936; 28:988-94.

[60] Cassie ABD, Baxter S. Wettability of porous surfaces. Faraday Society Transactions 1944; 40:546-51.

[61] Bico J, Thiele U, Quere D. Wetting of textured surfaces. Colloids and Surfaces A: Physicochemical and Engineering Aspects 2002; 206(1-3):41-6.

[62] Carman ML, Estes TG, Feinberg AW, Schumacher JF, Wilkerson W, Wilson LH, Callow ME, Callow JA, Brennan AB. Engineered antifouling microtopographies – correlating wettability with cell attachment. Biofouling 2006; 22(1):11-21.

[63] Walboomers XF, Jansen JA. Cell and tissue behavior on micro-grooved surfaces. Odontology 2001; 89:2-11.

[64] Curtis A, Wilkinson C. Review: Topographical control of cells. Biomaterials 1997; 18:1673-563.

[65] Singhvi R, Stephanopoulos G, Wang DIC. Review: Effects of substratum morphology on cell physiology. Biotechnology and Bioengineering 1994; 43:764-71.

[66] Wilkinson CDW, Riehle M, Wood M, Gallagher J, Curtis ASG. The use of materials patterned on a nano- and micro-metric scale in cellular engineering. Materials Science and Engineering C 2002; 19:263-9.

[67] Arnold M, Cavalcanti-Adam EA, Glass R, Blummel J, Eck W, Kantlehner M, Kessler H, Spatz JP. Activation of integrin function by nanopatterned adhesive interfaces. Chemphyschem 2004; 5(3):383-8.

[68] Callow ME, Jennings AR, Brennan AB, Seegert CA, A. G, Wilson L, Feinberg A, Baney R, Callow JA. Microtopographic cues for settlement of zoospores of the green fouling alga *Enteromorpha*. Biofouling 2002; 18(3):237-45.

[69] Hoipkemeier-Wilson L, Schumacher JF, Carman ML, Gibson AL, Feinberg AW, Callow ME, Finlay JA, Brennan AB. Antifouling potential of lubricious, micro-engineered, PDMS elastomers against zoospores of the green fouling alga *Ulva*. Biofouling 2004; 20(1):53-63.

[70] Berntsson KM, Jonsson PR, Lejhall M, Gatenholm P. Analysis of behavioural rejection of micro-textured surfaces and implications for recruitment by the barnacle *Balanus improvisus*. Journal of Experimental Marine Biology and Ecology 2000; 251:59-83.

[71] Scheuerman TR, Camper AK, Hamilton MA. Effects of substratum topography on bacterial adhesion. Journal of Colloid and Interface Science 1998; 208(1):23-33.

[72] Marmur A. Thermodynamic aspects of contact angle hysteresis. Advances in Colloid and Interface Sciences 1994; 50:121-41.

[73] Bico J, Marzolin C, Quere D. Pearl drops. Europhysics Letters 1999; 47(2):220-6.

[74] Bico J, Tordeux C, Quere D. Rough wetting. Europhysics Letters 2001; 55(2):214-20.

[75] Quere D. Rough ideas on wetting. Physica A: Statistical and Theoretical Physics 2002; 313:32-46.

[76] Callow ME. Fouling algae from "in-service' ships. Botanica Marina 1986; 24:351-7.

[77] Pettitt ME, Henry SL, Callow ME, Callow JA, Clare AS. Activity of commerncial enzymes on the settlement and adhesion of cypris larvae of the barnacle *Balanus amphitrite*, spores of the green alga *Ulva linza* and the diatom *Navicula perminuta*. Biofouling 2004; 20:299-311.

[78] Chaudhury MK, Finlay JA, Chung JY, Callow ME, Callow JA. The influence of elastic modulus on the soft fouling alga *Ulva linza* (*Enteromorpha linza*) from polydimethyl siloxane (PDMS) ideal networks. Biofouling 2005; 21:41-8.

[79] Callow M, Callow J, Pickett-Heaps J, Wetherbee R. Primary adhesion of *Enteromorpha* (*Chlorophyta, Ulvales*) propagules: quantitative settlement studies and video microscopy. Journal of Phycology 1997; 33(6):938-47.

[80] Callow JA, Callow ME, Ista LK, Lopez G, Chaudhury MK. The influence of surface energy on the wetting behaviour of the spore adhesive of the marine alga *Ulva linza* (syn. *Enteromorpha linza*). Journal of the Royal Society Interface 2005; 2(4):319-25.

[81] Gray BL, Lieu DK, Collins SD, Smith RL, Barakat IL. Microchannel platform for the study of endothelial cell shape and function. Biomedical Microdevices 2002; 4(1):9-16.

[82] Buttiglieri S, Pasqui D, Migliori M, Johnstone H, Affrossman S, Sereni L, Wratten ML, Barbucci R, Tetta C, Camussi G. Endothelization and adherence of leucocytes to nanostructured surfaces. Biomaterials 2003; 24(16):2731-8.

[83] Riehle M, Ferris D, Hamilton D, Curtis A. Cell behavior in tubes. Experimental Biology Online 1998; 3(2)

[84] Dalby MJ, Riehle MO, Johnstone H, Affrossman S, Curtis ASG. *In vitro* reaction of endothelial cells to polymer demixed nanotopography. Biomaterials 2002; 23:2945-54.

[85] Zhang J, Patel JM, Block ER. Molecular cloning, characterization and expression of a nitric oxide synthase from porcine pulmonary artery endothelial cells. Comparative Biochemistry and Physiology Part B: Biochemistry and Molecular Biology 1997; 116(4):485-91.

[86] Karges HE, Funk KA, Ronneberger H. Activity of coagulation and fibrinolysis parameters in animals. Arzneimittelforsching/Drug Research 1994; 44(6):793-7.

[87] Gross DR. Thromboembolic phenoena and the use of the pig as an appropriate animal for research on cardiovascular devices. International Journal of Artificial Organs 1997; 20(4):195-203.

[88] Feinberg AW, Gibson AL, Wilkerson WR, Seegert CA, Wilson LH, Zhao LC, Baney RH, Callow JA, Callow ME, Brennan AB. Investigating the energetics of bioadhesion on microengineered siloxane elastomers: Characterizing the topography, mechanical properties, and surface energy and their effect on cell contact guidance. In: Clarson SJ, Fitzgerald JJ, Owen MJ, Smith SDVan Dyke ME, editors. Sythesis and Properties of Silicones and Silicone-Modified Materials. ACS, 2003. p. 196-211

[89] Ostuni E, Chen CS, Ingber DE, Whitesides GM. Selective deposition of proteins and cells in arrays of microwells. Langmuir 2001; 17(9):2828-34.

[90] Ward CA, Stanga D, Zdasink BJ, Gates FL. Effect of air nuclei on the adsorption of fibrinogen to silicone rubber. Annals of Biomedical Engineering 1979; 7:451-69.

[91] Patel JM, Edwards DA, Block ER, Raizada MK. Effect of nitrogen-dioxide on surface-membrane fluidity and insulin-receptor binding of pulmonary endothelial-cells. Biochemical Pharmacology 1988; 37(8):1497-507.

[92] Dunn GA, Heath JP. A new hypothesis of contact guidance in tissue cells. Experimental Cell Research 1976; 101:1-14.

[93] Finlay JA, Callow ME, Ista LK, Lopez GP, Callow JA. The influence of surface wettability on the adhesion strength of settled spores of the green alga *Enteromorpha* and the diatom *Amphora*. Integr. Comp. Biol. 2002; 42:1116-22.

[94] Kaelble DH, Moacanin J. A surface energy analysis of bioadhesion. Polymer 1977; 18:475-82.

[95] Dexter SC. Influence of substrate wettability on the formation of bacterial slime films on solid surfaces immersed in natural sea water. International Congress on marine Corrosion and Fouling 1976; 4:137-44.

[96] Baier RE, Meyer AE, Natiella JR, Natiella RR, Carter JM. Surface properties determine bioadhesive outcomes: methods and results. Journal of Biomedical Materials Research 1984; 18:337-55.

[97] Baier RE. On adhesion of biological substances to low energy solid surfaces. Journal of Colloid and Interface Science 1982; 88(1):296-7.

[98] den Braber ET, de Ruijter JE, Smits HTJ, Ginsel LA, von Recum AF, Jansen JA. Quantitative analysis of cell proliferation and oritentation on substrata with uniform parallel surface micro-grooves. Biomaterials 1996; 17:1093-9.

[99] den Braber ET, de Ruijter JE, Ginsel LA, von Recum AF, Jansen JA. Orientation of ECM protein deposition, fibrblast cytoskeleton, and attachment complex components on silicone microgrooved surfaces. Journal of Biomedical Materials Research 1998; 40(2):291-300.

[100] Wilson LH, Schumacher JF, Finlay JA, Perry R, Callow ME, Callow JA, Brennan AB. Towards minimally fouling substrates: Surface grafting and topography. Polymer Preprints 2005; 46(2):1312-3.

[101] Wilson LH. Bioresponse to polymeric substrates: effect of surface energy, modulus, topography, and surface graft copolymers. Ph.D. University of Florida, Materials Science and Engineering, 2005.

[102] Qian P-Y, Rittschof D, Sreedhar B. Macrofouling in unidirectional flow: miniature pipes as experimental models for studying the interaction of flow and surface characteristics on the attachment of barnacle, bryozoan and polychaete larvae. Marine Ecology progress Series 2000; 207:109-21.

[103] Ross-Murphy SB. Structure and rheology of gelatin gels: reent progress. Polymer 1991; 33(12):2622-7.

[104] Scott G, editor, Degradable Polymers - Principles and Applications 2nd ed. Dordrecht, The Netherlands: Kluwer Acadmeic Publishers, 2002.

[105] Wess TJ, Orgel JP. Changes in collagen structure: drying, dehydrothermal treatment and relation to long term deterioration. Thermochimica Acta 2000; 365(1-2):119-28.

[106] Koide M, Osaki K, Konishi J, al. e. A new type of biomaterial for artificial skin: dehydrothermally crosslinked composites of fibrillar and denatured collagens. Journal of Biomedical Materials Research 1993; 27(1):79-87.

[107] Weadock KS, Miller EJ, Bellincampi LD, Zawadsky JP, Dunn MG. Physical crosslinking of collagen fibers: Comparison ultraviolet irradiation and dehydrothermal treatment Journal of Biomedical Materials Research 1995; 29:1373-9.

[108] Butler MF, Ng YF, Pudney PDA. Mechanism and kinetics of the crosslinking reaction between biopolymers containing primary amine groups and genipin. Journal of Polymer Science Part A - Polymer Chemistry 2003; 41(24):3941-53.

[109] Liang HC, Chang WH, Lin KJ, Sung HW. Genipin-crosslinked gelatin microspheres as a drug carrier for intramuscular administration: In vitro and in vivo studies. Journal of Biomedical Materials Research Part A 2003; 65A(2):271-82.

[110] Lynn L. H. Huang H-WSC-CTD-MH. Biocompatibility study of a biological tissue fixed with a naturally occurring crosslinking reagent. Journal of Biomedical Materials Research 1998; 42(4):568-76.

[111] Chang Y, Hsu C-K, Wei H-J, Chen S-C, Liang H-C, Lai P-H, Sung H-W. Cell-free xenogenic vascular grafts fixed with glutaraldehyde or genipin: In vitro and in vivo studies. Journal of Biotechnology 2005; 120(2):207-19.

[112] Yang LJ, Ou YC. The micro patterning of glutaraldehyde (GA)-crosslinked gelatin and its application to cell-culture. Lab on a Chip 2005; 5(9):979-84.

[113] Cuevas BJ. Synthesis and properties of protein micro/mesosphere-drug compositions designed for intratumoral cancer therapy. Ph.D. Dissertation, University of Florida, Materials Science and Engineering, 2003.

[114] Bajpai AK, Shrivastava M. Dynamic swelling behavior of polyacrylamide based three component hydrogels. Journal of Macromolecular Science. Pure and Applied Chemistry 2000; A37(9):1069-88.

[115] Lee JH, Macosko CW, Urry DW. Swelling behavior of gamma-irradiation cross-linked elastomeric polypentapeptide-based hydrogels. Macromolecules 2001; 34:4114-23.

[116] Rathna GVN, Chaaterji PR. Swelling kinetics and mechanistic aspects of thermosensitive interpenetrating polymer networks. Journal of Macromolecular Science. Pure and Applied Chemistry 2001; A38(1):43-56.

[117] Matsuda S, Iwata H, Se N, Ikada Y. Bioadhesion of gelatin films crosslinked with glutaraldehyde. Journal of Biomedical Materials Research 1999; 45(1):20-7.

[118] Liang H-C, Chang W-H, Liang H-F, Lee M-H, Sung H-W. Crosslinking structures of gelatin hydrogels crosslinked with genipin or a water-soluble carbodiimide. Journal of Applied Polymer Science 2004; 91:4017-26.

[119] Frame MD, Sarelius IH. Flow-induced cytoskeletal changes in endothelial cells growing on curved surfaces. Microcirculation (New York, N.Y.: 1994) 2000; 7(1):419-27.

[120] Sirois E, Charara J, Ruel J, Dussault JC, Gagnon P, Doillon CJ. Endothelial cells exposed to erythrocytes under shear stress: An in vitro study. Biomaterials 1998; 19(21):1925-34.

[121] Taite LJ, Rowland WL, Ruffino KA, Smith BRE, Lawrence MB, West JL. Bioactive hydrogel substrates: Probing leukocyte receptor-ligand interactions in parallel plate flow chamber studies. Annals of Biomedical Engineering 2006; 34(1):1705-11.

[122] Schumacher JF, Carman ML, Estes TG, Feinberg AW, Wilson LH, Callow ME, Callow JA, FInlay JA, .Brennan AB. Engineered anitfouling microtopographies - Effect of feature size, geometry, and roughness on settlement of zoospores of the green alga *Ulva*. Biofouling 2007; 23(1):55-62.

[123] Toborek M, Kaiser S. Endothelial cell functions. Relationship to atherogenesis. Basic Research in Cardiology 1999; 94(5):295-314.

[124] Kubes P, Suzuki M, Granger DN. Nitric oxide: an endogenous modulator of leukocyte adhesion. PNAS 1991; 88(11):4651-5.

[125] Harrison RG. On the stereotropism of embryonic cells. Science 1911; 34(870):279-81.

[126] Ohara PT, Buck RC. Contact guidance in vitro - light, transmission, and scanning electron-microscopic study. Experimental Cell Research 1979; 121(2):235-49.

[127] Wilkinson PC, Shields JM, Haston WS. Contact guidance of human neutrophil leukocytes. Experimental Cell Research 1982; 140(1):55-62.

[128] Brunette DM, Kenner GS, Gould TRL. Grooved titanium surfaces orient growth and migration of cells from human gingival explants. Journal of Dental Research 1983; 62(10):1045-8.

[129] Brunette DM. Spreading and orientation of epithelial-cells on grooved substrata. Experimental Cell Research 1986; 167(1):203-17.

[130] Dunn GA, Brown AF. Alignment of fibroblasts on grooved surfaces described by a simple geometric transformation. Journal of Cell Science 1986; 83:313-40.

[131] Brunette DM. Fibroblasts on micromachined substrata orient hierarchically to grooves of different dimensions. Experimental Cell Research 1986; 164(1):11-26.

[132] Clark P, Connolly P, Curtis ASG, Dow JAT, Wilkinson CDW. Topographical control of cell behavior: I. Simple step cues. Development 1987; 99(3):439-48.

[133] Chehroudi B, Gould TR, Brunette DM. Effects of a grooved epoxy substratum on epithelial-cell behavior invitro and invivo. Journal of Biomedical Materials Research 1988; 22(6):459-73.

[134] Wood A. Contact guidance on microfabricated ubstrata - the response of teleost fin mesenchyme cells to repeating topographical patternss. Journal of Cell Science 1988; 90:667-81.

[135] Chehroudi B, Gould TRL, Brunette DM. Titanium-coated micromachined grooves of different dimensions affect epithelial and connective-tissue cells differently invivo. Journal of Biomedical Materials Research 1990; 24(9):1203-19.

[136] Clark P, Connolly P, Curtis ASG, Dow JAT, Wilkinson CDW. Cell guidance by ultrafine topography *in vitro*. Journal of Cell Science 1991; 99:73-7.

[137] Clark P, Britland S, Connolly P. Growth cone guidance and neuron morphology on micropatterned laminin surfaces. Journal of Cell Science 1993; 105:203-12.

[138] Meyle J, Wolburg H, von Recum AF. Surface micromorpholgy and cellular interactions. Journal of Biomaterials Applications 1993; 7:362-74.

[139] Meyle J, Gultig K, Wolburg H, Vonrecum AF. Fibroblast anchorage to microtextured surfaces. Journal of Biomedical Materials Research 1993; 27(12):1553-7.

[140] Oakley C, Brunette DM. The sequence of alignment of microtubules, focal contacts and actin-filaments in fibroblasts spreading on smooth and grooved titanium substrata. Journal of Cell Science 1993; 106:343-54.

[141] Meyle J, Gultig K, Brich M, Hammerle H, Nisch W. Contact guidance of fibroblasts on biomaterial surfaces. Journal of Materials Science-Materials in Medicine 1994; 5(6-7):463-6.

[142] Webb A, Clark P, Skepper J, Compston A, Wood A. Guidance of oligodendrocytes and their progenitors by substratum topography. Journal of Cell Science 1995; 108:2747-60.

[143] Chesmel KD, Black J. Cellular-responses to chemical and morphologic aspects of biomaterial surfaces .1. a novel in-vitro model system. Journal of Biomedical Materials Research 1995; 29(9):1089-99.

[144] Chou LS, Firth JD, Uitto VJ, Brunette DM. Substratum surface-topography alters cell-shape and regulates fibronectin messenger-RNA level, messenger-RNA stability, secretion and assembly in human fibroblasts. Journal of Cell Science 1995; 108:1563-73.

[145] den Braber ET, Deruijter JE, Smits HTJ, Ginsel LA, Vonrecum AF, Jansen JA. Effect of parallel aurface microgrooves and surface-energy on cell-growth. Journal of Biomedical Materials Research 1995; 29(4):511-8.

[146] Meyle J, Gultig K, Nisch W. Variation in contact guidance by human-cells on a microstructured surface. Journal of Biomedical Materials Research 1995; 29(1):81-8.

[147] Oakley C, Brunette DM. Response of single, pairs, and clusters of epithelial cells to substratum topography. Biochemistry and Cell Biology-Biochimie Et Biologie Cellulaire 1995; 73(7-8):473-89.

[148] Wojciak-Stothard B, Madeja Z, Korohoda W, Curtis A, Wilkinson C. Activation of macrophage-like cells by multiple grooved substrata - topographical control of cell behavior. Cell Biology International 1995; 19(6):485-90.

[149] Wojciak-Stothard B, Curtis ASG, Monaghan W, McGrath M, Sommer I, Wilkinson CDW. Role of the cytoskeleton in the reaction of fibroblasts to multiple grooved substrata. Cell Motility and the Cytoskeleton 1995; 31(2):147-58.

[150] den Braber ET, de Ruijter JE, Ginsel LA, von Recum AF, Jansen JA. Quantitative analysis of fibroblast morphology on microgrooved surfaces with various groove and ridge dimensions. Biomaterials 1996; 17(21):2037-44.

[151] Britland S, Morgan H, Wojiak-Stodart B, Riehle M, Curtis A, Wilkinson C. Synergistic and hierarchical adhesive and topographic guidance of BHK cells. Experimental Cell Research 1996; 228:313-25.

[152] WojciakStothard B, Curtis A, Monaghan W, Macdonald K, Wilkinson C. Guidance and activation of murine macrophages by nanometric scale topography. Experimental Cell Research 1996; 223(2):426-35.

[153] Rajnicek AM, Britland S, McCaig CD. Contact guidance of CNS neurites on grooved quartz: influence of groove dimensions, neuronal age and cell type. Journal of Cell Science 1997; 110:2905-13.

[154] Chehroudi B, McDonnell D, Brunette DM. The effects of micromachined surfaces on formation of bonelike tissue on subcutaneous implants as assessed by radiography and computer image processing. Journal of Biomedical Materials Research 1997; 34(3):279-90.

[155] Rajnicek AM, McCaig CD. Guidance of CNS growth cones by substratum grooves and ridges: effects of inhibitors of the cytoskeleton, calcium channels and signal transduction pathways. Journal of Cell Science 1997; 110:2915-24.

[156] Chou L, Firth JD, Uitto V-J, Brunette DM. Effects of titanium substratum and grooved surface topography on metalloproteinase-2 expression in human fibroblasts. Journal of Biomedical Materials Research 1998; 39(3):437-45.

[157] van Kooten TG, Whitesides JF, von Recum AF. Influence of silicone (PDMS) surface texture on human skin fibroblast proliferation as determined by cell cycle analysis. Journal of Biomedical Materials Research 1998; 43(1):1-14.

[158] Walboomers XF, Croes HJE, Ginsel LA, Jansen JA. Contact guidance of rat fibroblasts on various implant materials. Journal of Biomedical Materials Research 1999; 47(2):204-12.

[159] Deutsch J, Motiagh D, Russell B, Desai TA. Fabrication of microtextured membranes for cardiac myocyte attachment and orientation. Journal of Biomedical Materials Research 2000; 53(3):267-75.

[160] Pins GD, Toner M, Morgan JR. Microfabrication of an analog of the basal lamina: biocompatible membranes with complex topographies. FASEB Journal 2000; 14(3):593-602.

[161] Petersen EF, Spencer RGS, McFarland EW. Microengineering neocartilage scaffolds. Biotechnology and Bioengineering 2002; 78(7):801-4.

[162] Dalby MJ, Riehle MO, Yarwood SJ, Wilkinson CDW, Curtis ASG. Nucleus alignment and cell signaling in fibroblasts: response to a micro-grooved topography. Experimental Cell Research 2003; 284(2):272-80.

[163] Scheideler L, Geis-Gerstorfer J, Kern D, Pfeiffer F, Rupp F, Weber H, Wolburg H. Investigation of cell reactions to microstructured implant surfaces. Materials Science and Engineering: C 2003; 23(3):455-9.

[164] Teixeira AI, Abrams GA, Bertics PJ, Murphy CJ, Nealey PF. Epithelial contact guidance on well-defined micro- and nanostructured substrates. Journal of Cell Science 2003; 116(10):1881-92.

[165] Tan J, Saltzman WM. Biomaterials with hierarchically defined micro- and nanoscale structure. Biomaterials 2004; 25(17):3593-601.

[166] Wang YC, Ho CC. Micropatterning of proteins and mammalian cells on biomaterials. FASEB Journal 2004; 18(1):525-7.

[167] Recknor JB, Sakaguchi DS, Mallapragada SK. Growth and differentiation of astrocytes and neural progenitor cells on micropatterned polymer films. Annals of the New York Academy of Science 2005; 1049(1):24-7.

[168] Charest JL, Eliason MT, Garcia AJ, King WP. Combined microscale mechanical topography and chemical patterns on polymer cell culture substrates. Biomaterials 2006; 27(11):2487-94.

[169] Pins GD, Bush KA, Cunningham LP, Carnpagnola PJ. Multiphoton excited fabricated nano and micro patterned extracellular matrix proteins direct cellular morphology. Journal of Biomedical Materials Research Part A 2006; 78A(1):194-204.

[170] Yu B-Y, Chou P-H, Sun Y-M, Lee Y-T, Young T-H. Topological micropatterned membranes and its effect on the morphology and growth of human mesenchymal stem cells (hMSCs). Journal of Membrane Science 2006; 273(1-2):31-7.

[171] Teixeira AI, McKie GA, Foley JD, Bertics PJ, Nealey PF, Murphy CJ. The effect of environmental factors on the response of human corneal epithelial cells to nanoscale substrate topography. Biomaterials 2006; 27(21):3945-54.

BIOGRAPHICAL SKETCH

Michelle Carman, the daughter of Donna Fulford and Robert Carman, was born December 8, 1977 at Shands Hospital at the University of Florida where her father was attending dental school. Michelle was born 10 weeks premature and spent the first month of her life under the skillful watch of the NICU. She spent most of her childhood in Ocala, Florida where she graduated salutatorian of Forest High School in 1996. From there, she returned to the University of Florida and received her Bachelor of Science degree in chemical engineering in 2000 before choosing to remain at UF to study biomedical engineering in graduate school.